Theses and Dissertations   Theses, Dissertations, and Senior Projects

January 2019

Enhancing Liquid And Gas Separation With Activated Carbon Mixed-Matrix Membranes

Jeremy Lewis

Follow this and additional works at: https://commons.und.edu/theses

ENHANCING LIQUID AND GAS SEPARATION WITH ACTIVATED CARBON
MIXED-MATRIX MEMBRANES

by

Jeremy Charles Lewis
Bachelor of Science, California State Polytechnic University Pomona, 2017

A Thesis

Submitted to the Graduate Faculty

of the

University of North Dakota

in partial fulfillment of the requirements

for the degree of

Master of Science

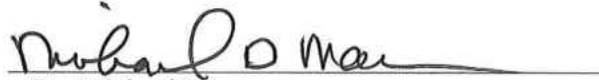
Grand Forks, North Dakota

May

2019

This thesis, submitted by Jeremy Lewis in partial fulfillment of the requirements for the Degree of Master of Science from the University of North Dakota, has been read by the Faculty Advisory Committee under whom the work has been done and is hereby approved.

_____

Dr. Ali Alshami

_____

Dr. Michael Mann

_____

Dr. Edward Kolodka

This thesis is being submitted by the appointed advisory committee as having met all of the requirements of the School of Graduate Studies at the University of North Dakota and is hereby approved.

_____

Dr. Chris Nelson, Associate Dean
School of Graduate Studies

4/26/19
_____
Date

iii

<div align="center">PERMISSION</div>

Title	Enhancing Liquid and Gas Separation with Activated Carbon Mixed-Matrix Membranes
Department	Chemical Engineering
Degree	Master of Science

      In presenting this thesis in partial fulfillment of the requirements for a graduate degree from the University of North Dakota, I agree that the library of this University shall make it freely available for inspection. I further agree that permission for extensive copying for scholarly purposes may be granted by the professor who supervised my thesis work or, in his absence, by the Chairperson of the department or the dean of the School of Graduate Studies. It is understood that any copying or publication or other use of this thesis or part thereof for financial gain shall not be allowed without my written permission. It is also understood that due recognition shall be given to me and to the University of North Dakota in any scholarly use which may be made of any material in my thesis.

<div align="right">Jeremy Lewis
4-11-19</div>

Contents

LIST OF FIGURES

LIST OF TABLES

ACKNOWLEDGMENTS

ABSTRACT

Mixed matrix membranes are one class of membrane material that are an especially promising separation media. By adding a particle phase to a matrix phase, multiple mechanistic pathways become available that are not present in pristine organic or inorganic membranes. These pathways can be exploited to better enhance separation performance for a variety of applications.

This research has focused on a specific mixed matrix membrane, which contains bio-derived activated carbon particles in a polysulfone matrix. In proper selection of activating agent, this research has shown that the surface functional groups of the activated carbon are highly influenced. This can lead to better polymer filler interaction and fewer defects. This research has also provided evidence to support the idea that by changing various membrane formation parameters such as choice of solvent, nonsolvent, and additives, can influence many of the membrane's thermal, physical, and separation properties.

This work has shown the viability of biochar and activated carbon derived from biochar are fillers that are worth investigating in mixed matrix membranes. The membranes produced were shown to have versatile applications with modifications to formation process. The applications studied include liquid phase: acid blue filtration and gas phase: CO_2/N_2, CO_2/CH_4, and N_2/CH_4.

CHAPTER I: INTRODUCTION

In the past several decades, many research efforts have been made within the area of mixed matrix membranes. Because there are so many filler and matrix materials these membranes can be made from, and the number of methods available to fabricate them, there are many properties that can be tailored to specific separation application. While this versatility has opened avenues for research and development that have previously been unexploited, it has also aroused many unanswered questions. Many of those questions involve how filler/matrix interaction can be improved to produce membranes with negligible interfacial defects. As a result, the scope of applications for new filler/matrix combinations has not yet been realized.

This research is aimed at better understanding this filler/matrix interaction and potential applications for activated carbon/polysulfone mixed matrix membrane. Activated carbon as a filler has been largely neglected. However, it has great potential due to its high porosity, specific surface area, and surface functionality. It is hypothesized that the functional groups on the activated carbon can be influenced by chemical activation of biochar. By introducing the correct functional groups on the activated carbon, dipole intermolecular forces, and pi stacking can strongly interact with the polar and aromatic groups of polysulfone. To gain insight into this hypothesis, biochar and activated carbons derived from biochar were produced from sunflower hulls, and thoroughly investigated in mixed matrix membranes.

Motivation

It is accepted that the power requirement for separation processes puts a heavy financial burden on the chemical process industry. This is mainly due to most separation processes are equilibrium driven or require a phase change. In equilibrium based separations, achieving high degrees of separation become extremely difficult, or simply unrealistic in some cases. The phase change requires large heating supply, and thus great power consumption. Additionally, the high power consumption contributes to the carbon footprint of a facility.

Membranes, on the other hand, are a rate driven separation process. This eliminated the thermodynamic limits and phase change requirements. As a result, it is anticipated that membrane based separations can help alleviate the cost and carbon footprint of traditional separation processes. Unfortunately, most membranes are simply not good enough to meet the demands of most processes. This is in part due to poor module design and lack of knowledge on membrane integration into existing processes. More importantly, this is a limitation caused by membrane material. Thus, many efforts have been made to produce membrane materials that provide better separation with higher throughput. Mixed matrix membranes are one of these efforts that are especially promising.

Published literature has shown that mixed matrix membranes containing various polymer/filler combinations perform better than their constituent materials on their own. For instance, many of these types of membranes exceed the upperbounds of gas separation. That is, the permeability/selectivity tradeoff that is traditionally seen in polymers is overcome by mixed matrix membranes. Many reports have shown that liquid separation is also enhanced in terms of higher rejection of adsorbable solutes, with improved flux.

One area which has not been extensively researched is activated carbon in mixed matrix membranes. Activated carbon is a highly porous material that can easily be processed into the desired size and with the desired functionality. This, along with its supposed low cost and abundance, makes it a promising candidate as a filler in mixed matrix membranes. Thus, the aim of this work is on better understanding how activated carbon behaves as a constituent in mixed matrix membranes.

Thesis Outline

In this thesis, one review paper (Chapter II) [1] and three research papers (Chapter III, IV, and V) are included. Each of these papers was, or will be submitted for peer review according to the citations:

(1) J. Lewis, M. Al-sayaghi, C. Buelke, A. Alshami. (2019) Activated carbon in mixed matrix membranes. *Separation and Purification Reviews*. in press.

(2) J. Lewis, M. Miller, J. Crumb, M. Al-sayaghi, C. Buelke, A. Tesser, A. Alshami. (2019) Biochar as a filler in mixed matrix materials: synthesis, characterization, and applications. *Journal of Applied Polymer Science*. in press.

(3) J. Lewis, A. Alshami. (2019) Factorial study on activated carbon mixed matrix membrane formation for aniline blue filtration. Manuscript in preparation.

(4) J. Lewis, A. Alshami. (2019) Bio-derived activated carbon-polysulfone mixed matrix membrane for gas separation. Manuscript in preparation.

Chapter II introduces the subject of mixed matrix membranes and some general aspects of membranes. It also goes into detail on how activated carbon is prepared from biomass. A comprehensive literature review is presented which focuses specifically on activated carbon in

mixed matrix membranes and discusses their formation, properties, and wide array of applications.

Chapter III focuses on utilizing biochar derived from sunflower hulls in a polysulfone matrix. The emphasis was on characterizing the material in terms of glass transition temperature, morphology, and surface tension. The use of dilute ethanol solutions as the nonsolvent was conducted and the thermodynamic considerations contributing to biochar/polysulfone interactions were discussed.

Chapter IV presents a factorial design on the fabrication of activated carbon mixed matrix membranes. Three factors considered were amount of activated carbon (powered 18 µm), concentration of polyethylene glycol additive, and solvent type. The response variables were water contact angle, agglomeration frequency, flux and aniline blue rejection. A novel method was proposed to study agglomeration frequency.

Chapter V shows the influence of activating agent on activated carbon functionality. Gas separation performance are shown with different activated carbons (micronized ~1µm) in a polysulfone matrix. The permselectivity of CO_2/N_2, CO_2/CH_4, and N_2/CH_4 are presented.

Chapter VI highlights the key findings and implications from this thesis. Suggestions for future research as also presented and outlined.

CHAPTER II: LITERATURE REVIEW

Abbreviations

ABS	acetonitrile butadiene styrene	PBT	protein bound toxins	
AC	activated carbon	PCS	p-cresylsulfate	
CAP	cellulose acetate phthalate	PDMS	polydimethylsiloxane	
CMS	carbon molecular sieves	PEBAX 2533	polyether block amide	
CNF	cellulose nanofiber	PEG	polyethylene glycol	
COD	chemical oxygen demand	PEI	polyethylenimine	
CTA	cellulose triacetate	PES	polyethersulfone	
E. coli	Escherichia coli	POMS	poly(octylmethylsiloxane)	
FFV	fractional free volume	PPSU	polyphenylsulfone	
GPG	Gonzo-Parentis-Gottifred	PSF	polysulfone	
HA	hippuric acid	PVC	polyvinyl chloride	
IS	indoxyl sulfate	PVP	polyvinylpyrrolidone	
KH550	$NH_2(CH_2)_3Si(OC_2H_5)_3$	PWF	pure water flux	
LMH	$Lm^{-2}h^{-1}$	SEM	scanning electron microscopy	
MMM	mixed matrix membrane	U	uranium	
PAC	powdered activated carbon	UV_{254}	measured by UV-Vis at 254 nm	
PAE	polyamide-amine-epichlorohydrin	YDH-171	$CH_2CH- Si(OCH_3)_3$	

Abstract

Mixed matrix membranes (MMMs) have emerged as strong contenders to conventional membranes for gas and liquid separations. Although numerous studies on filler/matrix combinations have been conducted and thoroughly reviewed, a review of activated carbon (AC) as a filler has thus far been minimal. This review intends to fill this gap via critically analyzing the state-of-the-art on AC as a filler in MMMs. Aspects of AC-MMM research, with emphasis on AC fabrication from biomass pyrolysis, AC-MMM fabrication and resulting properties, and influence of AC on MMM performance are thoroughly elucidated. Furthermore, the various applications that have been investigated with AC-MMM membranes,

and several predictive models that have been specifically utilized for AC-MMMs are also discussed.

1. Introduction

1.1. Motivation

Membranes for liquid and gas phase separations have evolved considerably in the past few decades. One major breakthrough was the development of MMMs, which are a composite two-phase membrane consisting of a polymeric continuous phase and a dispersed organic or inorganic filler. The continuous phase is commonly referred to as the matrix. MMMs have been the subject of extensive research studies and reviews involving a variety of organic and inorganic fillers, except for AC and biochar: two significant fillers with promising separation properties coupled with an abundance of low-cost raw material and processing techniques.

In recent years, AC has been gaining traction as a filler in MMMs. In this work, we present an up-to-date review of the literature and the state-of-the-art of research involving MMMs with the primary focus on AC and biochar as principal fillers. Special emphasis will be directed towards addressing AC-MMMs in terms of its formation, properties, applications, and predictive models that can be utilized for their performance.

1.2. Background

Starting as early as 1973, MMMs were studied by Paul and Kemp (1) and have grown into a field of their own. In some sense, the term "mixed matrix membrane" is a broad category of composite membranes that consist of adsorbent, nanocomposite, and hybrid membranes. During the late 1970s, MMMs were referred to as sorbent membranes, because adsorbent fillers were originally used and their adsorbent properties exploited (1). Recently, MMMs have

been cited as both nanocomposite membranes (2,3), especially when the filler is nanometers in diameter, and as hybrid membranes (4) which highlight the two species independently responsible for selectivity.

Nonetheless, MMMs remain attractive because by combining the properties of the matrix and filler, enhanced properties are achieved including improved separation performance in terms of selectivity and flux, as well as physiochemical properties such as hydrophilicity, porosity, surface charge, and mechanical strength.

Several different combinations of filler/matrix materials have been investigated. Commonly reported fillers include carbon nanotubes (5), metal organic frameworks (6), molecular sieve particles (7,8), and zeolites (9). A breadth of polymers have been studied in MMMs including polyimides (10,11), polysulfones (12,13,14), copolymers (15), and cellulose acetate (16) to name a few. Altogether, these combinations have been investigated for applications including water purification, pervaporation, gas separation, and proton exchange.

Many articles have been written reviewing the topic of MMMs in the last decade. Aroon et al. (17), Goh at al. (18), and Chung et al. (19) authored reviews focusing on gas phase separations. Rezakazemi and Vinoba et al. focused specifically on carbon dioxide separation (20,21). Goh et al. (22) and Qadir et al. (23) published reviews focusing on water purification. Other reviews focused specifically on filler materials including zeolites (9,24), metal organic frameworks (6), nanoparticles (25), and 2D materials (26,27).

Considering the breadth of matrix and filler materials as well as applications that have been investigated, one point of confusion in the definition of MMMs is the classification of the filler. Most reports in the literature define the filler as inorganic, while still recognizing organic

type fillers as possibilities. For example, carbon nanotubes and graphene are two organic compounds (i.e. made of only C, H, N, O) that have been categorized as organic and inorganic. Thus, the confusion has arisen because of the somewhat arbitrary categorization of organic and inorganic materials, because polymers are typically referred to as organics, and due to filler materials behaving very differently than polymers.

A comparison of MMMs to different membranes is presented in Table 1. Note the different categories for polymeric and organic membranes. Categorizing membranes into these four classes helps alleviate some confusion, especially between organic, inorganic, and polymeric materials. Although it is not common practice to present the class of "organic membranes" to mean those such as graphene, it is the authors' opinion this categorization is useful.

Table 1: General comparison of different membranes in terms of their advantages/disadvantages in relation to the emerging class of MMMs.

Membrane	Advantages	Disadvantages
Polymeric Membranes (28,29) Ex: polysulfone, polyimide, polyethersulfone	• Easy synthesis and fabrication • Low production cost • Good mechanical stability • Easy upscaling and modeule design • Separation mechanism: Solution diffusion	• Low chemical and thermal stability • Plasticization • Pore size difficult to control • Permeability/selectivity trade off
Inorganic Membranes (30) Ex: Titanium oxide, zeolite, metal organic frameworks	• Superior chemical, mechanical, and thermal stability • Tunable pore size • Moderate permeability/selectivity trade off • Stable in harsh conditions • Separation mechanism is dependent on pore size	• Brittle • Expensive • Difficult to scale up

Organic Membranes Ex: Carbon nanotubes(31), graphene (32)	• Tunable functional groups • Tunable pore size • Exceptional rejection in liquid separations • Moderate permeability/selectivity tradeoff • Separation mechanism: molecular sieving	• Difficult and expensive to make • Difficult to scale up • Can be frail
Mixed matrix membranes Ex: Matrimid-AC (10), PES-Kaolin (33), PVA-carboxyfullerene (34), PSF-MOF1 (35)	• Enhanced mechanical and thermal stability • Reduced plasticization • Low energy requirements • Surpasses permeability/selectivity trade off • Reduced fouling • Separation mechanism determined by the combined polymeric and filler properties	• Become brittle with high filler loadings • Poor interaction between matrix and filler results in unselective pores • Chemical and thermal stability depends on matrix material

2. Production of Biochar and Activated Carbon

Biochar primarily is the solid product of biomass pyrolysis and is commonly used as a precursor for AC, which is a unique material for various reasons. Variable particle sizes are achievable with simple mechanical grinding or crushing methods. AC is highly porous leading to excellent adsorptive capacity for various gaseous and aqueous species. They can also be functionalized by physical or chemical treatment, making them versatile for various applications.

2.1. Pyrolysis

AC is typically produced from carbonaceous materials such as biomass, sludge, and petroleum pitch via pyrolysis, a thermochemical decomposition of matter at a relatively moderate

temperature range of 200 to 700 °C. Currently, commercial AC is produced from coconut husks, wood saw dust, and coal (36). The first step in producing AC is the formation of char from these carbonaceous materials.

Depending on the pyrolysis conditions and end use, char takes on different names. Ahmad et al. conducted a thorough review including the definitions used for the pyrolyzed carbonaceous materials (37). In essence, char from a biomass feedstock has been labeled as biochar when it is produced in a dry environment and used as a soil amendment. Hydrochar is produced from biomass in an aqueous environment. On the other hand, charcoal is produced from coal and is meant to be used as a fuel. In recent years, the term biochar has been used to convey solid-pyrolyzed biomass, regardless of its end use. For simplicity, this paper defines biomass in its traditional sense, and AC is any biochar or other precursor that is activated as described in the following section.

Two types of pyrolysis are frequently studied: fast and slow pyrolysis, with the principle difference between them being the heating rate. In fast pyrolysis, the heating rate is on the order of hundreds of degrees centigrade per second, reaching its maximum temperature within seconds. The heating rate of slow pyrolysis, on the other hand, is on the order of tens of degrees centigrade per minute, reaching a peak temperature after several minutes, hours, or days (38).

Reactions taking place during the pyrolysis of biomass have proven to be extremely complicated. Depending on the feedstock, various products are formed based upon processing temperature and residence time (39). Regardless of the chemical species formed, it is clear that the result of pyrolysis is four unique product mixtures: 1) volatile gases, 2) bio-oils, 3) tars, and 4) solid char. Previous studies have focused on maximizing yield and characterizing bio-

oils (40). Bio-oils are potentially low grade fuel sources or fuel additives, as their heating values are typically slightly lower than conventional fuels (41). Tars are typically an undesired by-product of pyrolysis (42); however, some research has been conducted on upgrading their by-products into more desirable compounds (43). There is also some potential in using the tar as a composite additive (44). The solid that remains post pyrolysis treatment is the biochar.

2.2. Biochar

Biochar produced in the aforementioned section has several beneficial physical properties. Most notably, various sized pores are formed that create a porous substructure with a large amount of surface area (45,46,47). Depending on the biomass feedstock and pyrolysis conditions, surface functional groups tend to form, influencing its hydrophobicity and wettability (48). Table 2 lists a wide range of biochar derived from various feedstock and their relevant resulting properties. For a detailed review on biochar formation mechanisms, properties, and how biochar functionalization occurs, see Liu et al. (49).

In general, there exists a tradeoff between surface area and functional group formation as pyrolysis temperature increases. At high pyrolysis temperatures, biomasses tend to break down into bulky aromatics and lose their oxygen containing functional groups, which leads to high surface area. At relatively low temperatures, biochars tend to retain their functional groups, but have lower surface area. At extremely high temperatures, thermal cracking of the biochar occurs, causing pores to collapse and decreasing surface area. Depending on the biomass, an optimal temperature can vary between 300-800°C.

2.3. Activated Carbon

Once biochars are formed, they are subjected to activation treatments including physical, chemical, or combination activation. The term 'activated' is most often used to describe the state of enhanced physical and functional properties.

Table 2: Properties of various biochars and their corresponding pyrolysis conditions. The pyrolysis type (fast/slow) is listed in the case exact heating rate was not listed.

Biochar Feedstock	Surface Functional Groups	Surface Area (m^2/g)	Pyrolysis Temperature and Heating Rate
Guinea Fowl Manure (50)	Hydrogen bonded, aliphatic amines	60.0	250°C – 2°C/min then 500°C – 5°C/min
Sugarcane Bagasse (51)	phenolic acids, carboxylic acids, lactonic acids	92.30	500°C, slow
Orange Peels (51)	phenolic acids, carboxylic acids, lactonic acids	0.21	500°C, slow
Sunflower seed hull (52)	Alcohols, amines, aromatic	3.850	450°C, fast
Bamboo (45)	Hydroxyl, carbonyl	332.10	600°C , slow
Date Palm (53)	Carbonyl, carboxylic acids	-	300-800°C, 5°C/min
Sewage Sludge (54)	Carbonyl, protonated	54.05	700°C , 25°C/min
Rice Husk (55)	Alcohols, phenol, carbonyl	27.8	350°C, 25°C/min
Dairy manure (55)	Hydroxyl, carbonyl, phosphate, aromatics	5.61	350°C, 25°C/min
Coconut coir (56)	Carboxylic acids, phenolic acids, hydroxyl	153	500, slow
Peanut Shells (46)	Carbonyl, aromatic, aromatic amines	420	700°C, 7°C/min
Soybean Stover (46)	Carbonyl, aromatic, aromatic amines	448	700°C, 7°C/min
Maple Wood (57)	Deprotonated carboxyl and phenolic acids	225	500°C, 2.5°C/min

Eucalyptus saw dust (58)	Carboxylic, hydroxyl	1.57	120°C, slow
Swine Manure (59)	Hydroxyl, carboxylic	3.46	400°C, 25°C/min
Rice Straw (59)	Carbonyl, hydroxyl	2.01	400°C, 25°C/min
Corncob (60)	Carbonyl, nitro, hydroxyl, methoxyl	3.38	15°C/min , 550°C
Potato Peel (61)	Carbonyl, hydroxyl, aromatics	2.29	700°C, 2°C/min
Pine Needle (47)	Hydroxyl, carbonyl, aromatics	390.52	700°C, 7°C/min
Almond Shell (62)	Carbonyl, phenols, lactones	30.35	650°C, 10°C/min

Physical activation involves high-temperature treatment of biochar with oxidizing gases, such as carbon dioxide (63), steam (64), and air (65). Often physical activation leads to enhanced surface area and pore density while oxidizing surface functional groups. The formation of $C=O$ and O-H functional groups are typically apparent, whereas C-H and C-O functional groups usually disappear.

Chemical activation involves first impregnating the biochar with a chemical compound and then subjecting it to a high temperature treatment in an inert atmosphere or a vacuum. Typical activating chemicals are acids, bases, and oxidizing agents such as zinc chloride or hydrogen peroxide (66). An important parameter to consider during chemical activation is the impregnation ratio, or the ratio of the activating agent to the biochar. Upon impregnation, the biochar is subsequently treated at elevated temperatures in an inert atmosphere. This step is most often referred to as carbonization. Following carbonization, the AC is typically washed with a weak acid or base to remove the residual activating agent, and then washed with distilled or deionized water. Chemical activation can lead to an increased surface area, pore size and

volume, and tailored functional groups. Table 3 summarizes recent literature in terms of feedstock, activating methods, and resulting properties.

Chemical activation generally leads to the formation of carbonyl functional groups, such as ketones and carboxylic acids. The hydroxide functional group is also typically present, though in varying degrees depending on precursor biomass. Another noteworthy trend commonly seen is a maximum surface area achieved with respect to an optimal carbonization temperature. At relatively low temperatures, pore formation is restricted while at relatively high temperatures, functional groups tend to collapse and reduce pore size.

Table 3: Chemically activated AC produced from biochar and their processing conditions and resulting properties.

Feed Stock	Activating Agent	Impregnation Ratio (agent: biochar)	Carbonization Temperature	Surface Area (m^2/g)	Functional Groups
Spruce Whitewood (67)	KOH	3.5 : 1	475°C	643	Hydroxyl, aromatics
			675°C	1317	
			875°C	2024	
Palm Date Seed (68)	NaOH	3:1	600°C	1282.49	Carbonyl, ketones, ethers, nitro
Coconut Shell (69)	H_2SO_4	1.5 : 1	600°C	-	Hydroxyl, carbonyl, ethers, aromatics
Grape Bagasse (70)	H_3PO_4	3:1	400°C	1021	Carbonyl, esters, ketones, aliphatic acids
			500°C	909	
			600°C	629	
Grape Stalk (71)	$ZnCl_2$	0.5: 1	700°C	482.22	Hydroxyl, aromatics
		1:1		889.62	
		1.5: 1		1004.48	

Source	Chemical	Ratio	Temperature	Surface Area	Functional Groups
		2:1		1411.75	
Rice Husk (72)	KOH	5:1	750°C	2121	Hydroxyl, aromatics, ethers, esters
			850°C	2696	
			950°C	1592	
Sugar Cane Bagasse (73)	ZnCl$_2$	2:1	500°C	2200	Hydroxyl, carbonyl, aromatics
Sunflower Hulls (73)	ZnCl$_2$	2:1	600°C	1950	Hydroxyl, carbonyl, aromatics
Poplar Saw Dust (74)	KOH	1: 0.05	600°C	1506.2	Hydroxyl, carbonyl, carboxylic acids
Paulownia Wood (75)	H$_3$PO$_4$	4:1	400°C	2806	Carbonyl, aromatics, ketones, lactone, carboxyl, phosphates
Pork Bones (76)	H$_2$SO$_4$	2.8 : 1	800°C	110.7	Phosphates, carbonates

Both scenarios result in lower specific surface areas. It is also apparent that the higher the impregnating ratio, the higher the specific surface area becomes for any one activating chemical at a specified temperature. Other factors such as carbonization pretreatment and chemical washing of the AC tend to also influence the final properties.

Due to ACs having large surface areas, pore volume, and functionality, they adsorb species from both liquids and gases. Hence, regardless the type of fluid under investigation, liquid or gas, it is necessary to consider the adsorption of each species onto the AC to fully exploit and understand the separation capabilities of AC-MMMs.

2.4. Carbon Molecular Sieves

CMS are a class of AC which are derived from polymeric precursors rather than biomass. Despite the difference in precursors, CMS are fabricated and activated in a manner very similar to that of AC. This is by controlled pyrolysis and further chemical or physical activation (77). There are a couple very important differences between CMS and AC. First is the resulting pore sizes after pyrolysis. CMS typically contain pore sizes in the micropore and ultramicropore range (77), while AC typically have a broad pore size distribution in the micro, meso, and macro pore region (78,79). Secondly, CMS can be directly prepared into membranes. For instance, a cast membrane can undergo pyrolysis and retain its shape, resulting in CMS membranes, or simply, carbon membranes (80). Although an interesting class of membrane, carbon membranes are not included in this review. Rather, CMS can be made into particles, by mechanical grinding, and used as a filler in MMMs (81). These types of materials are discussed where appropriate.

3. AC Compatibility with Polymers and Solvents

The interaction of AC with both the polymer phase and solvent play an important role in AC-MMM development. One issue is sedimentation, whereby particles tend to settle in the casting solution rather than form a suspension. This is an occurrence that challenges the use of many fillers, and notably AC, in MMMs (82). Sedimentation causes undesired variability in particle loading, and skewed particle size distribution in the final membranes. To avoid separation from casting solutions, particle size should be closely controlled as small particles generally remain suspended in the solution longer (15). Another method is to ensure adequate mixing with sonication, albeit partial sedimentation may occur in some solvents (83).

A secondary issue that usually arises from improper solvent selection is particle breakage, in which some solvents possess the capability of etching formed pores in AC (84). This causes breakage as depicted in Figure 1. Although the breakage of AC in solvent is not frequently considered, the reduction in particle size and pore volume are two possible results that could cause unforeseen effects to AC-MMMs.
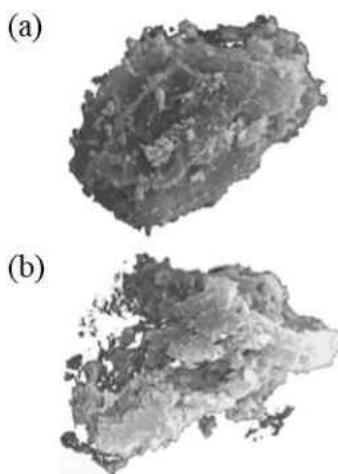
Figure 1: Particle breakage due to solvent etching of formed pores post activation of a 15 micron AC, (a) before, and (b) after contact with dimethylformamide (84). Reprinted with permission from Elsevier.

The most prominent issue with MMMs, however, remains to be the poor polymer-filler interaction causing unselective void space and consequently unselective membranes (6,24,85,86). While there is generally a good understanding of how some particles, such as colloids (87), interact in various solutions, very little is thus far known about the exact AC-polymer interaction. It has been suggested that the adsorption capacity of polymers by AC can be a good metric for compatibility (88); nevertheless, this has only been investigated for water soluble polymers in the liquid phase and not with interactions between two solid phases (88). Currently, photographic and thermomechanical observations serve as the best metric for AC/polymer compatibility.

Imaging is sometimes used to observe adhesion between AC particles and the polymer within the cross section of MMMs (89). Although not accurate, thin polymeric coatings surrounding AC particles can indicate good compatibility. In terms of mechanical properties, when a specific AC is compatible with the polymer matrix, mechanical properties tend to improve as measured by increases in tensile strength (90), fracture stress (91), or Young's modulus (90). Thermal properties also tend to become enhanced, as measured by an increase in glass transition temperature (92,93).

Loading MMMs with AC of small particle size is one method to increase interaction (94). For example, AC with a particle size of 750 nm demonstrated good interaction in a CAP matrix as measured by an increase in fracture stress (91). Particles with sizes between 1.5 and 3.5 micron showed good compatibility with a POMS matrix (89). However, it has been shown that, not only does the average size influence AC/polymer interaction, but the size distribution does as well. AC with a larger particle size distribution tend to disperse in a more inhomogeneous fashion and agglomerate more frequently (89).

Other methods to improve polymer-filler interaction include utilizing AC that has similar hydrophobicity or hydrophilicity as the polymer (95), which enables the binding of the polymer to the AC particles and increases the likelihood of strong interfacial compatibility (85).

The incorporation of ionic liquid additives into the MMM has also shown to improve the compatibility of filler/matrix (96). Ionic liquids act as a wetting agent between the particle and matrix, preventing the formation of interfacial defects. Moreover, the use of ionic liquid additives can prove versatile, as various anion/cation combinations are possible and can be tailored to specific membranes or applications (97). Surfactant and other salt additives also

serve to improve the filler/matrix interaction by maintaining a particle suspension, preventing particle agglomeration and subsequent sedimentation. Other low molecular weight additives can serve to physically fill the void space between filler and matrix, improving the MMM performance (98).

The influence of functional groups is one of the most important factors to consider. Poor intermolecular interactions between filler and matrix is the ultimate cause of interfacial defects. Thus, much worked has been performed in fabricating and modifying fillers to improve this interaction (98). Strong intermolecular forces like hydrogen bonding and dipole interactions are prime targets. However, pi-pi stacking of highly aromatic fillers or matrixes can also contribute to strong interaction (11). Various methods have been performed to achieve the desired functional groups on fillers in MMMs. Grafting of various molecules such as silane coupling agents is a well-accepted method, specifically for zeolites, silica, and carbonaceous fillers. Functional groups can also be directly incorporated onto fillers by surface modifications. Variations in synthesis conditions with additives is especially effective at creating multifunctional sites on metal organic frameworks. Ion exchange treatment can also be performed to alter ionic sites to the filler (98).

AC presents an interesting case for functional group led design of MMMs. As discussed earlier and shown in table 2 and 3, the functional groups present in AC is dependent on precursor and activating method. Thus it is important to carefully consider the AC precursor and the parameters that are chosen to create the AC, due to their influence on functional groups. Other, yet more involved, methods for adding functionality and improving interfacial compatibility of AC have been investigated. For example, Saranya et al. functionalized AC with alginate to form AC-alginate aggregates, and then further cross-linked the aggregates with

calcium as shown in Figure 2 (99). The alginate functionalized AC ensured active adsorption sites were available and prevented AC agglomeration.

Another method of modifying AC to enhance its interaction with polymers is by grafting silane coupling agents. Lan et al. grafted two different compounds, YDH-171 and KH550, to biochar (Fig. 3) (95). By grafting with hydrophobic or hydrophilic compounds, the overall hydrophobicity of the MMMs could be altered or enhanced. In this case, YDH-171 in a PDMS matrix resulted in MMMs with higher hydrophobicity than pristine PDMS (95).
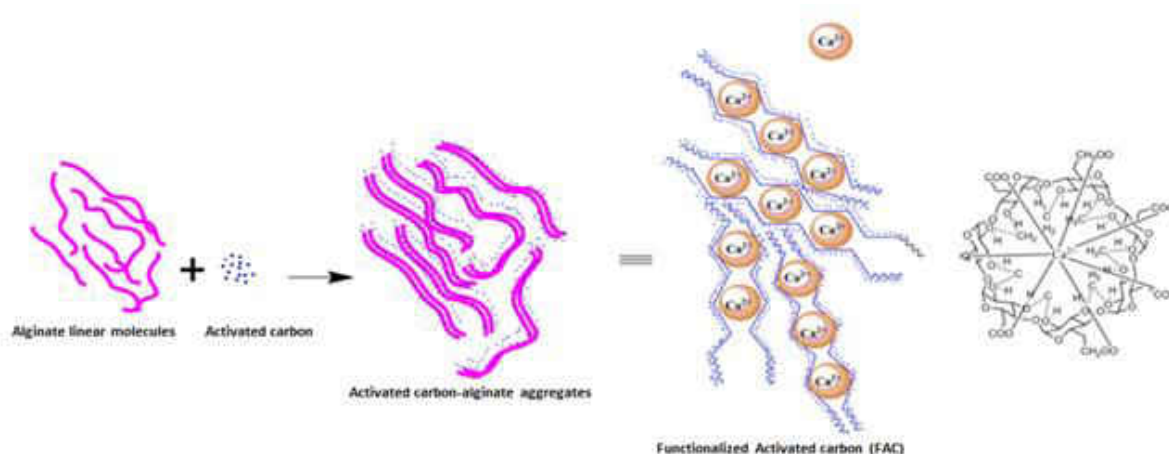
Figure 2: Schematic representation of AC functionalized with alginate by an ionic polymerization method and cross linked with calcium by the dissolution of calcium chloride in water (99). Reprinted with permission from Wiley.
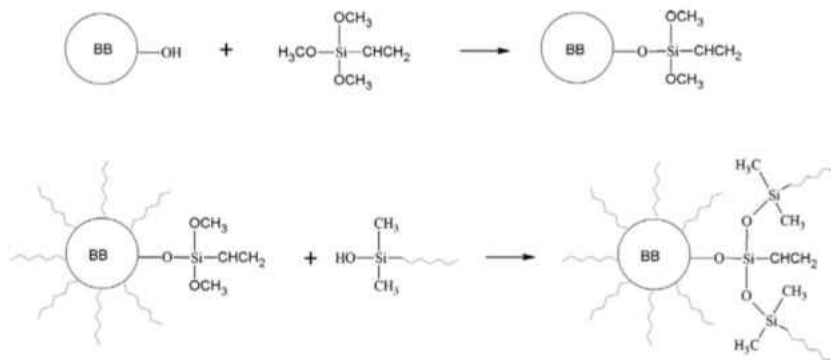
Figure 3: Proposed reaction between grafted biochar with PDMS resulting in highly hydrophobic membranes. Biochars (BB) were grafted with either YDH-171 (hydrophobic) or KH550 (slightly hydrophilic) (95). Reprinted with permission from Wiley.

4. Fabrication of MMMs

MMMs are fabricated into two primary configurations: flat sheets and hollow fibers. Depending upon the desired end application, membrane thicknesses can range between 10 – 200 microns, and can have active layers less than 10 microns. Both flat sheets and hollow fiber membranes can be formed in a similar fashion: casting solution formation, casting, and then precipitation. Each step is detailed in the following sections.

4.1. Formation of Casting Solution

Several methods exist to formulate the casting solution (94). The simplest one is by simultaneously dissolving the polymer and the AC in the appropriate solvent. Although quick and simple, this method runs the risk of disrupting the polymeric chains and forming agglomerations. A slightly different, but more common method, involves first dissolving the polymer in the solvent, then adding the AC once the polymer is completely dissolved (15,90). While this reduces the risk of disrupting the polymer chains, AC agglomerations may still form. In order to further reduce the risk of possible agglomeration, some researchers have dissolved the polymer and AC in a solvent separately, then combined the two solutions (89,100,101). Another method to reduce the presence of agglomerations in the casting solution is to simply filter it using a fine mesh before casting (15,102). In doing so, the casting solution is separated from agglomerates with a larger size than the mesh utilized. For all methods, dispersion of the filler in the solvent and the polymer is facilitated by mechanical stirring. Although polymer solutions are viscous, sonication can further disperse the filler and eliminate trapped gases without degrading the polymer (103,104).

The concentration of the polymer in the casting solution, as well as the choice of solvent, are critical parameters influencing pore size, thickness, free volume, d-spacing, and ultimately the separation properties of the formed membrane (105,106,107). One of the most crucial parameters for MMMs is the amount of filler added. That is, dilute amounts of filler can have negligible influences on membrane properties, and high concentrations of filler tend to cause void formation, agglomeration and surface ruptures.

4.2. Membrane Casting

Once the casting solution is made, it can then be formed into the desired shape. Most commonly, flat sheet membranes are cast using a casting knife or doctor blade on a proper supporting material made of glass or other rigid and inert materials (108). A moderate casting speed is usually utilized ranging from 2 cm/s to 5 cm/s. Although, this can be difficult to control unless automated techniques are utilized. In this way, the thickness of the membrane is controlled. With low viscosity solutions, it is sometimes necessary to fill a mold with casting solution rather than cast it (109).

The process used to create hollow fiber membranes is commonly referred to as spinning. The spinning process involves extruding a casting solution through an annular spinneret while a bore fluid flows through the annular center of the apparatus. The flow rate of casting solution and bore fluid are important parameters to consider and are typically set between 0.1 and 0.6 ml/min. Several additional factors influence membrane morphology including the viscosity of the casting solution, the bore fluid properties, as well as spinning parameters (110).

Using either casting or spinning, most single layer membranes can be fabricated. Similar techniques are used to create two layer membranes, but with special instrumentation. For example, a co-casting knife can be used to create two-layer flat sheet membranes with a combination of MMMs and pristine polymer layers (111). Likewise, hollow fiber spinnerets can be equipped with multiple nozzles to create a two-layer hollow fiber membrane (112,113). Both apparatuses are depicted in Figure 4.
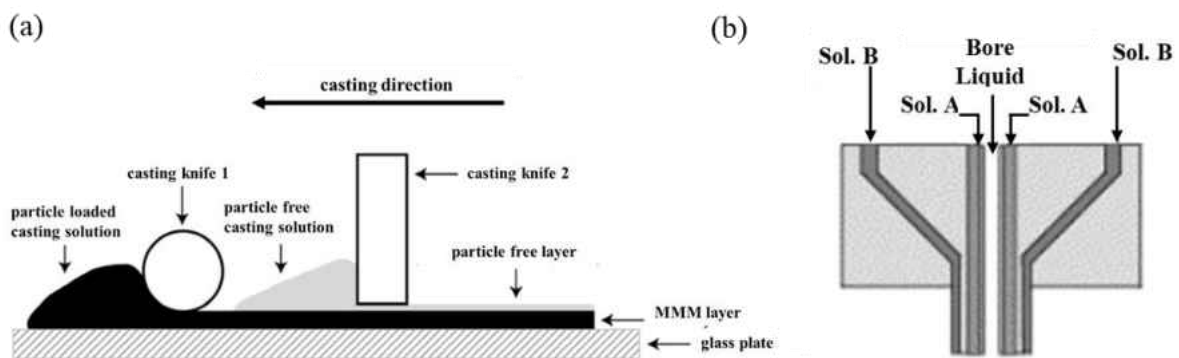
Figure 4: Schematic diagrams of multilayer casting apparatuses. Co-casting blade for (a) flat sheets (111) and multi-nozzle spinneret for (b) hollow fibers (113). Reprinted with permission from Elsevier.

4.3. Phase Inversion

Once the casting solution is cast, it is necessary to precipitate the membrane. This can be done using one of three methods: wet, dry, or combination wet/dry phase inversion.

4.3.1. Wet Phase Inversion

Wet phase inversion, sometimes called non-solvent induced phase inversion, can be used for polymer matrices that are insoluble in water or another non-solvent. Once cast, the solution is submerged into an appropriate non-solvent. Demixing of the solvent into the non-solvent occurs rapidly, and the polymer membrane precipitates, typically leaving behind a dense top layer with a porous supporting layer. It is understood that the kinetics of the demixing process

influence the type of porous supporting layer. The demixing process can be explained using a tertiary phase diagram shown in Figure 5 (108).
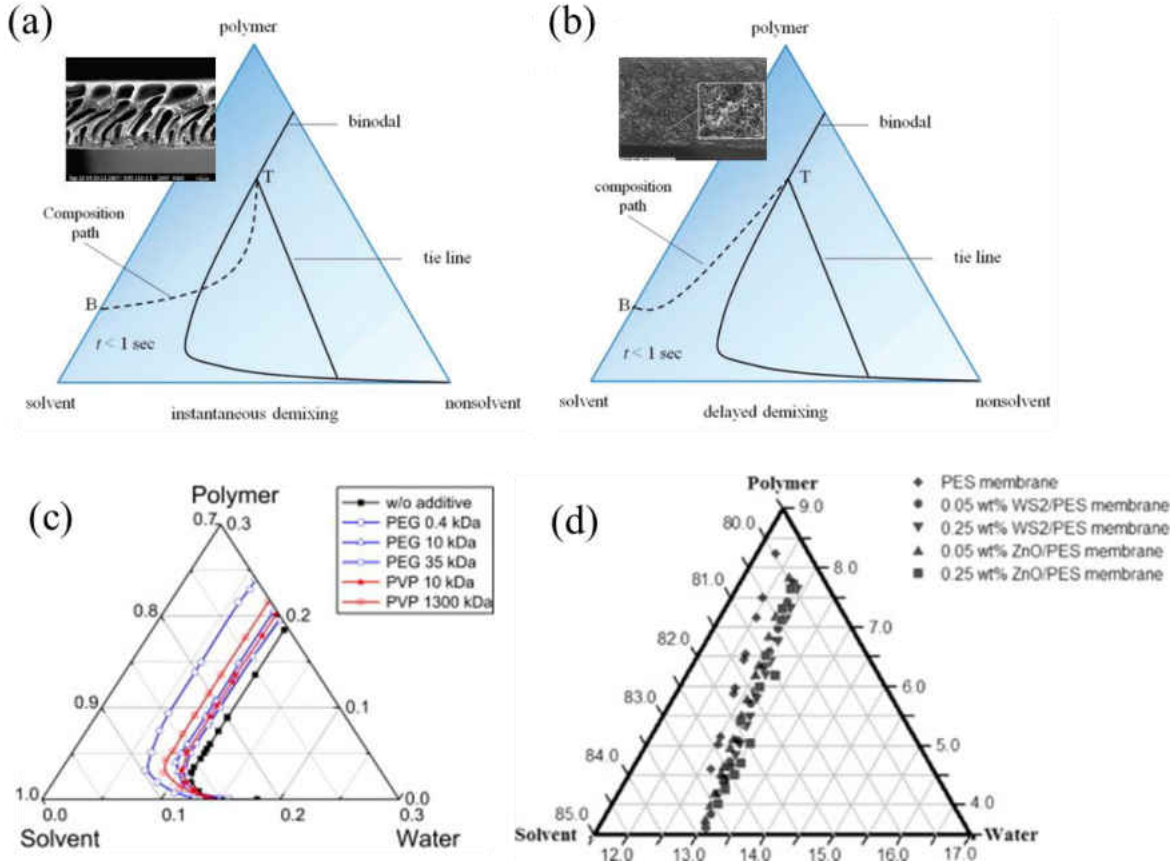
Figure 5: Ternary phase diagram showing (a) instantaneous demixing and the resulting finger-like morphology (108,114) (b) delayed demixing and the resulting spongy morphology (108,115) (c) the influence of PEG additives on binodal position (116) (d) the influence of metal particle additives on binodal position (117). Reprinted with permission from (a,b) ACS and (c,d) Elsevier.

The binodal line represents the cloud point of the ternary system and is physically the point where demixing begins to occur and the polymer begins to precipitate. The position of the binodal as well as the composition path show interesting trends in terms of membrane morphology. That is, when the so called "instantaneous demixing" occurs, the composition path crosses the binodal line and a finger like structure dominates. When "delayed demixing" occurs, the composition path does not cross the binodal line, resulting in a spongy structure.

The ternary system is strongly influenced by the solvent and non-solvent as the location of the binodal line changes for different components. A typical non-solvent is water since it is inexpensive and environmentally benign, however, other non-solvents such as methanol, hexane, acetone, and xylene have been reported (118,119). The binodal is also strongly influenced by the presence of additives in the casting solution. Water soluble polymers like PEG and PVP, as well as surfactants such as Triton-X, shift the binodal and influence membrane morphology (120,121,122). Interestingly, the presence of fillers also causes a shift in the binodal line. While this phenomenon has not been studied with AC, likely due to the difficulty in visualizing the cloud point in black casting solutions, it was seen with metal particles (117), and likely exhibits similar trends with AC. The shifts in the binodal line are the result of the strong affinity of the non-solvent toward the additives or fillers, preventing the exchange between solvent and non-solvent.

Wet phase inversion usually results in asymmetric membranes with a dense top layer, which is useful in gas phase separation applications. However, by adding pore forming agents or fillers to the casting solution, pores begin to form, creating a membrane suitable for liquid phase separations (99,120).

Adding filler particles to the casting solution tends to reduce the appearance of fingerlike structures and results in spongy cross sections with an ultrathin selective layer as a result of delayed demixing. However, combinations of pore forming agents, surfactants, and fillers can cause interesting morphologies. One example worth noting used a PSF matrix, PEG pore former, and Triton-X-100 non-ionic surfactant. AC was loaded into the MMM with 0.1, 0.5, and 1 wt.% concentrations. The influence of AC loading on MMM morphology was investigated. The use of Triton-X created a fingerlike morphology which broke down with the

addition of 1 wt.% AC. The surface pore size also increased with AC loading as shown in Figure 6 (121).
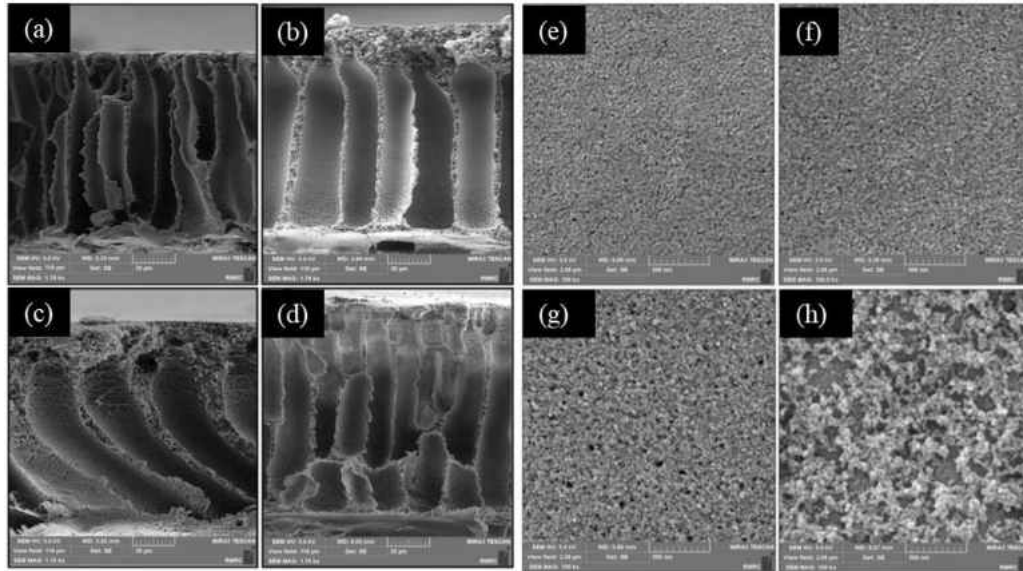
Figure 6: Triton-X results in finger like structure however, this finger like structure breaks down and surface becomes more porous with increasing amounts of AC from (a,e) 0 wt.%, (b,f) 0.1 wt.%, (c,g) 0.5 wt.%, and (d,h) 1 wt.%. (121). Reprinted with permission from Elsevier.

One interesting phenomena that has been documented during wet phase inversion with hydrophobic AC is the tendency of AC to settle near the top surface of the membrane depicted in Figure 7 (91,123). In this case, hydrophobic particles accumulate near the top of the membrane due to the instantaneous exchange of solvent with water at the top of the membrane, resulting in repulsion between AC and non-solvent near the bottom of the membrane causing migration of the AC to the top surface (13,91,123). Thus, increasing the exchange rate between solvent and non-solvent prevents this migration and particles remain randomly embedded.
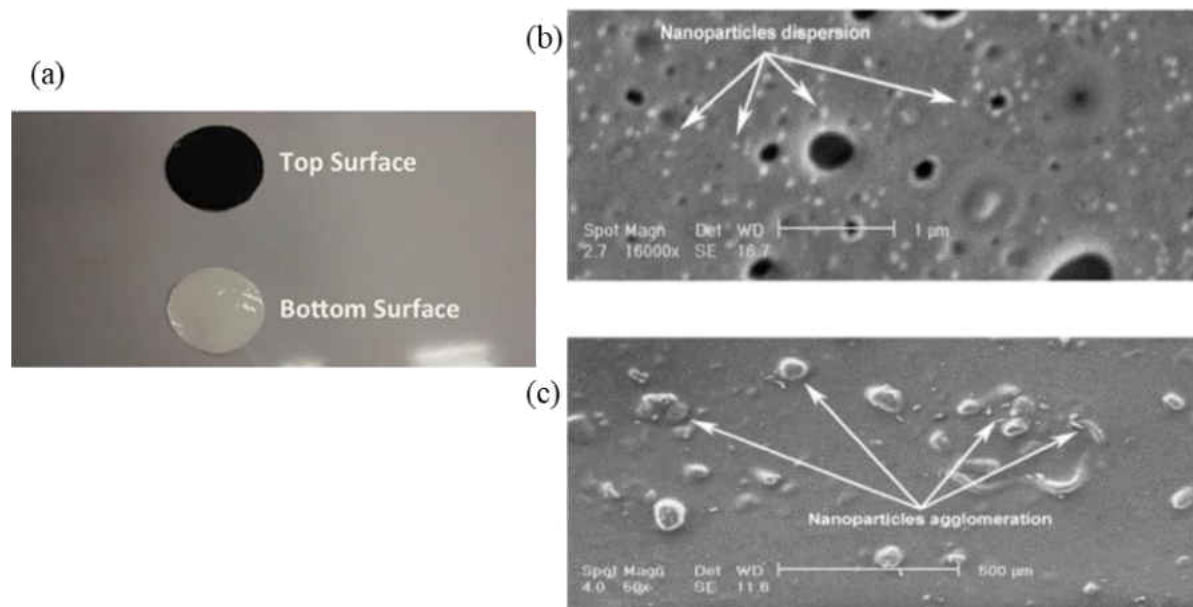
Figure 7: Migration of hydrophobic AC to the top surface occurs during wet phase inversion. (a) Macroscopic view showing black AC more apparent on the top view. (b) SEM image showing AC dispersion and pores on the bottom side with (c) High concentrations of agglomerations on the top side (123). Reprinted with permission from Elsevier.

4.3.2. Dry Phase Inversion

Another method of precipitating the membrane out of solution is by dry phase inversion, often called precipitation by solvent evaporation. In this method, the solvent is removed from the casting solution by evaporation rather than liquid-liquid demixing. The rate of evaporation, and thus the environment, temperature, and pressure, are key variables that influence the membrane properties. Dry phase inversion is typically performed in a vacuum or inert environment at elevated temperatures (15,124). Although, some research has been performed in humid environments where the relative humidity greater than 90% (125). Ambient environments are also utilized where the presence of oxygen and normal humidity levels of less than 60% are considered (90,92). High humidity levels tend to create areas of nonsolvent induced inversion, creating a slightly more porous surface which greatly influences performance (125). Otherwise, this method tends to produce dense membranes with a

nanoporous surface and a dense cross section (126). Increasing amounts of AC produce cross sections with less homogeneity as shown in Figure 8 (89).

Figure 8: POMS membranes formed with AC loaded with (a) 10 wt.% (b) 20 wt.% (c) 40 wt.% showing the increase in inhomogeneity with increasing amounts of AC (89). Reprinted with permission from Wiley.

One major advantage to the dry phase inversion technique is the thermal treatment of the membrane to influence free volume and chain rigidity (127). Moreover, the addition of AC tends also to influence free volume and chain rigidity mainly due to the AC porosity and crosslinking ability (95). When precipitated under appropriate conditions, this method works complimentary with AC addition.

4.3.3. Dry/Wet Phase Inversion

The final method is a combination of the previous two methods. Typically, solvent in the casting solution is allowed some time to evaporate before being submerged in a non-solvent (10,128,129). The dry phase step is allowed to occur for seconds to minutes, then wet phase inversion completes the precipitation. It is important to note, if complete precipitation occurs during the dry phase step, the effects of the wet phase step are not evident. Hence, the dry phase step should be carefully controlled as to not allow complete solvent evaporation.

In this case, a variety of membrane structures can form. Frequently, the benefits of both methods are evident, creating asymmetric membranes with few surface defects (130). The dry/wet phase inversion method is typically followed for fabricating hollow fiber membranes.

Table 4: Comparative properties of membranes produced by different phase inversion methods.

Inversion Method	Surface Morphology	Cross Sectional Morphology
Wet	Dense surface unless high filler content or pore forming agents are used.	Asymmetric with dense top skin and porous supporting layer. Porous layer can appear spongy, finger-like, or a combination of the two depending on inversion conditions.
Dry	Dense unless the evaporation rate is rapid, then surface pores can form. Filler materials can also cause ruptures leading to porous surfaces.	Dense and either homogeneous or asymmetric.
Dry/Wet	Dense or porous depending on the specific casting solution formation and conditions.	Dense or porous and asymmetric depending on the dry and wet phase steps. If the dry step dominated, the cross section will be denser than if the wet step dominates.

5. Relationship Between Surface Chemistry and Permeability

One of the main advantages of using MMMs is the fillers' influence on the surface chemistry and separation properties of the membrane materials. The use of AC in MMMs has a significant impact on the surface properties of MMMs. Their influence is greatly dictated by AC synthesis conditions such as the temperature of carbonization, temperature of activation and activating agents (131). Consequently, utilizing AC in MMM synthesis has an impact on some surface properties such as wettability, hydrophilicity, hydrophobicity, porosity, surface roughness, polarity and surface charge.

Wettability is a surface property that describes the ability of interaction between a solid and liquid phase, and it is greatly affected by the hydrophilicity and hydrophobicity of the solid phase (2). Wettability can be determined using the surface tension values obtained by

measuring the contact angle between the solid phase (the membrane) and the droplet of liquid on the surface. Hydrophilic surfaces tend to have high surface tension values and they are characterized by the existence of active functional groups that have the ability to form bonds with the fluid (2).
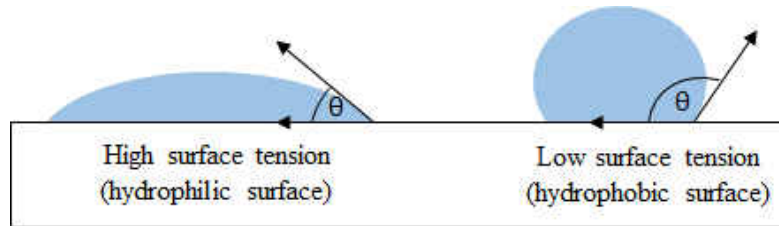
Figure 9: Example of the relationship between contact angle, surface tension, and hydrophilicity of membrane surfaces.

On the other hand, hydrophobic surfaces have a tendency to have low surface tension values and are characterized by the lack of the active groups. As the contact angle decreases, the surface tension increases which leads to a more hydrophilic membrane (2). On the contrary, increasing the contact angle decreases the surface tension and hence results in a more hydrophobic membrane.

It is important to note that the hydrophilicity and hydrophobicity of AC, as well as additives, in a casting solution are the main factors that govern the wettability of a membrane. The introduction of hydrophilic AC tends to create more hydrophilic surfaces (122), whereas hydrophobic AC results in more hydrophobic surfaces (95). This is dictated by the functional groups present in the AC and their electrostatic interaction with the polymer matrix. Localized electrostatic interactions can cause a shift in electron distribution, creating a more or less polar surface (132). Another possible mechanism to this trend is the migration of AC to the surface, and ultimate rupture, can leave the AC surface exposed (123). The exposure results in high degrees of contact between working fluid and the AC. Thus, the wettability of the MMM surface is defined by the wettability of the AC. Furthermore, the use of surfactants in the

casting solution has shown to be the dominant factor, preventing shifts in contact angle regardless of AC loading, as demonstrated by Aghili et al. (121). This is likely due to the smoothing effects of surfactants, leaving behind a smooth surface, while preventing surface migration of AC, balancing any influence of AC (133,134).

Porosity is a surface physical property indicative of the void fraction in a material or on a materials surface. As the amount of AC increases in a synthesized MMM, the membrane becomes more porous which results in a higher flux (120,122). This effect can be potentially attributed to the fact that AC can locally break surface tension, which results in the creation of surface pores in its vicinity. By increasing the frequency of this phenomena through increasing the loading of AC, porosity can be greatly increased (121). This property could be beneficial in the separation of solutes from liquids due to increased wettability and pores available for liquid penetration. In gas separation, on the other hand, porosity if most closely resembled by the FFV, in which gas permeability is highly dependent. AC inherently adds FFV within the membrane due to the highly porous nature of AC. The particles tend to increase the gaps between entangled polymer chains, providing more space for diffusive transport. AC also tends to adsorb high affinity gases. This results in higher rates of diffusion and solubility, hence improved permeation, as was demonstrated by the study by Weigelt et al. (10).

Surface roughness is another physical property that is a function of the surface texture. Generally, there is a directly proportional relationship between the amount of AC loaded and the surface roughness. This typically results in higher fluxes as a result of increased specific area. This increase in surface roughness is attributed to higher surface pore density and uneven settling in the polymer phase caused by the presence of AC and particle agglomeration (121). AC with higher surface area can cause rougher surfaces compared to AC with lower surface

area as was shown by Anson et al. (15) and Marchese et al. (124). This is a result of solvent being removed from the pores of AC rather than the polymer. However, surface roughness is usually associated with fouling, an undesirable property that can be mitigated by use of additives. For instance, according to Hwang et al., the addition of PEG to AC-PPSU membranes resulted in lower surface roughness. In membranes with 0.25% AC, the surface roughness was 360.0 without PEG, 72.1 with 6% PEG, and 119.0 with 12% PEG (120).

Polarity is a significant property in membrane science for gas separation. It can be described as an uneven distribution of charge across a molecule where it is believe to govern the gas solubility and the membrane selectivity (131). For instance, the polarity of a surface tends to increase due to the presence of oxygen complexes on the surface of AC, which impacts the sorption properties of the surface (131). In order for a gas to permeate, the polarity of both the membrane and the gas should match. This means that MMMs with AC tend to permeate more polarizable gases or vice versa depending on the polarity of AC-MMM.

Surface charge generally originates from the dissociation of ionizable groups present at the surface (2). For example, small anions are negatively charged because they are more polarizable than cations and tend to adsorb on hydrophobic surfaces (2). Moreover, surface charge and electric potential are both pH dependent where they shift from negative to positive as the pH decreases from basic to acidic (2). The surface charge is an important property in membrane characterization because it usually correlates to the tendency of fouling or even the state of fouling on membranes (2). Therefore, the more positively charged the surface is, the higher the fouling is in the membrane.

6. Application of AC-MMMs

Various separation applications have been investigated with AC-MMMs. Table 5 summarizes the most relevant recent studies, in terms of the membrane matrix, AC material, and the intended application. Significant findings are highlighted and detailed in following sections.

Table 5: Summary of most recent separation applications using AC-MM membranes with particular emphasis on the type of matrix used, AC source, method used for activating the derived carbon, and whether AC was commercial or synthesized in-house.

Matrix	AC Precursor	Activating Method	AC Vendor	Application	Ref.
PSF	Bagasse	Biochar was not activated	In house	Cu^{2+} and Pb^{2+} removal from water	(122)
PSF	Palm kernel shells	Not listed	Not listed	Ag^+, Pb^{2+}, Cd^{2+}, Cr^{3+} removal from water	(135)
PES	Bamboo	Not listed	US Research Nanomaterials, Inc., Houston, USA	Cu^{2+} and $(SO_4)^{2-}$ removal from water	(123)
PES	Polish subbituminous coal	Steam activation	In house	Cu^{2+} removal from water	(136)
CTA	Not listed	Not listed	Carbochem, LQ1000	Uranium removal from water	(137)
CTA	Not listed	Not listed	Norit NC-100	Uranium removal from water	(138)
PPSU	Acacia fumosa seed	HCl, functionalized with alginate	In house	Phenol removal from water	(99)
CAP	Not listed	Not listed	Merck (India) Ltd. Mumbai, India	Phenol removal from water	(91)
PSF	Not listed	Not listed	Merck (India) Ltd., Mumbai, India	Benzene, Toluene and Phenol, removal from water	(13)
PPSU	Coconut shell	Not listed	China Activated Carbon Industries Ltd., Taiwan	Humic acid removal from water	(120)
PSF	Broom sorghum	$ZnCl_2$	In house	Organic matter removal from cheese whey wastewater	(121)
CNF	Olive stones	KOH	In house	*E. coli.* removal from water	(78)

PES	Not listed	Not listed	Norit A Supra EUR, Norit Netherlands B.V., The Netherlands	Removal of creatinine from blood plasma	(111)
PES	Not listed	Not listed	Norit A Supra EUR, Norit Netherlands B.V., The Netherlands	Removal of creatinine, HA, IS, and PCS from blood plasma	(112)
PDMS	Not listed	Not listed	US1074 US-Nano Company SouthBend,IN,US	Pervaporation of butanol	(109)
PDMS	Tree biochar	Grafted with KH-550 and YDH-171	In house	Pervaporation of ethanol	(95)
ABS copolymer	not listed	Not listed	Maxsorb, The Kansai Coke & Chemical Co. Ltd. (Japan), Merk (Germany)	Separation of CO_2/CH_4	(15)
ABS	Not listed	Not listed	Not listed	Separation of CO_2/CH_4	(124)
PEBAX 2533	Not listed	Not listed	Permionics Membranes (Vadodara, India)	Separation of CO_2/CH_4	(139)
PEI	Not listed	Not listed	Maxsorb 3000, The Kansai Coke & Chemical Co. Ltd. (Japan)	H_2/CH_4, H_2/CO_2, H_2/O_2, H_2/N_2, CO_2/CH_4, O_2/N_2	(90)
PVC	Not listed	Not listed	Maxsorb 3000, The Kansai Coke & Chemical Co. Ltd. (Japan)	H_2/CH_4, H_2/CO_2, H_2/O_2, H_2/N_2, CO_2/CH_4	(102)
Matrimid	Not listed	Not listed	Blücher GmbH (Erkrath, Germany)	Pairs of He, H_2, O_2, N_2, CO_2, CH_4	(10)
PES	Not listed	Not listed	Aldrich	O_2/N_2	(92)
POMS	Not listed	Not listed	Blücher GmbH	$n\text{-}C_4H_{10}/CH_4$	(89)
POMS	Not listed	Not listed	Blücher GmbH	CO_2, C_2H_6, C_3H_8, $n\text{-}C_4H_{10}$, $n\text{-}C_5H_{12}/CH_4$	(79)
PES	Not listed	Not listed	Envior Chemical® Japan	CO_2/CH_4	(140)
Matrimid	Benzimidazole	Chemical crosslinking	In house	CO_2/N_2	(11)
Matrimid	Matrimid	Not Activated	In House	CO_2/CH_4	(7)

				O$_2$/N$_2$	
Nafion	Polypyrrole	KOH	In house	Methanol fuel cell	(141)
Nafion	Not listed	Post processed by acidification and PEG modification	Osaka Gas Co. Ltd.	Methanol fuel cell	(142,143)
Nafion	Glucose	steam	In house	Methanol fuel cell	(144)

6.1. AC-MMM uses in Water Purification

6.1.1. Rejection of Heavy Metal Ions

Due to the excellent adsorption capacity of AC, many researchers have investigated AC-MMMs for heavy metal ion rejection. In doing so, the selectivity of the matrix material, as well as the adsorption of the AC, are exploited to result in typically better rejection and permeation compared to the neat membrane or AC alone.

Jinsong et. al., reported 93.7-100% rejection of Cu^{2+} and 95.2-100% rejection of Pb^{2+} with a flux of near 33 LMH using a PSF hollow fiber membrane loaded with biochar (3-50 microns from sugarcane bagasse) (122). They also reported a recovery rate of 140 Lm^{-2} of water from Cu^{2+} solution and 1500 Lm^{-2} from Pb^{2+} solution before the defined breakthrough point (122). In another study by Hosseini et. al., PEI matrix with nano size AC were tested for copper and sulfate ion rejection; where membranes with 0.5 wt.% AC rejected copper ions at 96% and sulfate ions at 94% (123). Both studies observed an increase in flux compared to the pristine membranes with acceptable rejection of both Cu^{2+}, Pb^{2+}, and sulfate; completely attributed to adsorption onto the AC fillers. A different study by Hofman et al. detected differences between using biochar and AC from coal using a PES matrix due to acid functional groups in the AC (136). Biochar was more effective in removing Cu^{2+} at initial concentrations

below 10 mg/L, and the AC loaded membrane was more effective with initial concentrations greater than 15 mg/L (136).

PSF loaded with AC from palm kernel shells showed a permeability/rejection tradeoff for Ag^+, Pb^{2+}, Cd^{2+}, and Cr^{3+}. Pristine PSF membranes showed low flux, but near 100% rejection of all ions. Flux increased from about 10 LMH to 50 LMH as AC loading was increased from 0% to 0.9%, but major decrements in rejection for all species were observed (135). The optimal AC loading was suggested to be 0.3 wt.% in which rejection followed the order: $Cd^{2+} > Cr^{3+} > Ag^+ > Pb^2$. This is nearly consistent with the order of ionic radii, which would indicate size exclusion rejection. However, Cd^{2+} has the smallest ionic radius but had the highest rejection. This is likely because it could easily penetrate the matrix, but was chemisorbed by the AC. This along with higher rejection with increasing AC loading indicated that size exclusion and adsorption played an important role in the rejection of each ion (135).

With adsorption being the principal mechanism of heavy metal ion rejection, regeneration of the AC within the membrane becomes an issue. Chemical regeneration is required to remove metal ions from AC, but the matrix material must also be considered to prevent damage. He et al. showed that regenerating spent AC-MMMs with nitric acid resulted in acceptable performance, observing a decrease in rejection of Cu^{2+} from 93% to 87% and of Pb^{2+} from 95% to 86% after regeneration (122). Nevertheless, more studies are clearly still needed to better resolve the regeneration issue and comfortably proclaim that the hurdle has been cleared.

6.1.2. Rejection of Uranium

While some conventional separation methods to remove U from water (absorption, ion exchange, precipitation) can be used, they typically only have high rejection when treating solutions with high U concentrations (on the order of ppm) (137,145). However, U typically exists in relatively low concentration in water (on the order of ppb), making it difficult to remove using these methods. MMMs have been demonstrated to capture U from water at these lower concentrations via a combination of size exclusion and adsorption.

Rodriguez et al. investigated a CTA membrane with micron sized commercial AC for dilute (0.7 ppm) U removal (4). Membranes with 3 wt.% AC loading achieved the highest U removal of 41% with a feed pH of 7. The flux across the membranes averaged 363 LMH/bar. The high flux and high rejection, despite agglomerates and apparent pH rejection dependence, indicate adsorption of U on the AC was the predominant mechanism of separation.

The same group was able to increase the U removal of dilute solutions to 50% by introducing iron into the uranyl feed solution or by incorporating iron into the AC by chemical impregnation (138). This effect also indicated that adsorption dominated rejection. Additionally, in using the MMM with iron doped AC, homogeneous dispersions of AC were achieved, which allowed for more efficient adsorption. Although adsorption appeared dominant, the group noted complex rejection behavior for various species in the uranyl solution with varying pH, indicating size exclusion was also present.

6.1.3. Rejection of Aromatic Compounds

Phenol is a high priority water pollutant that is commonly studied (146). The removal of phenol from water can be achieved with both ultrafiltration and adsorption using MMMs, making them an ideal class of membrane for this process.

Saranya et al. used a PPSU matrix with functionalized AC from *acacia fumosa* seeds for the removal of phenol from water (99). Functionalizing the AC aimed to prevent agglomerations in the casting solution and ultimately within the membrane and to increase rigidity to maintain active sites for adsorption. The pristine polymer had nano-sized surface pores when cast and precipitated by wet phase inversion, as has been documented before (147,148). The surface pore size increased to nearly one micron until the surface became dense with 1% loading of AC. This indicated that even with functionalized AC, agglomerations still formed at high loadings and pore blockage by AC become more apparent.

The phenol rejection efficiency by the MMMs was found to increase with AC loading. However, the amount of phenol adsorbed by the AC decreased with higher loadings (99). This indicated that active adsorption sites became less available, marking a shift between adsorption dominated rejection to a combination of adsorption and size exclusion. The flux first increased from 14.5 LMH in the pristine polymer to 26.9 LMH in the 0.25 wt.% functionalized AC loading and then decreased as the loading increased to 1 wt.% as a direct result of decreased porosity and fewer surface pores.

The use of nano sized (750 nm) AC seemed to prevent agglomeration in a CAP membrane, allowing for 25 wt.% loading (91). A flux of 64 LMH flux and 96% rejection for phenol was attributed to an increase in both specific surface area and hydrophilicity compared

to the pristine membrane due to the AC. These two properties appeared to maximize the flux

and active sites available for adsorption as depicted in Figure 10.
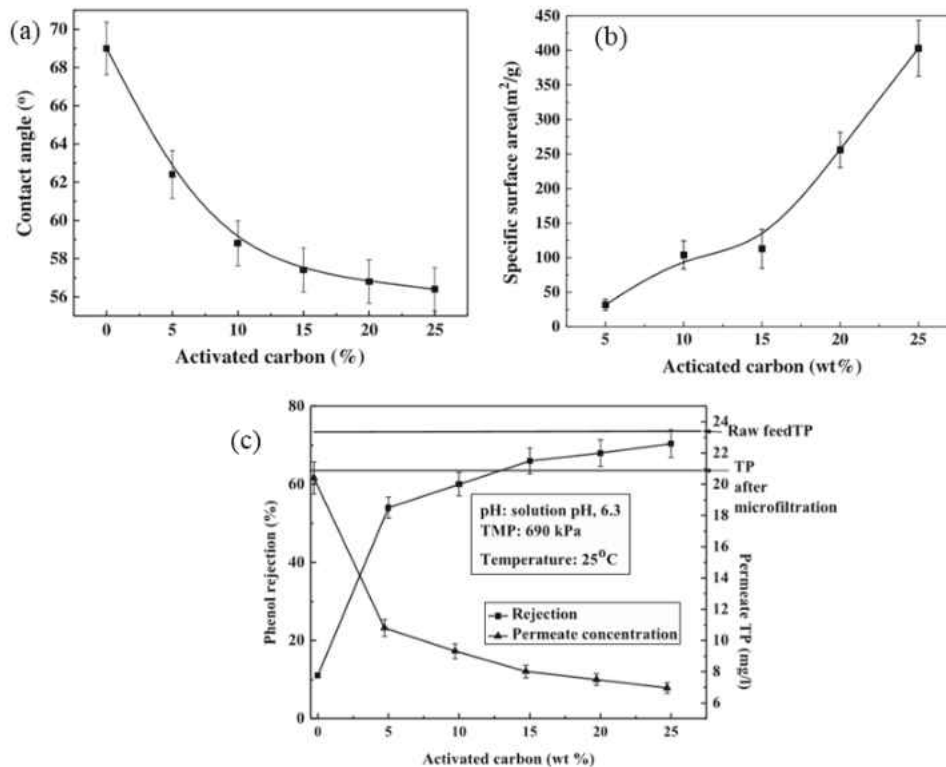
Figure 10: Influence of nano sized AC on (a) contact angle, (b) specific surface area, and (c) phenol rejection on an AC-CAP MMM (91). TP is the total phenol concentration. The secondary y-axis in (c) demonstrates the raw feed TP, TP after microfiltration with unloaded membranes, and the permeate TP using various loadings of AC. The steep decline from 23 TP in raw feed to 21 TP after microfiltration to 7 TP in the 25 wt.% AC-MMMs demonstrate the improved rejection performance. Reprinted with permission from Wiley.

Despite the high concentration of AC near the membrane surface, fouling was still present and

10% reduction in flux was seen even after acid-alkali regeneration, indicating irreversible

fouling (91).

The same group also investigated a 70 nm AC in a hollow fiber PSF matrix (13).

Although surface pores were visible in the pristine and low loaded membranes, they noted a

decrease in surface pore volume at AC loadings larger than 1 wt.% as a result of pore blockage

(13). As noted before, the addition of AC lead to a more hydrophilic membrane, however, the

PWF decreased with increasing AC loading. This signifies competition between pore blocking

and surface hydrophilicity on flux. In this case, the pore blockage was more dominant, restricting flux.

They also found that a membrane with 2 wt.% AC was optimal in terms of flux and adsorption of benzene, toluene, and phenol. The pH dependent rejection was attributed solely to adsorption by the AC, and was a maximum of 96% for benzene, 88% for toluene, and 80% for phenol at a pH of 4 (13). The influence of pH was shown to influence the zeta potential of the MMM surface. Acidic solutions resulted in higher zeta potentials. Thus, less polar molecules could more easily be adsorbed by the AC in the MMM. Hence, the lower rejection for phenol was primarily caused by its negative -OH functional group, limiting its adsorption. The $-CH_3$ group on toluene is slightly less negative, promoting higher adsorption than phenol. The absence of negative functional groups on benzene was the reason for its high adsorption.

Another aromatic water pollutant that has been investigated by AC-MMMs is humic acid. The rejection of humic acid is commonly probed in membrane applications because it is a major source of fouling on many polymeric membrane materials (16,149,150). A study by Lin-Luen et al. used a PEI-PPSU polymer blend, which was loaded with 0.25wt.% AC from bamboo and 6 wt.% PEG as a pore forming agent, to achieve a removal efficiency of 84%, as shown in Figure 11 (120). The addition of PEG not only helped create a spongy cross section with surface pores, but additionally helped in reducing surface roughness caused by the addition of AC. In membranes with 0.25 wt.% AC, the surface roughness was 360.0 without PEG, 72.1 with 6 wt.% PEG, and 119.0 with 12 wt.% PEG (120). This is an interesting observation since rougher membranes typically lead to higher degrees of fouling. Hence, adding PEG can potentially mitigate fouling. Membrane porosity was also improved by the addition of AC as measured by PWF. As the AC loading increased from 0.25 wt.% to 1 wt.%

without the addition of PEG, the PWF increased from 271 to 535 LMH (120). The exception

was in membranes with 0.50 wt.% AC, adding 12 wt.% PEG into the casting solution slightly

increased the PWF from 428 to 452 LMH (120).
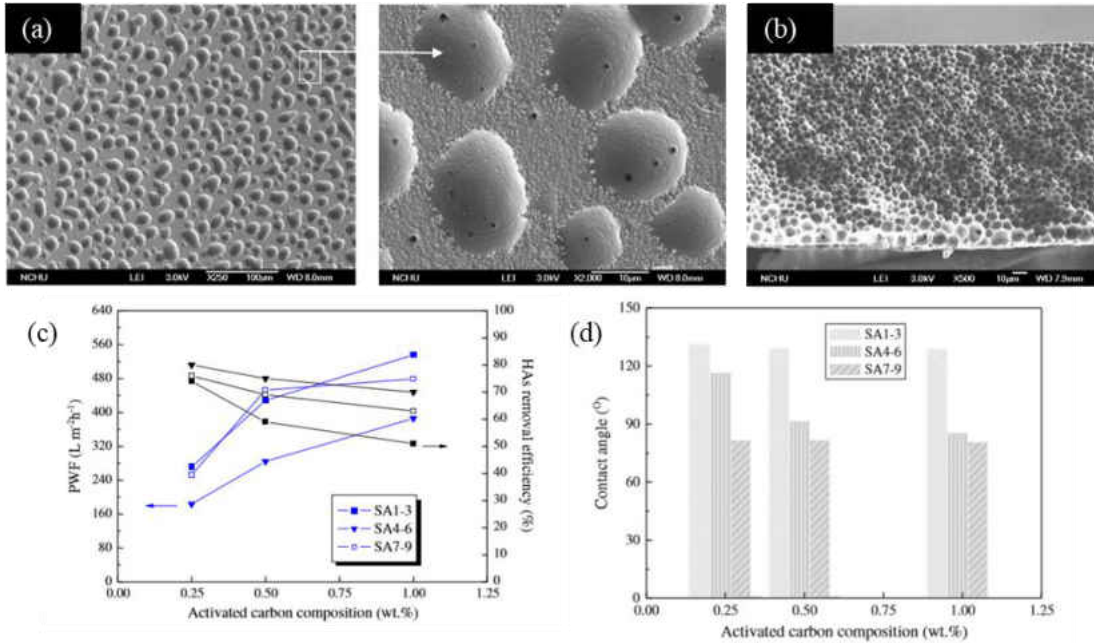
Figure 11: (a) Crater-like morphology formed on the tope surface of PEI-PPSU blended AC-MMM and the resulting (b) cross section. The influence of AC on (c) PWF and humic acid removal efficiency and (d) contact angle. Membranes were formed with 35 wt.% PPSU and 5 wt.% PEI. PEG pore forming agent was not used in samples SA1-3, 6 wt.% was added to SA4-6, and 12 wt.% to SA7-9. Each series of samples contains 0.25, 0.5, and 1 wt.% AC (120). Reprinted with permissions from Elsevier.

6.2. AC-MMM uses in Biological Solute Rejection

6.2.1. Removal of organic Matter

PSF matrix loaded and coated with powdered AC (<74 microns from sorghum) proved to be

effective for the removal of organic matter from cheese whey wastewater (121). The rejection

was quantified in terms of COD and UV_{254}.

AC-loaded membranes showed improved rejection of COD and UV_{254} shown in Figure

12a. The COD rejection increased from 38% in neat membranes to 44% in 0.5 wt.% AC-

MMMs. Similarly, UV_{254} removal increased from 42% to 48%. A rejection decline in both was seen with 1 wt.% AC-MMMs. The waste water flux, shown in Figure 12b, was similar in membranes loaded with 0.1 and 0.5 wt.% AC, and was higher than both the neat membrane and the membrane loaded with 1 wt.% AC (121). Though, all membranes showed a decline in flux with time, indicating pore blockage and cake formation on the membranes.
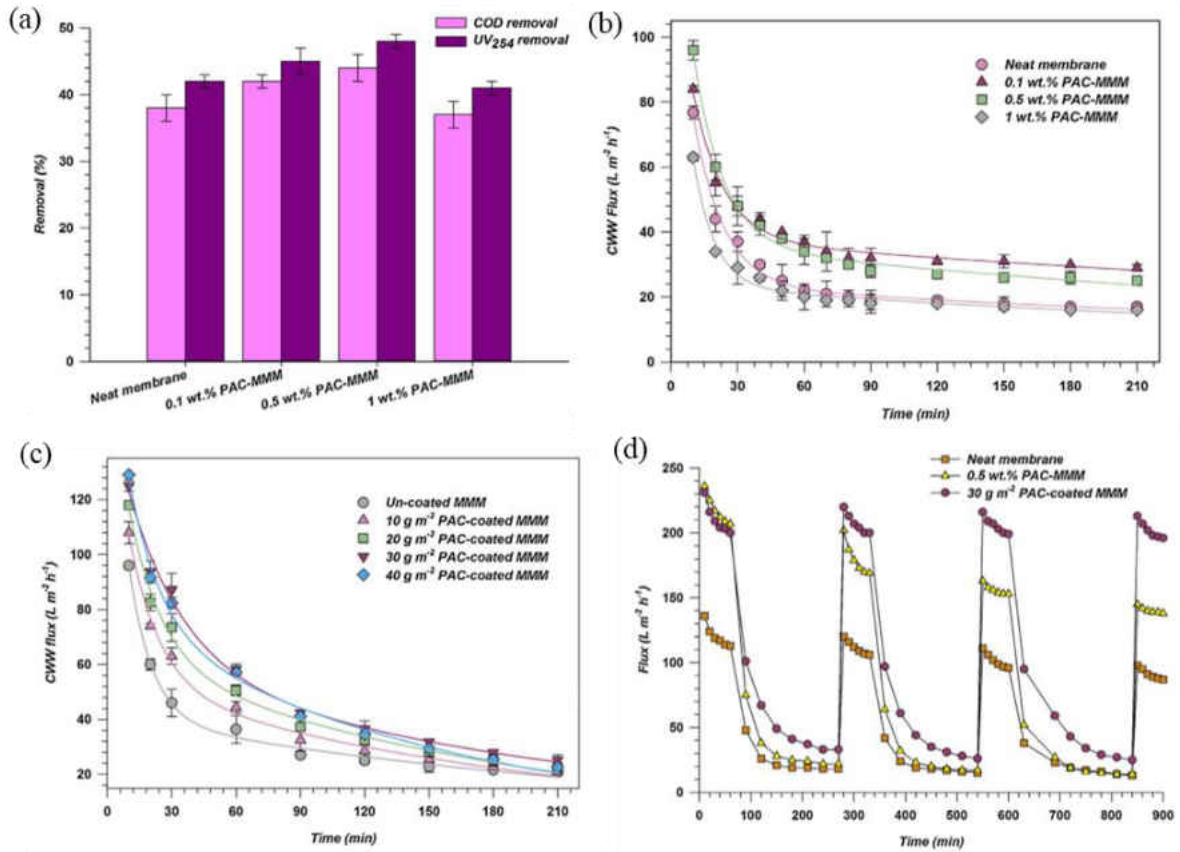
Figure 12: Influence of AC on (a) organic solute removal and (b) clean water flux over time. The influence on coated AC-MMMs on (c) clean water flux over time, and (d) improved regeneration ability (121). Reprinted with permission from Elsevier.

To combat cake formation, AC was used to coat the 0.5% loaded membrane. When coated with 30 g/m^2 AC, rejection increased to about 80% due to the additional sites for adsorption. In membranes coated with more than 30 g/m^2, there was no increase in rejection due to AC agglomeration leading to fewer active sites (121). Surprisingly, the waste water flux increased proportional to the amount of coating despite the extra thickness caused by the added

layer. The coated membranes still showed a flux decline with time, indicating fouling was still present. However, after physically cleaning the surface, the waste water flux returned to near its original value before filtration. As shown in Figure 12, the flux of the coated membrane remained constant after cleaning, whereas the neat and uncoated membranes saw a flux decline after cleaning. This means the irreversible fouling was reduced by coating the MMMs with AC.

6.2.2. *E. Coli* Removal

Considering *E. coli.* is relatively large (0.5 microns wide by 2 microns long) and leaves membranes susceptible to bacterial growth over time, antimicrobial membranes with relatively large pores can be advantageous.

Hassan et al. investigated a novel MMM configuration made with two layers for the removal of *E. coli.* (78). It consisted of oxidized CNF intertwined with AC deposited on a porous paper support covered in un-oxidized CNF and a PAE crosslinking agent. Two methods of formation were investigated. 1) direct drying and 2) rinsing with isopropyl alcohol prior to drying. Drying with isopropyl alcohol resulted in membranes with a more porous surface (78). The membrane with AC in the bottom layer was more porous than membranes without the AC in the bottom layer.

In the membranes formed by direct drying, adding the AC layer enhanced PWF, from 55 LMH without AC to 158 LMH with AC, due to pore formation in the CNF layer even though the AC was not directly introduced into that layer. Increased PWF was observed with the isopropyl alcohol drying, and the membrane with AC showed relatively higher PWF as they saw an increase from 165 LMH to 425 LMH as a result of the AC. The flux with bacteria

suspensions was significantly lower, at 139 in CNF and 345 in CNF-AC, which was a result

of pore blockage by the bacteria (78). The removal of *E. coli.* was slightly improved from 97%

to 99% with the addition of AC, as a result of adsorption by the AC layer. They found that the

CNF-AC membranes were antibacterial, showing no growth after 24 hrs. at 37°C (78).

6.2.3. Blood Plasma Toxin Removal

In purifying blood plasma, it is crucial to prevent contamination, thus AC presents some

hazards as AC-MMMs pose the risk of particles breaking free and entering the passing fluids

(151). One method to ensure this does not happen is by using a two-layer membrane with a

pristine polymer on one side.

A two-layer PES-PES/AC membrane was investigated for the removal of creatinine

from blood plasma by Tijink et. al. and is shown in Figure 13(a) (111). The particle free PES

layer was used to ensure AC was not mixed with the retentate. This two-layer architecture was

achieved using an adjustable co-casting knife. The cross sections were influenced by a PVP

additive in the casting solution, and 60% NMP in the coagulation bath for the phase inversion.

They showed that between 50-70% AC relative to the PES could be loaded while maintaining

a spongy cross section (111). This architecture observed decreased water permeance from 1839

LMH/bar in the single layer MMM to 350.7 LMH/bar in the dual layer. This is likely a result

of the surface of the particle free layer adding resistance to flow. The particle free layer did not

reduce creatinine concentrations, whereas the single layer MMM and dual layer particle free-

MMM reduced concentrations by about 80% (111). This was compared to creatinine

adsorption on the AC alone, and was similar, indicating that the active sites on the AC in the

MMMs were readily accessible (111). Both diffusion of creatinine through the membrane as

well as adsorption by the AC was simultaneously responsible for the removal of creatinine

(111). It is important to note that this removal was accomplished without major changes in plasma osmolality, pH, or total protein concentration. Major changes in these values would be detrimental to dialysis patients.
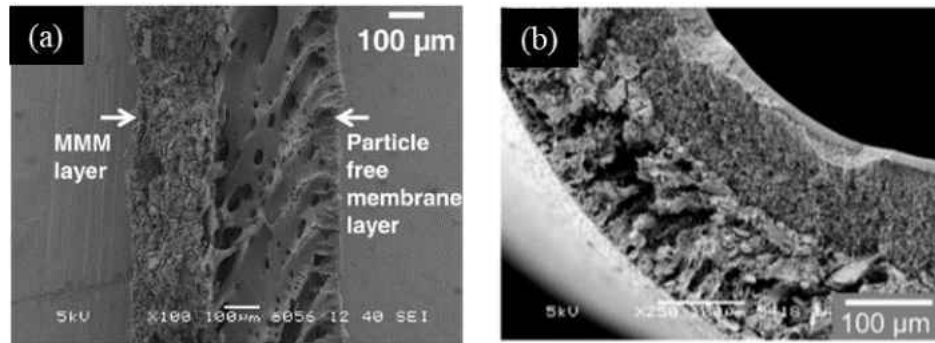
Figure 13: Two layer PES-PES/AC (a) flat sheet and (b) hollow fiber membranes (112). Reprinted with permission from Elsevier.

Tijink et al. also studied the removal of other toxins from plasma with a two layer hollow fiber membrane depicted in Figure 13(b) (112). This configuration was achieved using a triple layer spinneret. PES/PVP/AC membranes were fabricated by the dry-wet spinning method in air and further precipitated in PVP or NMP solutions. They observed good dispersion of AC with no macro void formation. Using a 5% PVP in water solution as the bore fluid resulted in a circular bore, whereas using only water resulted in irregular shapes (112). The membrane with the highest pure water permeance was made with the NMP containing bore fluid and was used throughout the study. The clean water permeance was 58.4 LMH/bar and it was shown that no delamination or AC losses occurred.

Creatinine was investigated as the water soluble toxin. HA, IS, and PCS were also investigated and represented PBTs (112). The creatinine adsorption by the hollow fiber membrane of 100 mg/g was higher than the flat sheet configuration at 29 mg/g for the same feed concentration. Creatinine, HA, IS, and PCS all showed similar adsorption capacities in the dual layer MMM as was also observed in the AC alone, indicating good accessibility. In

cross flow measurements, nearly 40 mg/g (creatinine/membrane) was removed after 4 hours.

The removal of PBTs in cross flow was mostly attributed to adsorption on the MMM. This is in contrary to creatinine rejection, which combines adsorption with diffusional effects. Removal, in mg PBT per gram of membrane, was about 14 for HA, 3.5 for IS, and 2.3 for PCS (112). It is important to note that albumin was able to pass through the membrane and osmolality decreased over time. However, no changes in pH or salt concentrations were detected.

6.3. AC-MMM uses in Pervaporation

Pervaporation has frequently been investigated for the dehydration of organic compounds, especially alcohols. This process offers a unique cross between liquid and gas phase separation because both phases are in contact with the membrane. Thus, the rejection of a polar liquid species on the surface and the diffusion of a less polar gaseous species in the free volume of a membrane is required. This provides an interesting challenge for AC-MMMs due to the AC influence on surface hydrophobicity and free volume. Moreover, as most AC-MMMs result in hydrophilic surfaces, modifications to the AC are required for enhanced properties.

Lan et al. investigated the modification of biochar created from lodgepole pine bark with KH-550 and YDH-171 (95). The nano-sized "grafted biochar" was loaded into a PDMS membrane and cast on a cellulose acetate support and allowed to precipitate in air for 24h. The grafting resulted in weaker –OH stretches in the biochar, and ultimately an increase in water contact angle and a decrease in ethanol contact angle in the MMMs. These changes indicated that the neat membranes became more hydrophobic with the addition of grafted biochar and has a stronger affinity toward ethanol (95). The hydrophilicity on the YDH-171 was stronger

than KH-550 due to the presence of a hydrophilic -NH$_2$ in KH-550. Likewise, MMMs with YDH-171 showed stronger compatibility with ethanol.

Both biochars showed an increase in flux with an increase in loading up to 4 wt.% due to an increased free volume. However, the separation factor decreased in both cases after 3 wt.% likely due to the formation of macrovoids within the membrane. An increase of ethanol in the feed solution resulted in lower flux but higher separation factors. MMMs loaded with 3 wt.% biochar at 40°C and 10 wt.% ethanol feed concentration performed best. The YDH-171 MMM performed relatively better with a separation factor and flux of 11.3 and 227 LMH. The KH-550 MMM had a 10.1 separation factor and a flux of 225 LMH (95).

Another AC that resulted in MMMs with stronger affinity toward the alcohol was nano sized (20-40nm) AC with higher specific surface area (1400 m^2/g) (109). When fabricated by the dry phase inversion method, the addition of AC resulted in a rougher PDMS surface, increased degree of swelling, and an increase in water and butanol contact angle caused by the AC (109). A lower contact angle was seen with butanol than water, indicating higher affinity of butanol with the membranes. The permeability of both butanol and water increased when AC loading was increased from 0 to 6%, but then decreased slightly at 8% loading. However, the separation factor increased for the entire range of AC loadings (109). The decrease in permeability from 6 to 8% loadings was likely the result of agglomeration forming within the membrane, creating a longer path for diffusion. Optimal results were seen at 6% AC loading with a butanol permeability of 9.49x10^{-7} g cm/s cm^2 bar. Separation factor increased with increasing temperatures within the range of 37-57°C.

6.4. AC-MMM uses in Gas Separation

The use of MMMs has especially attracted attention for gas phase separations due to the permeability/selectivity limitations of polymeric and inorganic membranes. MMMs offer multiple mechanistic pathways (152) capable of exceeding the permeability and selectivity upper bounds suggested by Robeson (153). Moreover, Chuah et al. recently formulated a metric for MMM performance based on filler/matrix properties (154). They presented an "F-index" which quantifies improvements in permeability and selectivity. AC and CMS MMMs consistently showed F-index values greater than 1 with many polymers, meaning they are likely to improve both permeability and selectivity in MMMs.

Although Robeson's upperbounds were correlated specifically for membranes undergoing solution diffusion, AC-MMMs are often compared to this upperbound (10). However, the use of this comparison may not be accurate not only because of the mechanistic difference, but also because of the difficulty in establishing and measuring the active layer used in the permeability calculation. Nonetheless, AC-MMMs have shown promising results for two classes of gasses: small, low molecular weight, non-polar gas mixtures and higher hydrocarbons.

6.4.1. Small, Low Molecular Weight, Non-Polar Binary Mixtures

The gas pairs consisting of a combination of He, H_2, O_2, N_2, CO_2, CH_4 present some of the most difficult, industrially relevant gases to separate due to their similar size, polarity, and low boiling points. The use of AC-MMMs has yet to be exceptionally successful in their separation, however, many important studies offer insight into their behavior.

The influence of AC size was investigated in an ABS copolymer membrane for CO_2/CH_4 separation (15). Two AC of different particle size were utilized. The AC with lower surface area and larger size ultimately lead to better CO_2/CH_4 permselectivity. However, more filler was needed to achieve this. It was suggested that poor polymer filler interaction was improved by the butadiene-styrene block in the matrix. Both CO_2 permeability and CO_2/CH_4 selectivity was improved with the addition of AC particles. Higher loadings led to further increases in permselectivity up to 10 wt.% in the smaller AC, and 40 wt.% in the larger AC (15). Increases in permeability and selectivity were attributed to selective surface diffusion through the pores of the AC. This is reasonable considering CO_2 is the more adsorbable of the two species. The use of dry phase inversion technique was critical to the increase in permeability, as nano-sized pores and surface roughness were enhanced with the addition of AC (15,124). Moreover, AC with higher surface area and pore volume resulted in increased roughness due to the solvent being eliminated from pores in the AC rather than from the polymer (124). This results in localized variation in mass transfer around the AC particles, creating a higher tendency for node and valley formation compared to pristine membranes (155).

The influence of particle surface area was opposite to this finding in a Matrimid-CMS MMM. Two different CMS nanoparticles (1079 and 538 m^2/g BET) showed similar performance when used for CO_2/N_2 separation (11). In this case, the gas diffusion through the particle/matrix void space was more significant than the diffusion through the particle pores. None the less, membranes showed improved performance compared to pristine Matrimid, with a 14.9 barrer permeability and 38.9 ideal CO_2/N_2 selectivity (11).

On the other hand, a PEBAX matrix loaded with 25 and 50 wt.% (relative to the polymer phase) AC saw a different trend (139). Similar CO_2/CH_4 selectivity was seen in the neat and 25 wt.% loaded membranes, but a large drop in selectivity was observed at 50 wt.% loading. CO_2 permeance was the following order: neat PEBAX<25%<50%. The increase in permeability was attributed to diffusion through the pores of the AC as well as unselective void space in the 50 wt.% loaded membrane (139). This is further evidence that there is an optimal loading before the formation of unselective void space.

Garcia at el. also studied AC loaded in a PEI matrix (90). Using optical microscopy, they were able to determine that 2% loading of AC resulted in homogeneous dispersion of AC in the PEI. At higher loadings, agglomerations were observed by measuring visible particle size and comparing it to the original particle size distribution. (90). It was also shown that the d-spacing decreased with increasing AC loadings, likely the result of rigidification of the polymer structure. They also saw an increase in pure gas permeability in all pure gases tested with increased AC loading. A simultaneous increase in selectivity for H_2/CH_4, H_2/CO_2, and O_2/N_2 gas pairs was also observed, resulting from a decrease in the diffusion coefficient and an increase in solubility due to preferential sorption of O_2, CO_2, and CH_4 in the AC particles (90).

The same group studied a PVC membrane cross-linked with a difunctional amine: 4,4'-oxidianiline loaded with AC up to 60 wt.% (102). After creating the casting solution, AC agglomerations were filtered. They noted that the top and bottom surface of membranes loaded with 60% AC were similar and contained visible void spaces around the AC (102). Using a crosslinking agent favored the formation of a less permeable porous structure. X-ray diffraction revealed that cross linked membranes had a lower degree of crystallinity aided by AC loading.

Thermogravimetric analysis showed that as the AC content reached 60 wt.%, the thermal behavior was dominated by AC rather than matrix phase. Increasing amounts of cross linking and AC loading also influenced an increase in gas permeability as predicted due to void spaces in the membrane surface (102). Membranes loaded with 60% AC showed Knudsen selectivity as a result of that void formation. However, their selectivity was dissimilar to the Knudsen selectivity in cross-linked membranes with 23 wt.% AC. They suggested a combination of sorption-diffusion and Knudsen diffusion was observed (102).

Another study demonstrated that a reduction in surface defects was shown to occur by using a dry/wet phase inversion method on an AC loaded Matrimid matrix (10). Solvent and non-solvent were chloroform and methanol. Good polymer-AC interaction was verified by an increase in glass transition temperature with an increase in AC loading (10). Despite the AC causing a rougher surface than pristine membranes, the AC tended to accumulate near the bottom of the membrane due to settling during the dry phase inversion step.

For all gases, there was an increase in permeability with increased AC loading and very small changes in selectivity for most gas pairs. A significant difference between the measured selectivity and the predicted Knudsen selectivity showed that solution diffusion was the primary mechanism, attributing the increase in permeability as a result of adsorption and surface diffusion through the AC (10).

The formation of void spaces with high amounts of AC was also apparent in a PES matrix. With 10 wt.% AC, macrovoid formation was present as a result of poor compatibility (92). The O_2 and N_2 permeance was higher in the MMMs than pure PES, showing increased transport proportional to increased AC loading until 10%. A similar trend was seen in O_2/N_2 selectivity, where an increase in selectivity was observed with membranes made with 1 and 5

wt.% AC followed by a decrease at 10 wt.%. Still, this decreased selectivity was higher than the pure PES (92).

Vu et al. showed that priming of CMS with small amounts of PSF before being placed in contact with dissolved Matrimid helped to decrease agglomeration and interfacial defects (7). Moreover, thermal annealing in combination with priming significantly reduced defects, enabling defect free membranes at loadings of 35 vol.%. Interestingly, this led to an increase in selectivity for CO_2/CH_4 and O_2/N_2 but overall lower permeabilities than the pristine polymer.

Facilitated transport of CO_2 by alkanolamine embedded in dense PES-CMS membranes proved to be highly effective for CO_2/CH_4 separation (81,140). In this case, CMS and the alkanolamine components opened multiple pathways for gas transport through the membrane. Increased loading of the alkanolamine solution resulting in increases in CO_2 permeance while maintaining CH_4 permeance. This resulted in a CO_2 permeance of 117.32 GPU and CO_2/CH_4 selectivity of 20.1 with a membrane made of 20 wt.% PES, 30 wt.% CMS, and 15 wt.% alkanolamine in NMP (81,140).

When compared to MMMs containing other common fillers, CMS and AC-MMMs perform average in the case of CO_2/N_2 and H_2/CH_4 separation. In the case of CO_2/CH_4, O_2/N_2, and H_2/CO_2, several of these membranes showed superior performance. This comparison is shown in Figure 14, where various MMMs were grouped by filler type. Plots were constructed from data listed in various review articles (17,18,20,21,24,82,94,152,156) as well as other recent literature. While the choice of matrix material is of crucial importance, these plots demonstrate the viability of using AC in MMMs. They also highlight the need for more studies, as there is no apparent trend seen in AC-MMMs for these applications.

6.4.2. Higher Hydrocarbons

The separation of higher hydrocarbons (C3+) from methane is also a challenging task is which membranes can compete with existing technologies (157).

Mushardt et al. studied a POMS MMM loaded with AC at 1.5 and 3.5 microns particle size for the separation of $n-C_4H_{10}$ and CH_4 (89). A silicon coating was applied to seal surface defects. Adsorption studies on the AC particles showed that the AC had a higher affinity toward $n-C_4H_{10}$ than CH_4. As the amount of AC loading increased, membrane cross sections became less homogeneous and were more pronounced for smaller AC sizes. Defects were seen with 40 wt.% (relative to polymer) loaded membranes despite silicon coating. Smaller particles tended to result in more frequent defects (89).

That same study also found that the addition of AC led to a reduction in the swelling effect commonly caused by $n-C_4H_{10}$ and a decrease in $n-C_4H_{10}$ permeance proportional to increased AC loading. MMMs with smaller particles showed higher permeance compared to the larger particles. However, membranes with 20 wt.% (relative to polymer) loading showed the highest $n-C_4H_{10}/CH_4$ selectivity. They concluded that particle size had little influence on selectivity, indicating that pore size, not particle size, controlled permselectivity behavior in these membranes (89).
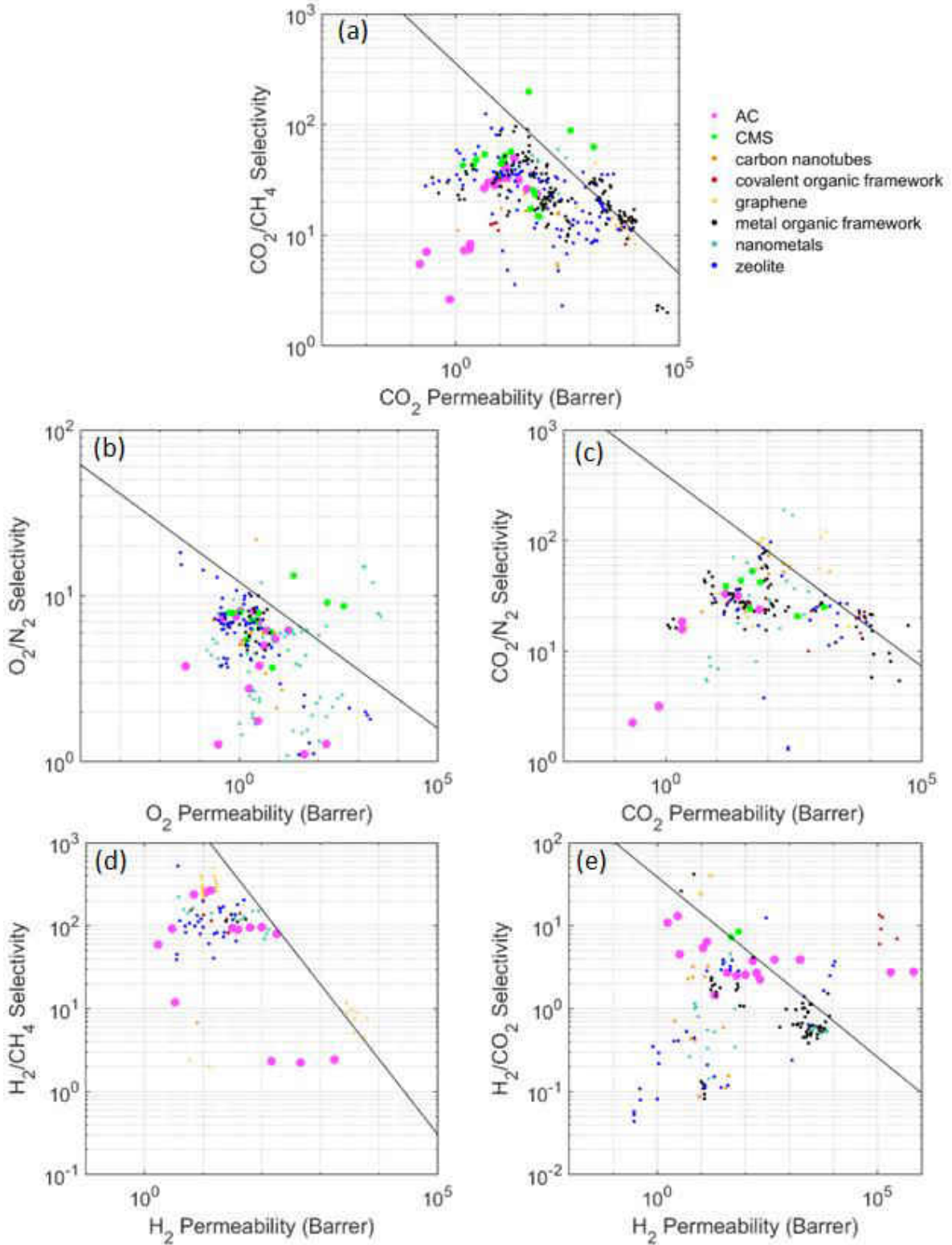
Figure 14: AC and CMS MMMs compared to other MMMs grouped by filler type for (a) CO2/CH4, (b) O2/N2, (c) CO2/N2, (d) H2/CH4, and (e) H2/CO2 gas pairs plotted against Robeson's 2008 upperbounds.

A follow-up from the same group studied the performance properties of mixed gases of higher hydrocarbons using the same POMS-AC MMM (79). They noted that swelling caused by $n\text{-}C_4H_{10}$ uptake played an important role in both permeability and selectivity. Using a mixture of 5 mol% $n\text{-}C_4H_{10}$ in CH_4, they saw higher $n\text{-}C_4H_{10}$ permeance in the pure POMS membrane, but a higher selectivity in the MMM containing 20 wt.% AC. For feeds with less than 2% $n\text{-}C_4H_{10},$ the permeance of $n\text{-}C_4H_{10}$ was lower in the MMMs, and the selectivity was equal for both membranes (79).

They also tested a gas containing 19% of higher hydrocarbons consisting of CH_4, CO_2, C_2H_6, C_3H_8, $n\text{-}C_4H_{10}$, and $_n\text{-}C_5H_{12}$. The permeance of each species followed the condensability, increasing proportionally with the number of carbons. Likewise, selectivity with respect to CH_4 also increased with number of carbons (79).

6.5. Proton Exchange AC-MMMs for a Direct Methanol Fuel Cell

Important parameters in proton exchange membranes for a direct methanol fuel cell are proton conductivity, limited methanol permeability, and overall stability. AC-MMMs contend for this application because the polymer serves to provide flexibility and ion exchange capacity while the AC serves to enhance dimensional, thermal, and mechanical stability and enhance proton conductivity and water uptake (158).

Nafion is the most common membrane material for fuel cell applications. It is typically formed by tradition phase inversion or sol gel methods. AC can be introduced into the casting solution readily before inversion (142,143). Chai et al. utilized a unique method to produce and incorporate AC into a Nafion in a single step. A glucose solution was introduced to a swollen membrane and then hydrothermally reacted to carbonize the glucose (144).

Hydrophilic AC can be used to improve the water uptake in proton exchange membranes. The increase of water in the membrane enhances proton conductivity, improving the performance of the membrane. Several studies have shown this increase. Guo et al. reported an increase from 28% to 48% water uptake with 1 wt.% nano AC (141). A similar increase was observed by Tsai at al., however 15 wt.% AC was need to achieve 65% water uptake (142). Chai et al. further demonstrated the water uptake potential, measuring 140% uptake with a 10 wt.% AC loading (144). At low loadings, this variation with AC loading is the direct result of hydrophilic properties of the AC. At higher loadings, the AC may become agglomerated, reducing active sites available for water adsorption. In turn, the water uptake becomes limited with increasing AC loading. The increase in water uptake and electrostatic repulsion of AC to methanol resulted in an increase in proton conductivity and simultaneous decrease in methanol permeability (144). Importantly, the power density is also influenced by introducing AC. With 3.6 wt.% AC, an increase from 25.2 mWcm^{-2} in pristine Nafion to 36.3 mWcm^{-2} in one instance (144). However, with AC loading exceeds a certain concentration, increased resistance between the membrane and electrode can occur, resulting in a reduced power density. Likewise, too high loading resulted in particle agglomeration leading to poor mechanical performance, hindering the viability of AC-MMM use.

7. Predictive Models

Modeling is regularly needed and used to guide experiments, design specific unit operations, and optimize process. Because of this, many predictive models have been developed for MMMs. A thorough review of these models was conducted, presenting numerous models for MMMs in ref. (152). However, there are no apparent studies that have aimed to develop models specifically for AC-MMMs. This is likely due to the complexity of pore size distribution,

functionality, and irregular shapes of most AC, rendering general predictive behavior difficult to formulate (122). Nonetheless, existing models have shown some accuracy for AC-MMMs and are further discussed.

In liquid phase separation, the rejection of dissolved solutes can be predicted with adsorption isotherms. Several studies have highlighted the similarity between amount adsorbed on standalone AC, and AC-MMMs (4,13,78,122,123)

As AC has traditionally been used as an adsorbent, much research has been performed on isotherm type specifically for heavy metal ions including arsenic (V), cadmium (II), copper (II), mercury, nickel (II), lead (II), magnesium, and zinc (159,160). Typically, a Langmuir isotherm (monolayer coverage) describes the equilibrium adsorption well, although, the Freundlich isotherm (monolayer) is relatively common for high concentration solutions. The Langmuir isotherm also accurately depicts adsorption of larger molecules such as creatinine (112) and phenol (91). It is important to note that these isotherms depict the equilibrium adsorption capacity, making them accurate for cross flow filtration setups with recycled streams. Adsorption kinetics are required to accurately predict rejection with cross flow or dead end filtration systems without recycle streams. Some researchers have found diffusional effects to be slightly influential on predictability, for example with the removal of phenol from water (99) and creatinine from blood plasma (112). The common equilibrium isotherms that help predict liquid separation by AC-MMMs are shown in the following equations:

Langmuir
$$q_e = \frac{Q_m K_a C_e}{1 + K_a C_e}$$
(1)

Freundlich	$$q_e = K_F C_e^{1/n_f}$$	(2)

Temkin	$$q_e = \frac{RT}{b_T}\ln(K_T C_e)$$	(3)

where q_e is the mass normalized equilibrium adsorption amount, Q_m is the maximum adsorption capacity of a solute on AC, C_e is the equilibrium concentration of the permeate, R is the universal gas constant, T is temperature, K_a is the Langmuir constant, K_F and n_f are Freundlich constants, and K_T, is the Temkin constant.

Kinetic isotherms can also be useful for AC-MMMs. With the known AC loading and an estimation of the time constant within the membrane, the permeate concentration can be estimated. Three common kinetic isotherms which have been applied extensively to AC adsorption are shown here in their linearized form:

Pseudo 1st order	$$\log(q_e - q_t) = \log q_e - \left(\frac{k_1}{2.303}\right)t$$	(4)

Pseudo 2nd order	$$\frac{t}{q_t} = \left(\frac{1}{k_2}\right) + \left(\frac{1}{q_e}\right)t$$	(5)

Intra-particle Diffusion	$$q_t = k_d t^{1/2}$$	(6)

where q_t is the mass normalized amount absorbed at a given time, t. k_1, k_2, and k_d are the rate constants associated with each model.

The study of gas adsorption on AC has also been studied. The adsorption of He, H_2, O_2, N_2, CO, CO_2, and H_2O are typically modeled well by isotherms assuming monolayer coverage, specifically Langmuir and Freundlich isotherms. The adsorption of CO_2 on AC has been the major recent application of study, which is more frequently modeled with the Freundlich isotherm (160).

Although isotherms predict equilibrium concentrations and the adsorption capacity of gases on AC, they are rarely used to predict the behavior of gases in MMMs because diffusional effects have a more pronounced effect on permeability and selectivity, and MMMs are rarely studied in transient states. Thus, the adsorption of gases on the AC plays no part in selectivity once saturated. One-dimension mass transfer in two phase systems can be used to model gas behavior, but a number of simplifications and assumptions must then be made regarding diffusion in both phases as well as in the interface between AC and matrix (89). Other models have been used to predict gases permeability in AC-MMMs including the Maxwell, Bruggeman, and GPG models. Although these models have not shown to be extremely accurate in AC-MMMs, they are simple to solve, and have shown acceptable results when compared to some experimental data.

The Maxwell model, which was originally developed to predict the electric conductivity of composite materials, was adopted for permeability of gases and is accurate for dilute particle loadings up to 20 vol.% (10). The Bruggeman model more accurately predicts the permeability of AC-MMMs with medium particle loadings between 0-40 vol.% (10). The GPG model is a modified form of the Maxwell model and is based on the model of a hard

sphere (161). It has been validated for both liquid and gas permeation for AC contents up to 15 vol.% (152,162).

Maxwell $$\frac{P_{eff}}{P_c} = \frac{P_d + 2P_c - 2\varphi_d(P_c - P_d)}{P_d + 2P_c + \varphi_d(P_c - P_d)} \tag{7}$$

Bruggeman $$\frac{P_{eff}}{P_c} = \frac{1}{(1-\varphi_d)^3} \left(\frac{\frac{P_{eff}}{P_c} - \frac{P_d}{P_c}}{1 - \frac{P_d}{P_c}} \right)^3 \tag{8}$$

GPG

$$\frac{P_{eff}}{P_c} = 1 + 3\beta\varphi_d + K\varphi_d^2 \tag{9}$$

In these models, P_{eff} is the effective permeability, P_d and P_c are the permeability in the dispersed (AC) and continuous (matrix) phase, φ_d is the volume fraction of AC, and K is a correction factor defined in terms of β:

$$\beta = \frac{P_d - P_c}{P_d + 2P_c} \tag{9a}$$

$$K = a + b\varphi_d^{1.5} \tag{9b}$$

$$a = -0.002254 - 0.123112 \, \beta + 2.93656 \, \beta^2 + 1.690 \, \beta^3 \qquad \text{(9c)}$$

$$b = 0.0039298 - 0.803494 \, \beta - 2.16207 \, \beta^2 + 6.48296 \, \beta^3 + 5.27196 \, \beta^4 \qquad \text{(9d)}$$

In this case, β is bound by $-0.5 \leq \beta \leq 1$. For $\varphi_d \ll 1$, the GPG model simplifies to the Maxwell model (152).

Several more complex models have been developed for predicting behavior of MMMs. Although not extensively used to model AC-MMMs, many accurately predict the behavior of CMS-MMMs (8). Major differences between the simple models presented in Equations 7-9 and the more complex models is a consideration for particle shape, maximum particle loading achievable, presence of a permeable layer between particle and matrix, or some combination. These are factors are essential to consider for general models where different fillers can have vastly different properties (163).

The Maxwell-Wagner-Sillar model takes into account the particle shape, estimating it as an ellipsoid (152). This is determined by the variable, n, which is bound $0 < n < 1/3$ and $1/3 < n < 1$. The model reduces to simple parallel/series resistance based models when n is an extreme. Similarly, the Cussler model estimates the shape as a flake represented by the flake aspect ratio, α_f (152). This model may find particular accuracy with some CMS-MMM due to their potentially high aspect ratio.

Both the Lewis-Nielsen and Pal models include a shape factor, α, which can be used to fit experimental data, or taken as the inverse diameter when particles are modeled as tubes

(152). Each also considers a maximum packing volume fraction achievable in MMMs, φ_m. For particles estimated as a sphere, this value is 0.64, but can by any fraction dependent on the particle size distribution, shape, and aggregation tendency. When φ_m approaches 1, the Lewis-Nielsen model reduces to the Maxwell equation and the Pal model reduces to the Bruggeman equation.

The Felske model contains multiple parameters to account for a permeable layer between the particle and matrix (152). This type of filler is otherwise known as a core-shell. The particle is the core surrounded by some permeable shell. To account for permeability in this layer, the permeability of the species of interest in that interface layer, P_I, is required. To account for the thickness of the shell layer, a parameter δ is defined as the ratio of outer diameter shell to outer diameter of the core. This may find use in AC-MMMs where particles are grafted or interfacial polymerization is conducted at the particle/matrix interface.

Maxwell-Wagner-Sillar

$$\frac{P_{eff}}{P_c} = \frac{nP_d + (1-n)P_c - (1-n)\varphi_d(P_c - P_d)}{nP_d + (1-n)P_c + n\varphi_d(P_c - P_d)} \tag{10}$$

Lewis-Nielsen

$$\frac{P_{eff}}{P_c} = \frac{1 + 2\varphi_d(\alpha - 1)/(\alpha + 2)}{1 - \psi\varphi_d(\alpha - 1)/(\alpha + 2)} \tag{11}$$

$$\psi = 1 + (\frac{1 - \varphi_m}{\varphi_m^2}) \varphi_d \tag{11a}$$

Pal

$$\frac{P_{eff}}{P_c} \left(\frac{\alpha - 1}{\alpha - \left(\frac{P_{eff}}{P_c}\right)} \right) = \left(1 - \frac{\varphi_d}{\varphi_m}\right)^{-\varphi_m} \tag{12}$$

Cussler

$$\frac{P_{eff}}{P_c} = \cfrac{1}{1 - \varphi_d + \cfrac{1}{\cfrac{P_d}{\varphi_d P_c} + 4\cfrac{1 - \varphi_d}{\alpha_f^2 \varphi_d^2}}} \tag{13}$$

Felske

$$\frac{P_{eff}}{P_c} = \frac{2(1 - \varphi_d) + (1 + 2\varphi_d)\beta/\lambda}{(2 + \varphi_d) + (1 - \varphi_d)\beta/\lambda} \tag{14}$$

$$\beta = (2 + \delta^3)\frac{P_d}{P_c} - 2(1 - \delta^3)\frac{P_I}{P_c} \tag{14a}$$

$$\lambda = (1 + \delta^3) - (1 - \delta^3)\frac{P_d}{P_I} \tag{14b}$$

All models predict an increasing permeability for increasing AC loading when $P_d > P_c$. Considering AC is highly porous, this is a reasonable prediction and as such, an example of this situation is depicted in Figure 15.
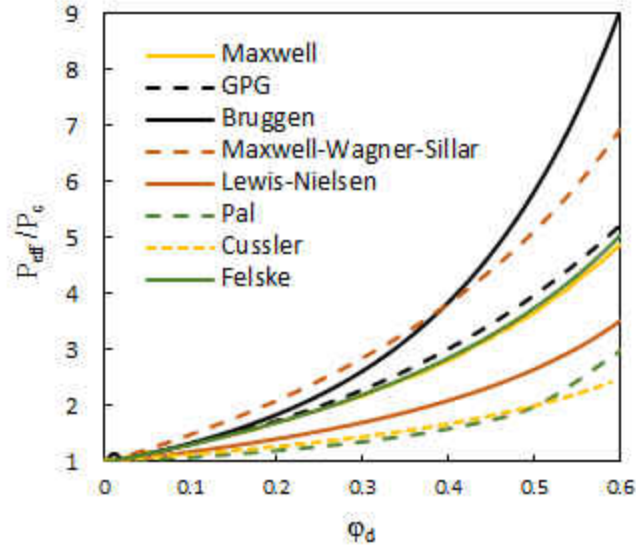
Figure 15: Comparative example of models with $P_c = 20$ and $P_d = 1000$, corresponding to $\beta = 0.94$. Other reasonable assumptions used are: $n = 0.2$, $\alpha = 5$, $\alpha_f = 10$, $\varphi_m = 0.5$, $P_I = 800$, $\delta = 1.01$.

When comparing experimental data to the models presented, three known variables are necessary, P_d, P_c, and φ_d. There are a number of methods to measure P_d and P_c, including constant pressure-variable volume apparatuses, or constant volume-variable pressure apparatuses. Similar techniques can be used to determine P_I for use in the Felske model. Time lag measurements can also be taken to determine the diffusivity coefficient. Using pure continuous phase adsorption measurements and Henry's law, the solubility coefficient can be calculated. Multiplying the two coefficients, the permeability can be calculated.

While the volume fraction of AC is defined in the formation of the casting solution, slight variances can occur between forming the casting solution and casting. For a better estimation of φ_d , Weigelt et al. (10) suggested using thermogravimetry by first finding the weight fraction of AC, w_{AC}, using,

$$w_{AC} = \frac{m_{MMM} - m_{matrix}}{m_{AC} - m_{matrix}}$$

(15)

64

where m_{MMM}, m_{matrix}, and m_{AC} are the final mass of the MMM, matrix, and AC after degradation under inert conditions at 1000°C. The volume fraction of AC is then calculated based on the density of each component ρ:

$$\varphi_d = \frac{1}{1 + \left(\frac{\rho_{AC}}{\rho_{matrix}}\right) * \left(\frac{1}{w_{AC}} - 1\right)} \tag{16}$$

8. Suggestions for Future Work

Although AC shows promise as a filler in MMMs, several fundamental studies are still required to fully realize their potential. Specifically, there is still not a fundamental understanding to how AC interaction with polymers can be probed before membrane formation. Classic methods for probing interaction in other cases involve comparing solubility parameters and analyzing functional groups. However, in the case of solid-liquid and solid-solid interactions involving AC, this becomes more complex, and determining solubility parameters becomes difficult. Therefore, fundamental studies are needed to expose the mechanism behind AC interactions with polymers, solvents, and other additives. This will involve the development of novel methods and perhaps the theoretical framework from colloid interactions in various media.

Another fundamental necessity that is thus far unclear is a relationship between AC properties and MMM performance. There is contradictory evidence between AC surface area, pore size, particle size and functionality on MMM performance. This lends to the conclusion there is ample interactions between each property that is not yet realized. Understanding this

would require studies with carefully controlled AC properties be pursued, which can be accomplished by investigating various biomass or polymer precursors, activating methods, and post treatments. This fundamental knowledge would provide some criteria and more insight into material selection of AC and polymer combinations.

In AC-MMM formation, still very little has been investigated relating phase inversion variables and MMM properties. Important variables include nonsolvent, additives, and temperature. Each is likely to cause a shift in the equilibrium between each phase in the casting solution. Binodal shifts in ternary phase diagrams can give insight into cross sectional structure and help guide experimentation, which has yet to be thoroughly examined. Detailed studies of dry phase inversion are also needed. It is not clear how various parameters can be manipulated to prevent unwanted sedimentation and surface ruptures. These studies are ultimately needed to determine if particle/filler interaction can be influenced by variables in the membrane formation process. Likewise, other membrane fabrication techniques should be investigated that may prove useful for some applications. For example, electrospinning of AC into fibrous membranes presents a plausible scenario (164), in which applications with surface pore size sensitivity may benefit.

In applications where adsorption is a major factor in separation performance, methods to sufficiently regenerate spent AC are still needed. This is a major issue because all active sites on the AC in MMMs may not be accessible by all fluids, which restricts the regenerating ability of some chemicals. Thus, a variety of regenerating methods needs to be investigated to give insight into how effective regenerating AC-MMMs are for various ions and molecules. This will allow realization of the extend of applications in which these membranes can be employed.

Furthermore, the gas separation potential of AC-MMMs should be further pursued. This will also involve fine control of particle size distribution, pore size distribution, and surface area in AC and CMS. In doing so, AC-MMMs can be tailored to specific gas separation applications by enabling different flow regimes in the AC such as Knudsen diffusion, surface diffusion, and molecular sieving. Each may have advantages for different gas mixtures. Various other applications of AC-MMMs should also be investigated. One example is direct contact membrane distillation, which is influenced by membrane porosity, free volume, and thermal properties. Other applications involve proton exchange. While there have been some efforts to use AC-MMMs in proton exchange, their full potential has not been realized. Lastly, predictive models that take into consideration size distribution, pore size distribution, and shape distribution should be pursued. Currently no models consider variations in filler particles, but will be highly beneficial to AC-MMM due to the inevitable variability between particles. In all, these studies would benefit AC-MMMs greatly, but also provide insight into the entire class of MMMs.

CHAPTER III: BIOCHAR AS A FILLER IN MIXED MATRIX MATERIALS: SYNTHESIS, CHARACTERIZATION, AND APPLICATIONS

Abstract

The use of mixed matrix materials (MMM) has become a major topic of research in recent years, due to unique properties achieved in these composites. In this work, biochar from sunflower seed hull (SSH) pyrolysis and biochar/polysulfone (PSF) MMMs were produced and characterized. The optimal pyrolysis temperature for biochar production was determined to be 500°C. The resulting biochar properties were an iodine number of 203 mg/g and pore volume of 0.595 mL/g. In MMM fabrication, the use 4% ethanol as nonsolvent in the wet phase inversion process increased the glass transition temperature by 8°C, indicating improved biochar/PSF interaction. The presence of biochar was shown to create pores in otherwise dense surfaces. The critical surface energy was also increased by the addition of biochar from 28.6 mN/m in pristine PSF to 35.7 mN/m in biochar/PSF MMMs. We identified and discussed several potential applications based on the determined properties.

1. Introduction

Mixed matrix materials (MMMs) are composites, often formed into thin films, consisting of a continuous phase (matrix) and a dispersed particle phase (filler). Over the past three decades, these materials have been investigated for various applications including membranes for separations [1-3], reinforced materials for structures [4,5], and as wound dressings [6] among others. By creating MMMs, properties of both the matrix and filler are

exploited, and oftentimes enhanced, resulting in superior properties than either the matrix or filler alone. Despite the diversity of available filler materials and abundance of studies into their properties, one particular filler remains mildly researched; namely, biochar from biomass pyrolysis. Biochar exhibits distinctive properties and possess key features rendering it worthwhile to study in MMMs.

The most important aspect of MMM development is material's constituent's selection. As a result, much research has been focused on fabrication and implementation of various matrix/filler combinations. The most common class of matrix materials are polymers, due to the number of polymers available, and the simple processability of polymers into MMMs. MMMs with glassy polymers [7], rubbery polymers [8], polymer blends [9], and copolymers [10,11] have all been investigated. Both inorganic and organic type fillers have been investigated. These include clay particles [12], metal organic frameworks [2], activated carbon [13], graphene [4,8], and metal oxides [14] to name a few.

Although any polymer and filler can be combined into MMMs, their compatibility is critical and deterministic for the overall composite properties and function. Poor compatibility can result in poor matrix/filler interactions, causing void formation, reduced thermal and mechanical performance [15], and undesired permeation properties [16]. Researchers have investigated several methods to prevent or correct poor polymer/filler compatibility [17], including functionalization of the matrix or filler [18], interfacial polymerization of monomers containing fillers [19], matching polarity of the matrix/filler [20], and using nano sized fillers [21].

Biochar as a filler material in MMMs functional composites has been minimally investigated as an effective element in MMMs. Biochar particles, a solid product of biomass

pyrolysis, are porous, with high specific surface areas, and can be easily processed into sizes ranging from nanometers to millimeters. Due to the nature of biomass and biomass degradation, biochars tend to possess surface functional groups that are dependent on the biomass precursor and pyrolysis conditions [22]. Biochar particles' functionality and porosity offer ample binding sites for the polymer matrix; thus, increasing the possibility of strong interfacial interactions [23]. Hence, owing to these key and significant features, in addition to the cost-effect production methods, biochars present an invaluable material to probe as a filler of MMM constructs.

Another critical aspect of MMM development and performance is the method of fabrication and processing selection. One of the most common fabrication techniques for creating MMM films involve phase inversion of a dissolved polymer/filler solution [24]. The wet phase inversion technique is performed by casting a dissolved polymer solution, then introducing it to a nonsolvent. Liquid-liquid demixing occurs instantly, resulting in precipitation of a thin polymeric film. [25]. The two key parameters of wet phase inversion are the quaternary components of polymer/filler/solvent/nonsolvent system and temperature. The dry phase inversion method utilizes solvent evaporation for film precipitation [26]. In this case, a cast solution is heated for enough time to allow all the solvent to evaporate. The rate of evaporation, and thus the environmental conditions, play an important role. Combinations of these two techniques have also been thoroughly investigated, known as dry/wet phase inversion. Each method results in films with unique surface and cross sectional morphologies. Other fabrication methods have been used for MMM development, but usually involve a phase inversion step as one step in the process. For example, spin coating utilizes a spinning wheel

to spread a film, rather than a casting blade, then phase inversion is used to precipitate the film [27].

Despite a thorough understanding of phase inversion processes, there has been minimal emphasis on how polymer/filler interaction is influenced by fabrication technique. The phase inversion process can be highly influential in the polymer/filler interaction due to the complex demixing that occurs upon precipitation. Biochar is highly adsorptive, so it is anticipated that when used as a filler, it has complex interactions between each of solvent, nonsolvent, and polymer due to the adsorption capacity of the biochar to each of these components.

In this work, we report on a study of filler-matrix interaction and influence of fabrication method on MMM films. In particular, we present characterization of MMM films consisting of a biochar filler embedded in a polysulfone (PSF) matrix. The biochar is synthesized from sunflower seed hulls (SSH), and the film is produced by the wet phase inversion method in ethanol solutions. We use this combination to investigate the viability of biochar as a filler in MMMs and to investigate the role of nonsolvent on the biochar/PSF interaction.

2. Materials and Methods

2.1. Materials

SSH were supplied by CHS Sunflower, Grandin, ND, USA. Polysulfone (35,000 Da PSF) and anhydrous dimethyl formamide (99.8% DMF) were purchased from Sigma Aldrich Co., USA. Compressed analytical-grade gases including argon (Ar 99.998%), nitrogen (N_2 99.998%) and air were purchased from Praxair Co., USA. PSF was dried in an oven at 105°C before use in an ambient atmosphere. DMF was used without further purification. Chemicals

used for iodine number determination (sodium thiosulfate (99%), iodine (>99.8%), potassium iodide (>99%, and potassium iodate (>98%)) were purchased from Sigma Aldrich Co., USA. Fuming hydrochloric acid was purchased from Fisher Scientific Co., USA. Butanol (99%) was used for pore volume estimation and was purchased from Fisher Scientific Co., USA. Polyethylene glycol (200 Da PEG) was used for surface energy calculations and was purchased from Sigma Aldrich Co., USA.

2.2. Biochar Synthesis via Slow Pyrolysis Reaction

Between 50 and 70g of SSH were loaded into a Thermolyne 21100 tube furnace reactor with a heating rate controller and temperature indicator shown in Figure 16. A stainless steel tube reactor with flanges on both ends was used as the reaction vessel. Argon (Ar) was used as the inert gas to displace oxygen at a rate of 2 mL/min. The reactor was purged with Ar for at least five minutes before heating. The reactor was set to heat at a rate of 15°C/min to various temperatures then allowed to slowly cool to room temperature under continuous Ar flow. Produced oils and tar were condensed in a water bath upon exiting the reactor, and volatiles were allowed to vent. Once cooled, the biochar was collected from the furnace and washed several times with distilled water, then dried in an oven at 105°C for several hours.
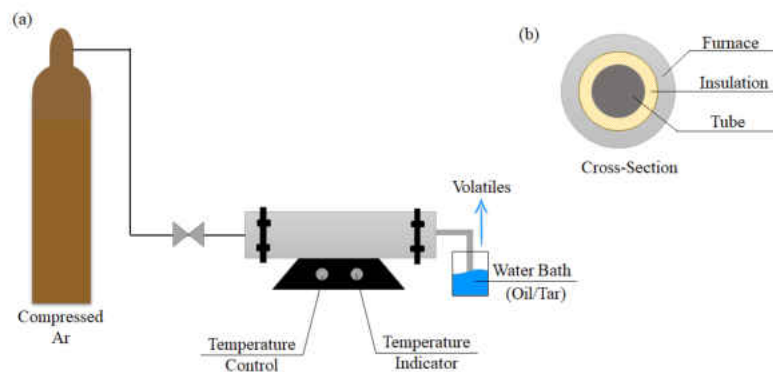
Figure 16: (a) Pyrolysis reactor set-up schematic and (b) cross-sectional view of furnace.

Once dried, the weight of biochar was recorded and the yield was calculated according to Equation 1:

$$Yield\ \% = \frac{Biochar\ Weight}{Initial\ Sample\ Weight} * 100\%$$ (1)

The biochar was then ground to a fine powder and sieved with an ASTM #270 mesh (53 microns) for one hour using a vibrating shaker.

2.3. MMM Film Fabrication

PSF was dissolved in DMF for an overall composition of 20% by mass of polymer. It is worth noting, DMF was chosen based on the solubility of biochar in DMF shown in Appendix A. While the solubility in the polymer phase is highly important, the solubility in the solvent was considered here for optimal results. The solution was stirred for at least 12 hours, or until completely dissolved, at room temperature with a mixing speed of 60 rpm. Biochar was then added at 1% by mass relative to the polymer phase, then mixed for at least 6 hours at a rate of 60 rpm. The solution was cast using a casting knife, then precipitated at room temperature in a nonsolvent of distilled water or ethanol solutions. The films were rinsed thoroughly with distilled water and dried at room temperature before analysis.

73

2.4. Biochar Characterization

2.4.1. Ultimate and Proximate Analysis

Ultimate analysis (CHN) was performed on raw SSH and biochar by Atlantic Microlab Inc., USA. Proximate analysis was performed using a thermogravimetric analyzer with differential scanning calorimetry (TGA/DSC) with a model SDT Q-600 analyzer. Samples were heated at a rate of 15°C/min in N2 or air from room temperature to 900°C.

2.4.2. Surface Area and Pore Volume

The biochar surface area was measured by means of iodine adsorption number according to ASTM standard 4607-94 [28]. In short, an iodine solution was put in contact with biochar. The residual was filtered and titrated with sodium thiosulfate to the endpoint. The iodine number is defined as the amount of iodine adsorbed per gram of biochar at a residual concentration of 0.02 N. The total pore volume was estimated based on thermogravimetric methods developed by Pan et. al., (1996) [29] and Mercuri et. al. (2006) [30]. Biochars were mixed with butanol, and the butanol desorption rate was quantified from changes in TGA/DTG curves. The pore volume was calculated based on empirical correlations listed in the Appendix B.

2.4.3. Scanning Electron Microscopy (SEM)

The particle size distribution was measured by analyzing SEM images with the open source software Image J [31]. Images were taken using a Hitachi SU8010 field emission scanning electron microscope. The number frequency average was taken based on the largest diameter of each particle. Biochar pores and surface morphology were also investigated by SEM analysis.

2.4.4. Functional Groups

Functional groups were analyzed using a ThermoNicolet NEXUS 460 FTIR equipped with a ZnSe crystal and DTGS detector. The spectra were tested in attenuated total reflection mode.

2.5. MMM Film Characterization

2.5.1. Differential Scanning Calorimetry (DSC)

A PerkinElmer DSC was used to measure glass transition temperature (T_g) of MMMs. About 5mg of samples were tested in aluminum pans. The method consisted of three cycles of heating from 0 to 200°C at a rate of 20°C min^{-1}, and were held isothermal at 0 and 200°C for two minutes to allow the sample to equilibrate.

2.5.2. Thermogravimetric Analysis (TGA)

TGA was performed on MMMs using the equipment described in section 2.4.1. About 10mg of film were analyzed. The degradation temperature (T_d) was recorded based on the maximum of the differential thermogravimetric (DTG) curve.

2.5.3. Scanning Electron Microscopy (SEM)

MMM morphology was investigated using a Hitachi SU8010 field emission scanning electron microscope. MMMs were fractured with liquid nitrogen to expose the cross section, then sputter coated for 30 seconds with carbon.

2.5.4. Contact Angle and Surface Energy

The contact angle of MMM films was measured by a sessile drop method described by Costa et al. (2018) [32]. In short, an image was taken of a 20 µL drop from the top view. The

diameter was measured, and the contact angle was calculated assuming a spherical cap geometry. Further detail on this method is described in the Appendix C. The critical surface energy was calculated based on the contact angle of PEG solutions according to the Zisman method [33,34], as described in more detail in section 3.2.

3. Results and Analysis

3.1. Biochar Fabrication and Analysis

In order to determine a suitable pyrolysis temperature of SSH, the pyrolysis reaction was investigated by TGA, as it has been shown before that the optimal reaction temperature can be predicted in this fashion [35]. From the DTG curve in Figure 17a, it is apparent that weight loss occurs at two temperature ranges. The first peak near 100°C is attributed to moisture loss whereas the second peak occurs near 350°C and is a result of cellulose, hemicellulose, and lignin degradation. The degradation rate levels off at 450°C. Thus at 500°C, the major degradation is complete. To complement this, yield was taken after pyrolysis at several temperatures and is shown in Figure 17(b). As expected, the yield decreases as temperature increases until about 500°C where there is little change. It is worth noting that the theoretical yield of biochar based on the TGA curve does not always match the actual yield, primarily due to the residual uncharred biomass. Based on these two results, 500°C was chosen as the optimal pyrolysis temperature. In this case, the optimum temperature results in low yield but desirable physicochemical properties.
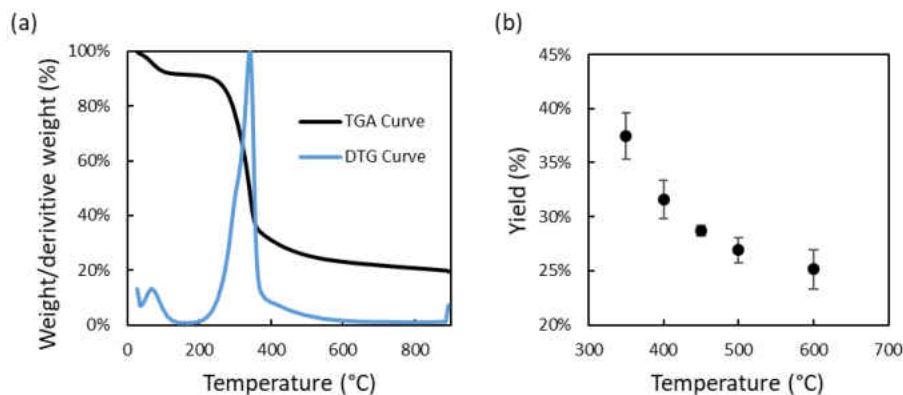
Figure 17: (a) TGA and DTG curves of the raw SSH and (b) biochar yield as a function of temperature after pyrolysis.

From the ultimate analysis results shown in Table 6, it is clear that biochar is richer in carbon and nitrogen compared to the raw SSH. Likewise, the presence of oxygen and hydrogen decreased after pyrolysis. This is to be expected; as pyrolysis occurs, oxygenated functional groups easily break apart and leave behind a graphite like structure, which is also concluded by the fixed carbon content of each species. The pore volume and iodine number demonstrate the formation of pores within the biochar, creating additional surface area for gas-solid and liquid-solid adsorption.

Table 6: Ultimate and proximate analysis of raw SSH and biochar produced at 500°C, and physical properties of biochar. All percentages are by weight.

Property	Raw SSH	Biochar
C (%)	48.24	65.93
H (%)	5.84	3.54
N (%)	0.30	2.00
O*(%)	41.16	17.25
Moisture (%)	3.45	2.60
Volatiles (%)	81.90	36.06
Ash (%)	4.46	11.28
Fixed Carbon* (%)	10.19	50.06
Iodine Number (mg/g)	-	203
Pore Volume (mL/g)	-	0.595

*denotes calculation by difference.

After sieving the biochar, the number average diameter was taken and organized into bin sizes of 2.5 microns. As shown in the histogram in Figure 18a, there was a higher percentage of smaller particles. Had aggregates been considered, the number average would have been highly skewed as a significant number of aggregates were observed as seen in Figure 18b. However, some particles larger than the mesh size (55 microns) were measured. The appearance of particles larger than the mesh size can be explained by their variation in geometry: larger particles could pass if oriented on their smaller axis.
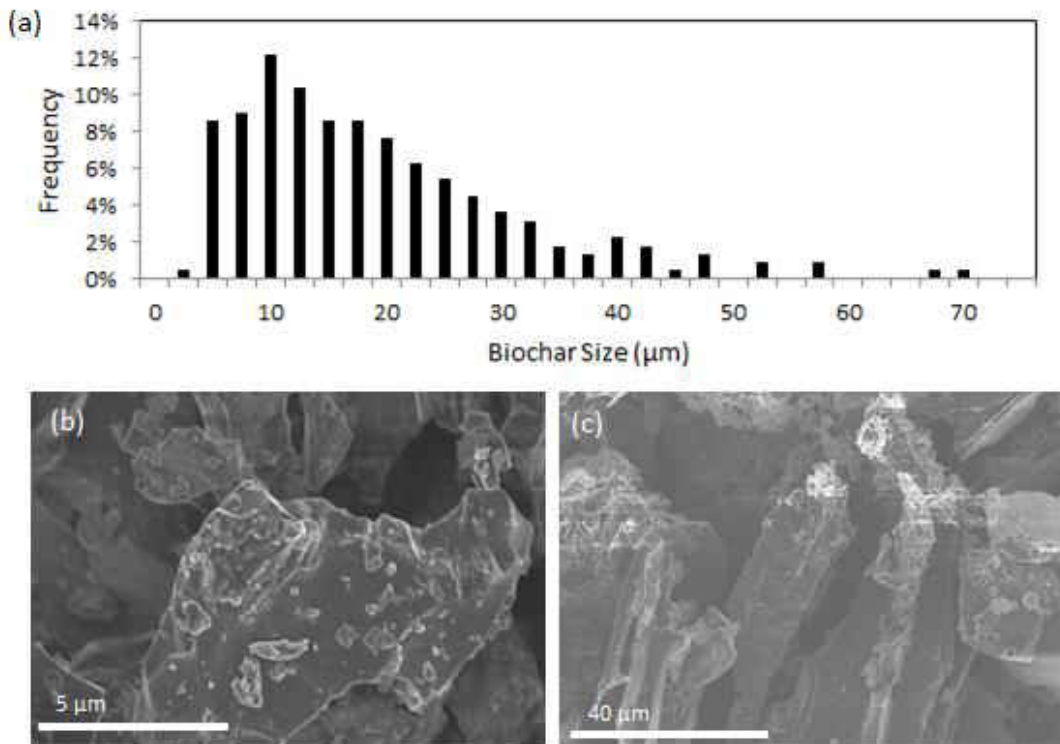
Figure 18: (a) size distribution of biochar ignoring aggregates less than 2.5 microns. (b) SEM image depicting aggregate formation, (c) irregular shaped particles, and pore formation.

FTIR spectra of the biochar is shown in Figure 19. The baseline shift seen after 2000 cm^{-1} is apparent and is common for carbonaceous materials due to strong absorption bands in that region. This causes a refractive index response very close to that of the ZnSe crystal, resulting in a noticeable shift. Regardless of this, the peaks are readily visible. Their position

and corresponding functional groups are summarized in Table 7. The spectra indicate the presence of oxygenated and nitrogenized functional groups with alkane, alkene, and alkyne linkages supported in aromatic structures.
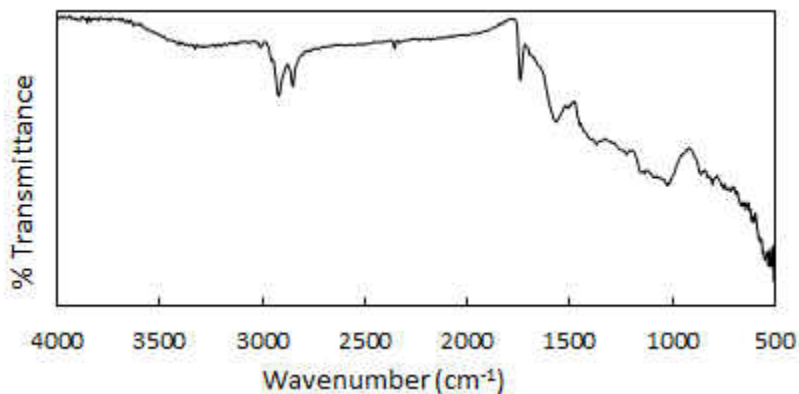
Figure 19: FTIR spectra of biochar created from pyrolysis of SSH at 500°C.

Table 7: Summary of FTIR spectra of biochar.

Peak Location (cm^{-1})	Functional Group	Molecular Motion
3300	Alcohols	-OH stretch
2900-2850	Alkane	CH$_3$ stretch
2350	Alkyne or Nitrile	C≡C stretch, C≡N stretch
1740	Aldehyde or Ester	C=O stretch
1650	Amide or Carboxylate	CO$_2$ stretch
1370	Aldehyde	C-H bend
1220	Ester	C-C-O stretch
1130	Ester	O-C-C stretch
<1000	Aromatic	C=C, NH$_2$ wag, C-C stretch, C-O bend, N-O bend, N-H bend, O-H bend, C-H stretch

3.2. MMM Fabrication and Analysis

The wet phase inversion method can be described by a solvent/nonsolvent/polymer ternary phase diagram as shown in Figure 20. The binodal line represents the region in which liquid-liquid demixing begins and phase separation occurs. Experimentally, the binodal line is determined by titration with nonsolvent to the cloud point. It is apparent that there is a difference in binodal placement if pure water or pure ethanol are used as the nonsolvent. Various concentrations of ethanol in water are expected to lie within these two curves, so they were not recorded.
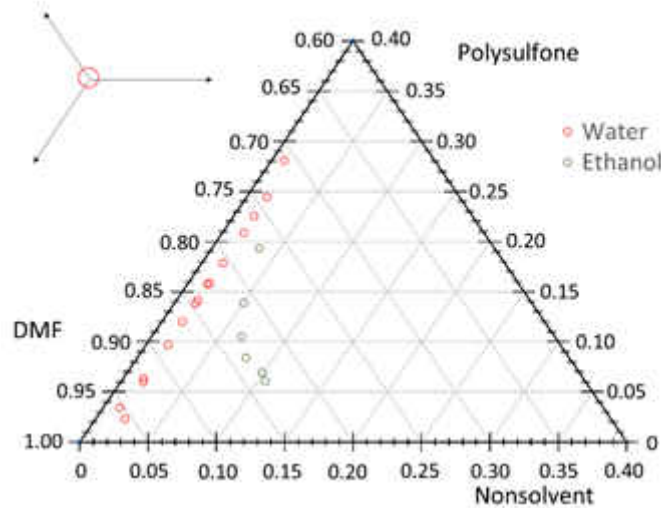
Figure 20: Ternary phase diagram with experimentally determined binodal lines using pure water and pure ethanol as nonsolvent in DMF/PSF/Nonsolvent system. All fractions are by weight and the key in the top left demonstrates the relationship between each point and its corresponding grid lines

MMM films loaded with 1% (relative to the polymer phase) of biochar were precipitated in various ethanol solutions containing between 0 and 20 vol.% ethanol. The T_g of each was measured since it is understood that the polymer/filler interaction in MMMs can be examined by measuring T_g of the composite [36, 37]. The T_g was taken as the inflection point from DSC thermograms as seen in Figure 21a. The extracted values shown in Figure 21b demonstrate

there is a linear trend until about 4 vol.% ethanol, then flattens off. This analysis revealed some interesting features of the biochar/PSF MMM.
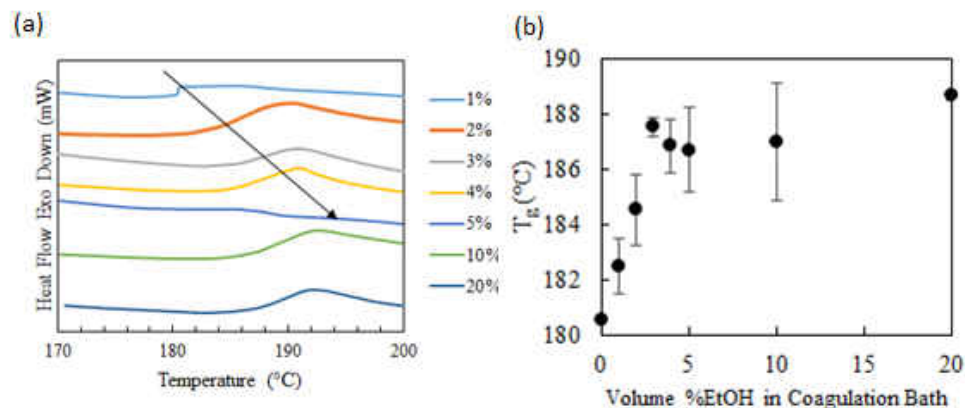
Figure 21: (a) DSC thermograms and (b) extracted Tg data as a function of vol.% ethanol in coagulation bath at 95% confidence.

FTIR spectra of each film were taken to rule out the possibility of chemical reactions caused by ethanol, and to investigate possible migration of biochar to either surface of the film. Both top and bottom of the films were observed, but due to exact matches between sides, only the top is shown. The spectra shown in Figure 22 reveal that no chemical reactions took place during the phase inversion process, as all peaks are consistent between samples and match the spectra of pure PSF reported elsewhere [38]. The most important peaks and corresponding wavenumbers that identify PSF are aryl ethers (1270-1230 cm^{-1}), aryl sulfones (1170-1135 cm^{-1}), and methyl groups (2970-2950 cm^{-1}).
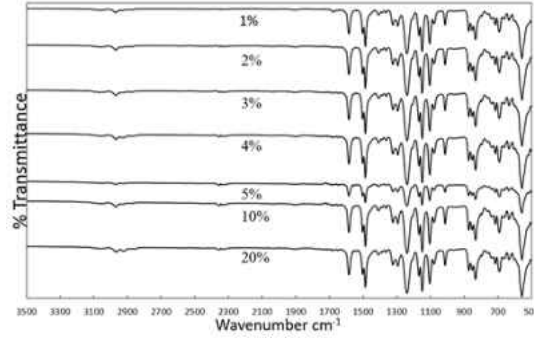
Figure 22: FTOR spectra of MMMs made with 1-20 vol.% ethanol in the coagulation bath.

The cross section and surface morphology were investigated using SEM. No morphological differences were apparent between films made with and without ethanol in the coagulation bath as seen in Figures 23a and 23b. The surface appears dense and the cross section is asymmetric with a thin top skin and spongy support structure. While the presence of ethanol did not appear to have an effect on morphology, the influence of biochar loading significantly influenced the surface.
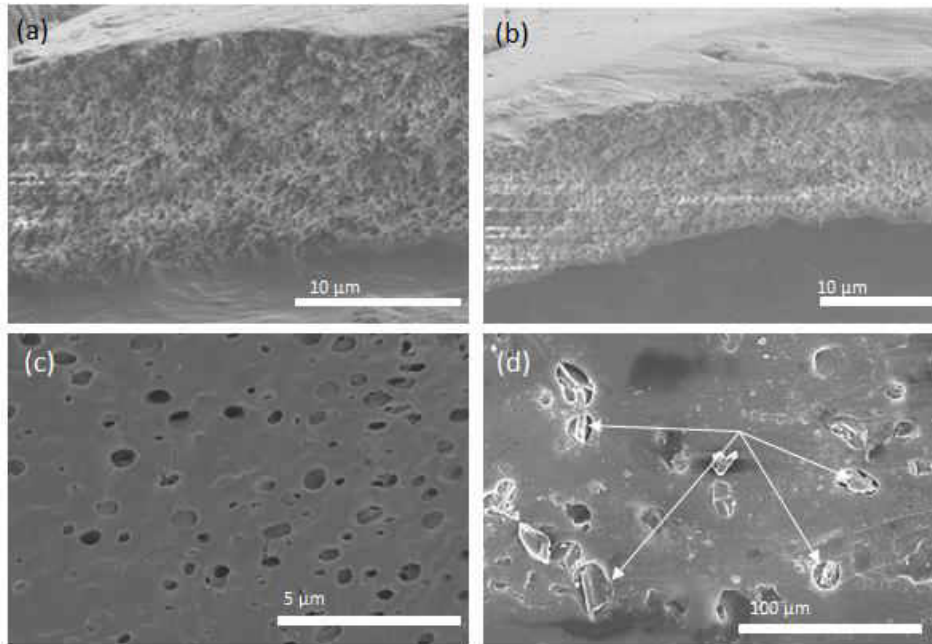
Figure 23: Cross sectional view of films made with (a) 0% and (b) 4% ethanol. Surface view showing (c) pore formation with 10% loading and (d) pore blockage at 40% biochar loading.

To demonstrate this, MMMs were loaded with 10 and 40 wt.% biochar relative to the polymer phase. The 10% loaded films showed surface pore formation on the order of 1 micron, shown in Figure 23c. At 40%, the pores appear larger, on the order of 10 microns. However, pore blockage was apparent as depicted in Figure 23d.

The surface energy of MMMs is another important parameter that allows for the prediction of properties such as permeability and adsorption of fluids. One technique to measure this is the Zisman method, which is an empirical method that allows for the evaluation of the critical surface energy (γ_c). The procedure is commonly employed for quick estimations of solid surface energy. The procedure and derivation have been discussed elsewhere in detail [39, 40]. In short, the known liquid surface energy of several different liquids, γ_l, is plotted verses $\cos(\theta)$, where θ is the contact angle between the solid and liquid drop. The linear line is extrapolated to the point where $\cos(\theta) = 1$. The value of surface energy at this point is γ_c.

Table 8: Measured contact angle on each surface, and liquid surface energy values used for analysis. The contact angles reported are the average of at least two measurements at a 95% confidence level.

Liquid	γ_l (mN/m)	Contact angle (°)	
		Pure PSF	1% Loaded Biochar in 4% Ethanol
Distilled Water	72.80 [49]	70.01 ± 2.0	72.56 ± 2.0
15% PEG-200	60.79 [49]	64.14 ± 2.1	53.59 ± 0.5
PEG-200	43.50 [50]	37.67 ± 1.5	33.08 ± 0.5

PSF is readily dissolved in many common liquids with known γ_l. This tremendously reduces the number of liquids available for analysis because drops will quickly dissolve films and not form a drop upon contact. In this case, three different liquids were examined: distilled

water, PEG-200, and a 15 vol.% PEG-200 in distilled water. The contact angle measurements and γ_l values are displayed in Table 8.

All contact angles are the average of at least three measurements. The contact angles of each liquid on the 1% loaded biochar films formed in 4 vol.% ethanol were compared to films prepared without biochar to gain a better understanding of the influence biochar has as the filler material. All values were recorded in Table 8 and were used to construct a Zisman plot (Figure 10).
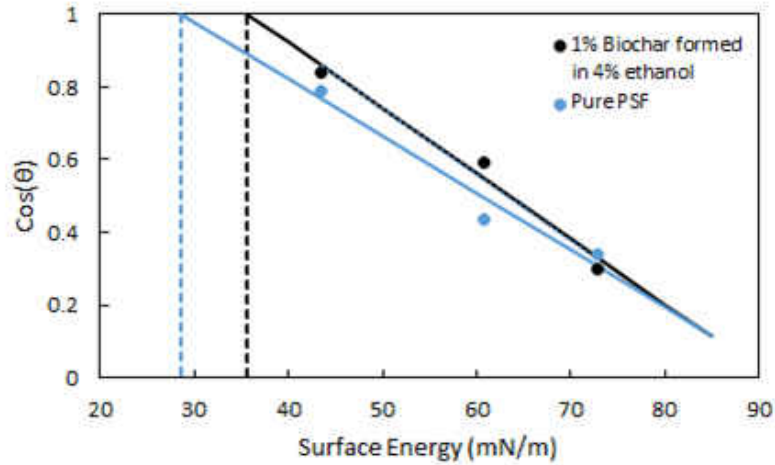
Figure 24: Zisman plot for each film showing extrapolated values for the 1% biochar (γ_c=35.7 mN/m, R2 = 0.9761) and pure PSF (γ_c=28.6 mN/m, R2 = 0.9519).

4. Discussion

In fabricating biochar from SSH pyrolysis, yield, surface area (iodine number), pore volume, and functional groups are key parameters that are influenced by pyrolysis temperature. It was shown that the yield decreases with increasing pyrolysis temperature at a rate of between 5%-10% per 100°C. Furthermore, it is well accepted that there exists a tradeoff between the yield and some of the physical properties. This is important to realize because at moderate

temperatures, a low yield typically indicates the point where surface area and pore volume are highest. This point is distinguishable in Figure 17. Thus if pyrolysis is performed at lower temperatures, the iodine number and pore volume will likely be lower, despite the higher yield. The same is true at higher temperatures. In this case, pores collapse, resulting in lower surface area and pore volume. This optimal pyrolysis phenomenon is commonly encountered [22].

There are several implications to potential applications based on the biochar characteristics. Firstly, the iodine number of 203 mg/g is reasonable compared to other biomasses [41]. Depending on the desired application, this iodine number could be sufficient. For example, if used as a conducting material, the surface area may not influence conductive properties. If used for separations, higher adsorption capacity may prove beneficial, so further treatment of the biochar may be necessary. The opposite is applicable for antimicrobial film applications where much of the antimicrobial properties are a result of microbe repulsion. Higher surface area allows more space for microbes to collect, thus reducing the antimicrobial properties [42].

The particle size and size distribution are expected to have some significant effects. It was shown in Figure 18 that the average biochar particle size obtained was 18.1 ± 4.0 microns (at 95% confidence) with a median of 15.7 microns. Because the particles are relatively large, the MMM thickness is limited to the size of the largest particles. If thinner films are formed, there is a higher chance of surface ruptures. Considering small particles tend to perform better in MMMs, the presented size distribution lends itself to a mixture of interactions in the MMM. Some of which favor strong interactions, some favor weaker interactions. Since the size distribution is skewed toward smaller particles, those interactions may be dominant.

The functional groups seen in the biochar are more so important to polymer/filler interaction than the size distribution. The FTIR spectra in Figure 19 indicate the presence of oxygenated and nitrogenized functional groups with alkane, alkene, and alkyne linkages supported in aromatic structures. The positive ends of the polar oxygenated/nitrogenized functional groups can produce dipole interactions between them and the sulfone group in PSF. However, the coupling of biochar size, size distribution, pore volume, surface area, and functional groups actually showed poor interaction between the biochar and PSF when water was used as the nonsolvent. This is indicated by a T_g of 181°C ±1.5°at 95% confidence, which is lower than the 185°C T_g of pure PSF. Thus, the nonsolvent choice was shown to be significant. A shift in the ternary binodal line indicated that when using ethanol as the nonsolvent, the demixing process speeds up, resulting in faster demixing. Physically, this is significant because the solvent will quickly diffuse from the polymer rich region to the nonsolvent, causing a reduction in the hydrated layer surrounding the biochar [43]. This likely results in better adhesion between the biochar and PSF. This is supported by the increase in T_g with increasing amounts of ethanol in the nonsolvent described in Figure 21. The T_g at 4 vol.% ethanol of about 188°C ±1° at 95% confidence, is indicative of this improved interaction. Considering this, it is anticipated that other thermo-mechanical properties are also improved. The use of 4% ethanol in the coagulation bath offers a simple method to improve the interaction between biochar and PSF. It can possibly improve the interaction between other combinations of polymer/filler and should be investigated.

Moreover, the absence of characteristic FTIR peaks of the biochar on the top and bottom surface of the MMMs indicated that there was no migration to either side of the film, and the biochar remained within the cross section. Considering the migration of fillers to the

surface of MMMs have been observed before [44], the concentration of biochar at the top surface may have been too dilute to measure its characteristic peaks by FTIR.

Another important thermal property is the degradation temperature (T_d), defined here as the temperature where the DTG curve is maximum. The T_d, regardless of ethanol concentration in the coagulation bath was near 543 ±7°C at 95% confidence. However, this is lower than what is typically reported for PSF [38]. This is likely a result of thermal degradation of the biochar, T_d of about 300°C, occurring before that of PSF. This has two pronoun effects on the overall T_d. Firstly, the degradation of biochar leaves behind void spaces, resulting in a more unstable matrix. Secondly, the decrease in mass of the sample at lower temperatures causes a faster response in T_d, which is a well-known occurrence in TGA [45]. Therefore, the thermal stability of the biochar ultimately limits that of the MMM, rather than acting as a thermal stabilizer. The implications are the combination of biochar/PSF MMMs cannot be used in high temperature applications that exceed 300°C, else the biochar would thermally degrade leaving behind an unstable MMM. Many applications involving films are often performed at temperatures much lower than 300°C, so this may not restrict the use of these MMMs.

The cross sectional and top surface morphology of the MMMs shown in Figure 23 also give insight into the potential use. MMMs with dilute biochar showed dense top surfaces with spongy cross sections with a thin dense layer. This lends itself for use in separations where the dense surface of the PSF acts as the selective barrier. Being thin, this layer is expected to exhibit high flux to gases when subject to high pressures. When higher concentrations of biochar were added to the MMMs, surface pores formed. This along with adding pore forming agents could create suitable materials for liquid phase separation applications where surface pores are necessary. Furthermore, very high concentrations of biochar tend to cause surface

defects such as ruptures and pore blockage. These defects are undesired and result in materials that are unusable for most applications: poor mechanical stability, poor thermal stability, inhomogeneity in the surface. Clearly there is a limit in biochar loading, much like other filler materials.

Lastly, it was apparent the critical surface energy of the biochar loaded film (35.7 mN/m, regardless of ethanol concentration in nonsolvent) was higher than that of the pure PSF (28.6 mN/m). This analysis is depicted in Figure 24. While both surfaces are considered "low energy", this indicated the surface of the biochar loaded film has a higher affinity to adsorb liquids. In turn, this leads to higher degrees of wetting for a larger array of liquids. Thus the biochar loaded MMMs are more versatile in regards to liquid phase separation applications where complete surface wetting is attributed to better separation performance.

Biochar/PSF MMMs can also be worthwhile to study in electronic applications where a moderate dielectric constant and thermal stability are required. Pure PSF has a dielectric constant near 3.1, depending on molecular weight. Considering biochar is electrically conductive [46], much like other carbonaceous materials, the dielectric constant of these MMMs is likely higher. The films would also have a tunable dielectric constant based on the biochar loading thus, would be ideal and versatile for the dielectric end of a monopole antenna. This, coupled with the wetting ability of many different liquids on the surface, can lead to a variety of liquid sensing capabilities. However, care must be taken as inhomogeneous loading could lead to anisotropic electrical properties [47]. Under low pressure conditions, these MMM characteristics also find useful traits in film packaging applications. Biochar tends to be antimicrobial, resulting in antimicrobial MMMs [48]. This, coupled with a dense top layer,

limits penetration of unwanted moisture or bacteria when subject to a range of temperatures at normal pressures, which is an ideal case for film packaging.

5. Conclusion

We have shown that biochar made from SSH pyrolysis at 500°C is a feasible filler in a PSF matrix made by wet phase inversion. This work addressed and offered a solution to one of the most prioritized problems with MMMs, poor polymer/filler interaction. By using a solution of 4 vol.% ethanol in distilled water as the nonsolvent, the T_g was shown to increase, indicating better biochar/PSF interaction. This reaches far beyond the biochar/PSF combination, as it can potentially improve the interaction between other filler/matrix combinations. The presence of ethanol in the coagulation bath did not influence surface or cross sectional morphology or surface energy. However, the presence of biochar in the PSF did influence the surface morphology and surface energy compared to pristine PSF. Insight into potential applications were discussed. In future works, the further application of biochar/PSF MMMs can be investigated as they present promising characteristics.

CHAPTER IV: FACTORIAL STUDY ON ACTIVATED CARBON MIXED MATRIX MEMBRANE FORMATION FOR ANILINE BLUE FILTRATION

Abstract

Mixed matrix membranes (MMMs) have become an effective membrane material for various applications. Activated carbon (AC)-polysulfone (PSF) MMMs are suitable contender for dye filtration due to size exclusion by PSF surface and adsorption by AC. In this work, AC from sunflower hull pyrolysis in a PSF matrix was investigated. A replicated 2^3 full factorial statistical design was used to investigate the effects of activated carbon (AC), polyethylene glycol (PEG), and solvent type, used during MMM formation, on contact angle, agglomeration frequency, and aniline blue filtration. We presented a novel method of studying agglomeration tendencies in MMMs. Results of the factorial analysis revealed information about each factor. Specifically, solvent type and PEG/solvent interactions had significant effects on water contact angle. Agglomeration frequency was influenced by AC loading, PEG loading, and interactions between AC/PEG loading and AC/solvent. Flux was significantly affected by PEG loading and also an AC/solvent interaction. Lastly, aniline blue rejection was influenced by AC loading and a PEG/AC interaction. The adsorption kinetics of aniline blue on the AC was also investigated, and an optimal membrane was selected based on the factorial analysis. The results demonstrated useful feature that are easily extended to other MMMs for other organic macromolecular separations

1. Introduction

A large percentage of dyes used in the textile industry are disposed of as waste water effluent and can be recycled back into the local water supply. High concentrations of dye in water are colorful, and colored water negatively impacts the public perception of water quality [1]. Also, dyes cause damage to aquatic species by reducing oxygen concentrations and preventing light penetration into water bodies [2]. Thus, the removal of dyes from wastewater has become an important environmental concern. Furthermore, dyes are large organic molecules, similar in many regards to other macromolecules. From a separation standpoint, the rejection of dyes is often used as a model pollutant, and is easily expanded to include other macromolecules [3]. While many studies have experimented with the removal of reactive dyes, less attention has been given to acid dyes such as aniline blue. Aniline blue is used frequently in fluorescence microscopy, assay development, and plays various roles in textile dying [4]. Many of its toxicological properties are, as of yet, unknown, but it is evident there are some hazardous potentials upon exposure [5].

Of the various methods available for dye removal, adsorption and membrane separation are two prominent contenders [6,7]. Adsorption is effective for removing dye from water, but is limited in the sense that it is an equilibrium process, meaning, it would require frequent regeneration. Membrane separations, on the other hand, are a rate driven process. Various exclusion mechanisms are possible, but in the context of dye removal, size exclusion is the dominant mechanism. For these reasons, a class of membrane materials called, mixed matrix membranes (MMMs) are suitable contenders for this task. This composite membrane material contains a continuous polymer phase (matrix) with a dispersed particle filler. In using an

adsorbent filler, both size exclusion by the membrane surface, and adsorption by the filler within the membrane are possible [8].

MMMs are created by dissolving a polymer in an appropriate solvent, then mixing in particles and other pore forming agents or additives to form a dope. The dope solution is cast then phase inversion takes place. The most common phase inversion technique is nonsolvent induced (wet phase inversion). In this case, the solution is submerged in a nonsolvent then liquid-liquid demixing occurs rapidly and the membrane precipitates. It is well understood the thermodynamics and kinetics of this demixing process, and thus the choice of solvent, nonsolvent, and additives, play an important role in membrane formation [9,10]. Additives that are soluble in the nonsolvent not only influence the thermodynamic and kinetic properties of the phase inversion process, they also exit the membrane upon phase inversion. This leaves behind a porous surface suitable for dye filtration. Filler particles remain in the membrane post inversion. Interestingly, the addition of a particle phase also influences the thermodynamics and kinetics of the process [11]. Unique membrane morphologies and surface properties such as pores and wettability are highly influenced by the components of wet phase inversion [12]. Although MMMs composed of a variety of polymer/filler combinations have found success in many applications [13-15], they are still limited by various factors including, agglomeration defects caused by poor particle/polymer interactions, particle ruptures, and pore blockage [16-19]. All of which lead to undesired performance.

In order to understand how the choice of dope solution components effect some of these parameters and their relation to aniline removal from water, we utilized a replicated 2^3 full factorial randomized design. The MMM under study contains activated carbon (AC) dispersed in a polysulfone (PSF) matrix. AC is a well-established adsorbent for dye removal [20]. PSF

is a well-studied polymer that is easily cast by wet phase inversion [21] and is influenced by pore forming agents [22]. Two continuous factors chosen were concentration of polyethylene glycol (PEG) and concentration of AC in the dope solution. One categorical factor was the choice of solvent. The four responses were water contact angle, particle agglomerations, flux, and dye rejection.

2. Materials and Methods

2.1. Materials

Sunflower hulls used for AC production was obtained from CHS Sunflower Grandin, ND. Sodium hydroxide (50%) was used as the chemical activating agent PSF (35,000 Da), was used as the continuous matrix, dimethyl formamide (DMF 99.8%), and n-methyl-2-pyrrolidone (NMP 99%) were used as solvent. PEG (200 Da) was used as the pore forming agent. Aniline blue (799.80 g/mol) was the dye investigated. 50% sodium hydroxide was used for AC synthesis. All components were purchased from Sigma. Distilled water was used as the nonsolvent in the phase inversion process and as the dye solvent.

2.2. AC Production by Sunflower Hull Pyrolysis

About 60g of sunflower hulls were pyrolyzed into biochar in a Thermolyne 21100 tube furnace displaced by argon. The heating rate was set to 15°C/min, and the temperature was maintained at 500°C for 20 minutes then allowed to slowly cool to room temperature. The biochar was rinsed thoroughly with distilled water, dried, ground, and sieved with a No. 325 (55μm) tray. 5g of biochar was then impregnated with sodium hydroxide at a ratio of 2:1 (dry sodium hydroxide:biochar) by mass. The impregnated biochar was then activated by heating at a rate of 15°C/min to 700°C, maintained for 20 min, then allowed to slowly cool to room

temperature. The AC was washed with, 0.1M HCl, then with distilled water to remove residual activating agent. The resulting properties are shown in table 9.

Table 9: Properties of AC produced from sunflower hull pyrolysis and chemical activation of biochar impregnated with NaOH at a ratio of 2 NaOH : 1 biochar by mass, at 700°C.

Property	Value
Average diameter	18.1 μm
Diameter standard deviation	15.7 μm
Maximum particle diameter	55 μm
Iodine number	452 mg/g
Pore volume	0.595 mL/g
Moisture	3.45 %
Volatiles	36.06 %
Ash	11.28 %
Fixed carbon	50.06 %

One of the main advantages to using a biomass based activated carbon is the abundance of functional groups present in its structure [23,24]. The FTIR spectra for the AC made in this study was taken using a Thermo Scientific Nicolet FTIR in attenuated total reflectance mode with a ZnSe crystal. The spectra is shown in figure 25. It is evident the AC is aromatic with an abundance of oxygenated functional groups.
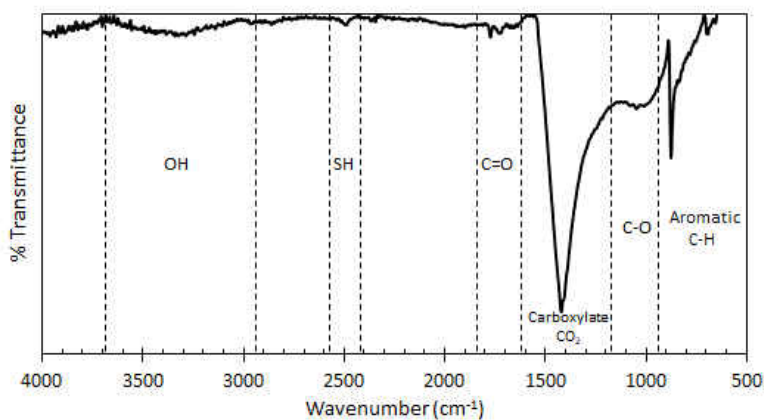
Figure 25: FTIR spectra of AC produced by NaOH activation of sunflower hull biochar.

2.3. Membrane Casting

A constant 20 wt.% polymer in solvent solution was used throughout each experiment. PEG and AC concentrations were then added relative to the polymer, as a percent weight according to the experimental design parameters. AC-MMM dope solutions were mixed for at least 24 hours with a magnetic stirrer at 60 rpm. The solutions were then spread on a Duran® glass plate, and cast with a casting blade. The membranes were then precipitated in distilled water, thoroughly rinsed, then submerged in distilled water for at least 12 hours to ensure complete solvent removal. They were allowed to dry in air at ambient conditions overnight before testing. The average membrane thickness was 70 +/- 3 μm.

2.4. Contact Angle Measurements

The contact angle of each membrane was measured based on the methodology presented by Costa et al. [25]. In short, a 20 μL drop of colored water was placed on the surface of the membrane. An image was taken of the top view with a resolution of 255 pixels/mm. The diameter of the drop was measured using the open source software ImageJ [26]. The contact angle was then calculated based on a spherical cap geometry. Additional details for this method are described in Appendix C. At least two measurements were taken per membrane and the average value was used.

2.5. Agglomeration Measurements

In order to study agglomeration trends, an imaging method was developed. A high resolution optical microscope with a bright front light was used to image the top surface of the membranes. AC within the membranes was clearly visible as black dots scattered throughout. The images were processed by ImageJ into 8-bit, black a white images, then the built in particle

analyzer was used to locate and count particles that were greater than 55 µm. The largest single

particle size after sieving was 55 µm, anything larger than 55 µm was considered a clump. The

frequency of agglomeration was then determined as the number of clumps per square cm of

membrane according to equation 1. Two difference locations per membrane were analyzed.

$$f_a = \frac{N_{dp55}}{cm^2}$$
(1)

2.6. Dye Filtration and Rejection

The feed solution was 0.1 g/L aniline blue with a pH of 6.0. A dead end filtration set up was

used with an exposed membrane area of 17 mm. Membranes were supported by a coarse mesh

and the exposed area was controlled with a Teflon washer. The solution was pressurized to 2

bar with nitrogen. A nitrogen sweep gas was also used on the permeate side to prevent adhesion

and minimize concentration polarization. The permeate was collected and the amount

quantified gravimetrically. The concentration of dye in the permeate was quantified by a

calibrated UV-Vis absorbance peak at 595 nm, according to Beer's law. The correlation was

linear with an R^2 of 0.97. The rejection was calculated according to Eq. 2:

$$R = \left(1 - \frac{C_{perm}}{C_{feed}}\right) * 100$$
(2)

C_{perm} is the concentration of the permeate and C_{feed} is the initial feed concentration.

2.7. Dye Adsorption on AC

To understand the contribution of dye adsorption onto AC during filtration, batch adsorption

studies were performed. A ratio of 2.5 mL dye to mg of AC was vigorously mixed for various

times and the residual concentration was measured. Kinetic isotherms were constructed using common models to determine the dye of adsorption. The concentration after adsorption was also found using UV-Vis.

2.8. Scanning Electron Microscopy (SEM)

SEM images of membranes were taken using a Hitachi SU8010 field emission scanning electron microscope. Membrane were sputter coated for 30 seconds with a gold/palladium coating before imaging. The cross section was exposed by cutting with a sharp blade.

2.9. Experimental Design

The full factorial design was chosen because it can help determine the response of each factor and the interactions between factors. Moreover, factorial designs are often used to narrow the important factors associated with membrane formation and performance [27,28] The randomized design was created using Minitab 18. The following high and low values were chosen for each factor based on previous experimental observations. AC concentration higher than 10 wt.% (relative to the polymer) tend to result in surface ruptures. Concentrations of PEG higher than 20 wt.% (relative to the polymer) result in membranes too facile for testing at 2 bar.

Table 10: Factors and factor levels used for the experimental design. PEG and AC concentrations are on a per PSF basis (i.e. 20% PEG corresponds to 0.2g PEG per 1 g PSF).

Factor	Coded Factor	Type	High	Low
PEG %	A	Continuous	20	3
AC %	B	Continuous	10	0.5
Solvent	C	Categorical	DMF	NMP

3. Results and Discussion

Factorial analysis was performed by Minitab 18 according to standard statistical methods [29]. For all cases the coded factors are represented by: A = PEG%, B = AC%, and C = solvent. Two replicates were performed at each corner point, for a total of 16 experiments shown in table 11.

Table 11: Randomized 23 experimental design with 2 replicates of each corner point

Run order	PEG%	AC%	Solvent	Contact Angle (°)	Agglomeration Frequency	Flux (LMH)	Rejection (%)
1	3	0.5	DMF	58.6	70	2.37	89.70
2	20	10.0	DMF	57.8	1284	27.89	98.40
3	3	0.5	NMP	66.9	150	5.28	77.00
4	20	0.5	NMP	46.9	146	51.67	82.86
5	3	0.5	DMF	48.0	104	11.50	81.00
6	20	0.5	DMF	75.9	108	48.12	70.76
7	20	10.0	DMF	84.8	1210	119.00	97.89
8	3	0.5	NMP	65.2	182	19.82	76.68
9	20	10.0	NMP	51.6	1120	19.03	85.74
10	3	10.0	DMF	51.2	1654	21.01	84.35
11	20	0.5	NMP	52.7	118	77.56	58.77
12	3	10.0	NMP	45.0	1442	4.23	90.30
13	3	10.0	NMP	38.3	1250	5.10	61.03
14	3	10.0	DMF	71.3	1574	16.78	99.29
15	20	0.5	DMF	83.9	42	69.52	40.00
16	20	10.0	NMP	50.8	1272	14.14	96.30

The morphology of each membrane reveals much about the role of PEG and AC. Figure 2 shows SEM images of selected membranes. The asymmetric structure consisting of a top skin and spongy support is evident regardless of casting solution composition. However, when DMF was used as the solvent, the spongy support appears more homogenous (figure 26a) whereas NMP results in some less spongy areas in the cross section (figure 26b). The presence of PEG results in surface pores on the order of 0.5μm. This is in the microfiltration regime, suitable for dye filtration. The pores size distribution is relatively narrow and is seen in figure 26c. When More than 10% AC is used, particle ruptures occur as shown in figure 26d. These ruptures lead to larger surface pores and blockage.
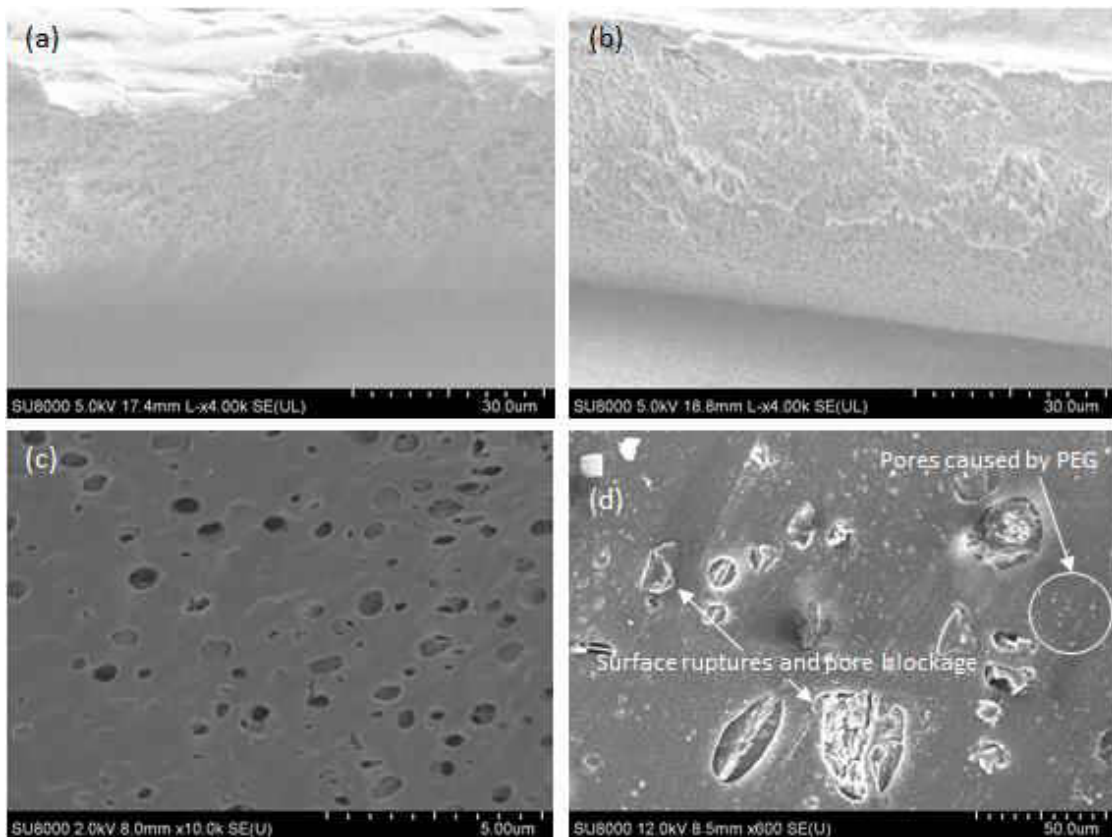
Figure 26: Cross section of membranes form run (a) 2 and (b) 9 showing a subtle difference between solvents. (c) Surface pores as a result of PEG diffusion from the membrane during inversion. (d) Example of AC surface ruptures with loading greater than 10%.

3.1. Effects on Water Contact Angle

The water contact angle is widely regarded as a measure of membrane wettability. Contact angles measuring less than 90° indicate hydrophilic surfaces (low energy), and angles greater than 90° are representative of hydrophobic surfaces (high energy). For liquid phase separation, generally a relatively low contact angle is beneficial because the surface is able to become thoroughly wetted, maximizing the areas available for diffusion into the membrane surface. Generally, lower contact angles tend to represent higher flux in membranes.
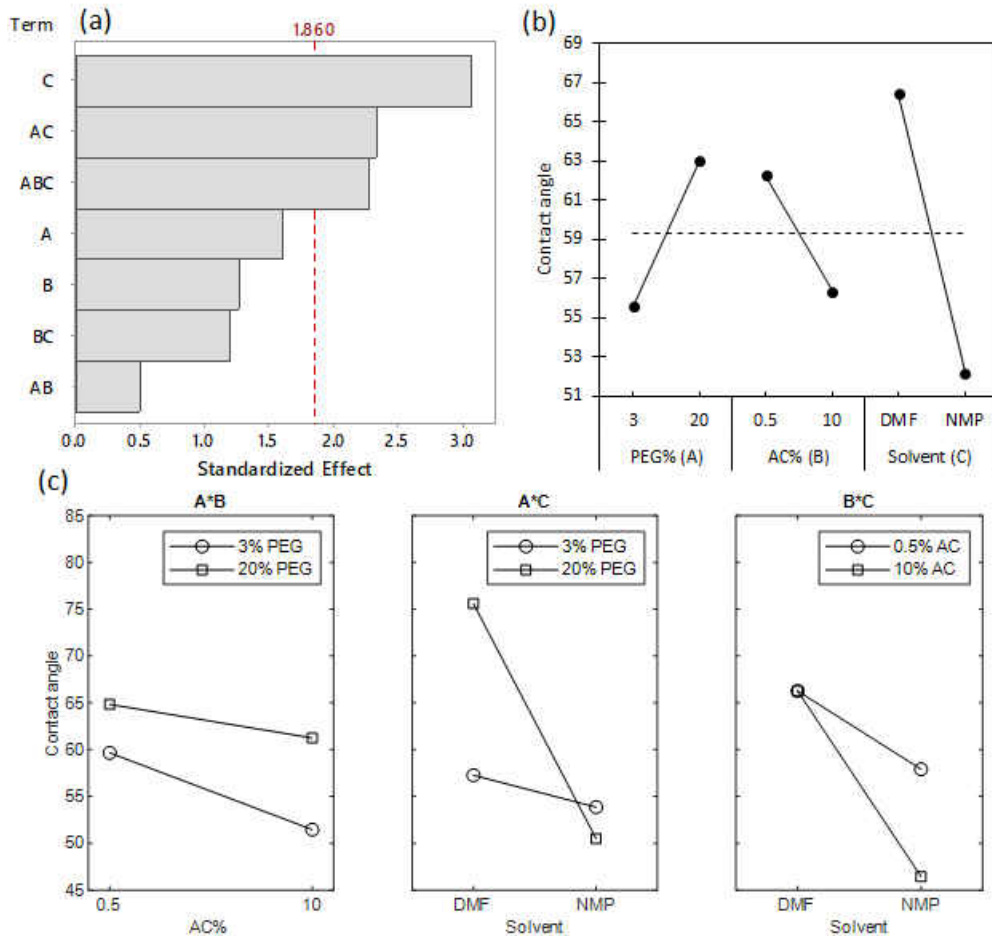
Figure 27 : (a) Pareto daigram, (b) main effects, and (c) interaction effects on water contact angle. Analysis was performed with a 90% confidence level.

100

On the other hand, the contact angle is also used as a predictor to fouling. Depending on the type of foulant, either higher or lower contact angles can indicate higher attraction. In the case of aniline blue, lower contact angles (more hydrophilic) tend to indicate higher fouling potential [30]. Due to the moderate difficulty in accurately measuring the water contact angle with the method utilized, a confidence level of 90% was used for this analysis. The effects are depicted in figure 27.

From this, it is evident the solvent choice was the only significant main effect, and there was a two level interaction between PEG concentration and solvent, and a three level interaction. Figure 27 depicts the main effect plots and significant interactions. The interaction plot shows that when DMF is the solvent, lower contact angles are observed when low concentrations of PEG are used. However, when NMP is the solvent, higher contact angles are observed when PEG concentrations are low. Although the AC concentration did not have a significant effect on contact angle, it was apparent that higher amounts of AC lead to lower angles. This is due to the hydrophilic nature of AC and possibly the increase in surface roughness. This phenomena has been well documented [8,31]. These results have several implications for potential fouling behavior. Since higher contact angles tend to result in less fouling, it seems the best membrane in terms of fouling resistance would be made with high PEG, low AC, and DMF as the solvent.

3.2. Effects on Agglomeration Frequency

Particle agglomeration is a negative result of poor polymer/filler interactions. Currently, the most common methods of speculating about agglomeration are through thermal and mechanical analysis [32]. Both of which yield qualitative observation. Here we present an imaging tool that can be used to quantitatively measure agglomeration frequency defined by

equation 1. This method proved useful for AC-PSF membranes because it could accurately image relatively large black particles in a white PSF matrix. If smaller particles are used, or if particles are not differentiable by optical microscopy, this method may not be useful. Other limitations to this method are failure to consider agglomerations less than 55µm. In order to do so, a comparison of the size distribution of AC before and after being introduced into PSF would be necessary. That qualitative comparison would not be useful for a statistical analysis. Also, this method does not consider the number of particles and does not normalize the number of agglomerations to the total particles present. If the total number of particles was considered, the analysis would be less accurate because of too low resolution to differentiate small particles from the matrix, thus an inaccurate count of total particles would result.
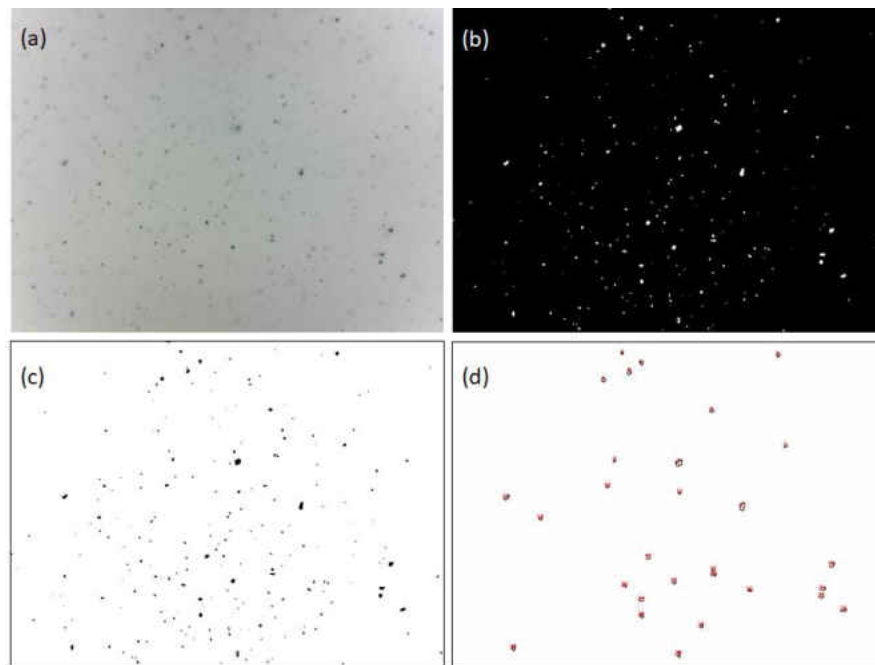
Figure 28: (a) raw optical micrograph of AC-MMM transformed into (b) black and white image, then (c) inverted to show particles as black dotes. (c) ImageJ particle analyzer was used to locate and label particles larger than 55 µm.

So, it is immediately expected that increasing the concentration of AC will increase the agglomeration frequency. None the less, this microscopy method allows for a quantitative determination and gives much insight into the agglomeration trends. Optical micrograms of

each sample was taken, processed and analyzed. An example of the output from this analysis is shown in figure 28.

The measurement of agglomerations was fully automated, so a 95% confidence level was used for the analysis. From figure 29a, it is readily apparent that the factor with the strongest effect on agglomeration frequency was the concentration of AC, as expected. The other main effect was PEG concentration, with weak PEG%-AC% and AC%-solvent interaction effects.
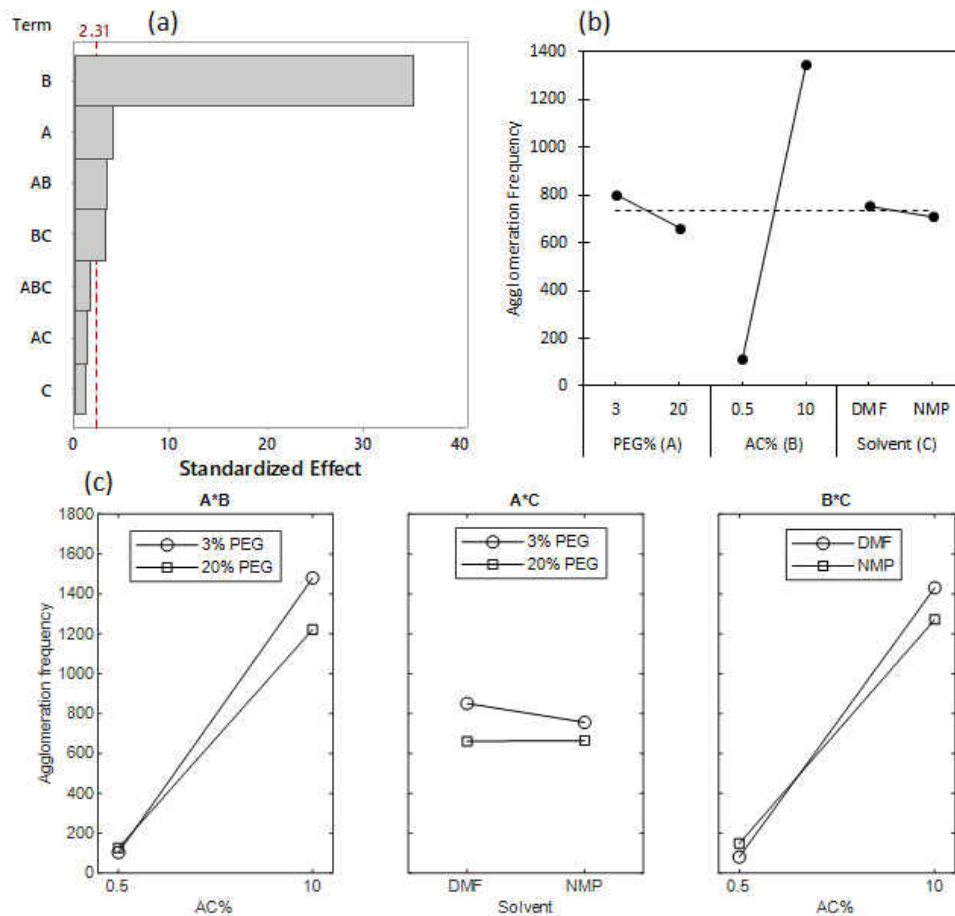
Figure 29: (a) Pareto diagram, (b) main effects, and (c) interaction effects on agglomeration frequency performed at 95% confidence.

The main effects are shown in figure 29b. It is logical and frequently observed that increasing the filler concentration (AC) in the membrane increases agglomeration. As more

particles are introduced, the more likely they are to form a clump due to space limitations in the membrane and intermolecular attraction between AC particles. The decreasing trend with increase PEG concentration can prove beneficial. There are two likely causes to this trend. One could be the addition of PEG into the casting solution lowered the viscosity and allowed for better dispersion of AC in the casting solution. The other cause could be the result of improved AC-PSF interaction caused by a decrease in the demixing rate during phase inversion. This would allow for increased contact time between the AC particles and the dissolved polymer, promoting stabilization. It is also worth noting that there was also a tendency of the AC to migrate to the top dense layer of the membranes. Creating an AC rich top layer and a relatively PSF rich bottom layer.

The interaction plots in figure 29c also show insightful trends. It seems when NMP was used as a solvent, a higher agglomeration frequency was observed at low AC concentrations, but a lower frequency at high concentration. Higher PEG concentrations seemed to reduce agglomerations more effectively when higher concentrations of AC were used.

3.3. Effects on Flux

Flus (measured in $Lm^{-2}hr^{-1}$ or simply LMH) is one of the most important parameters in membrane performance. High flux is more desirable than lower flux. However, membranes generally have a flux/rejection tradeoff. So these values should be optimized to find appreciable flux and high rejection. None the less, the analysis revealed the only PEG concentration had a significant effect on flux. Interestingly, AC concentration had the lowest effect. This is significant because it signifies no surface ruptures or pore blockage was caused by AC. This would have resulted in a significant increase in flux in the case of surface ruptures, or a significant decrease in flux for the case of pore blockage.
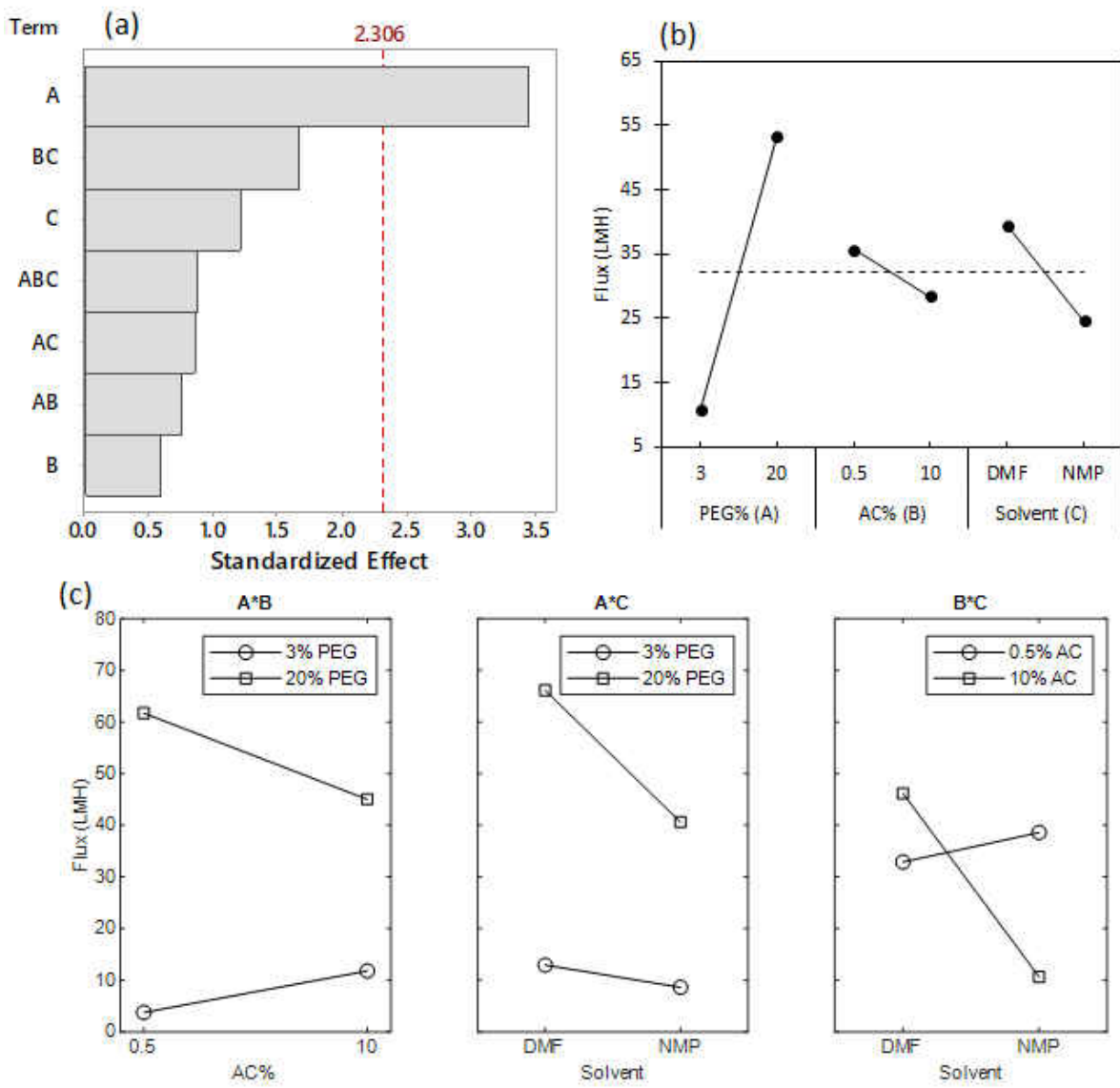
Figure 30: (a) Pareto diagram, (b) main effects, and (c) interaction effects on flux performed at 95% confidence.

Figure 30b shows a dramatic increase in flux with an increase in PEG concentration. This is likely due to pore formation, as PEG is water soluble and escapes from the membrane during the phase inversion process, leaving behind surface pores. It is interesting that the flux was higher when DMF was used as the solvent. This is consistent with the SEM images showing a more spongy cross section between figure 26a and 26b. This may also be a result of an increase in d-spacing when DMF is used, as was reported by Adewole, et al. [21]. Although not statistically significant, it is also worth noting the AC/solvent interaction shown in figure

60c. When DMF was used as the solvent, a higher flux was seen with 10% AC. On the other hand, when NMP was used as the solvent, higher flux was seen with 0.5% AC. This signifies the role of solvent on AC-PSF interaction during formation. It seems pore blockage occurred when NMP was used with 10% AC but not with 0.5% AC. Another plausible scenario is PSF clogging pores in the AC. A thorough investigation into the demixing kinetics during formation may help explain this observation. However accurately representing the complex AC-PEG-solvent-water system would be challenging.

3.4. Effects on Rejection

Dye rejection is the other important performance parameter. The Pareto diagram in figure 31a shows AC is the only significant factor influencing dye rejection, followed closely by the two-way interaction between AC and PEG concentration.

The main effect due to AC shown in Figure 31b depicts the average increase in dye rejection from 72% to 89%. This is likely a result of adsorption by the AC. At higher concentrations, there is an increased capacity for adsorption. This result is significant, because it means the active sites available for adsorption were not impeded by the number of AC particles in this concentration range. Although not stastically significant, it is interesting to note that the rejection was lower when NMP was used as the solvent. Because the same trend was seen in flux performance, this is likely a result of PSF clogging pores in the AC, reducing the number of active site available for adsorption in those instances. The interaction plot in figure 31c also shows interesting results. When 3% PEG was used, the rejection was almost the same despite the amount of AC. However, when 20% PEG was used, there was a large increase, from 63% to 95%, in rejection. This is indicative of decreased agglomeration defects creating more adsorption active sites. The insignificant PEG/solvent interaction is also worth

106

mentioning. In this case, the rejection/flux tradeof is somewhat apparent when DMF was used as the solvent. Membranes made with DMF saw higher rejection with 3% PEG compared to 20% PEG. In the same way, the flux was much lower with3% PEG than 20% PEG. When NMP was used, there is no difinitive tradeoff seen.
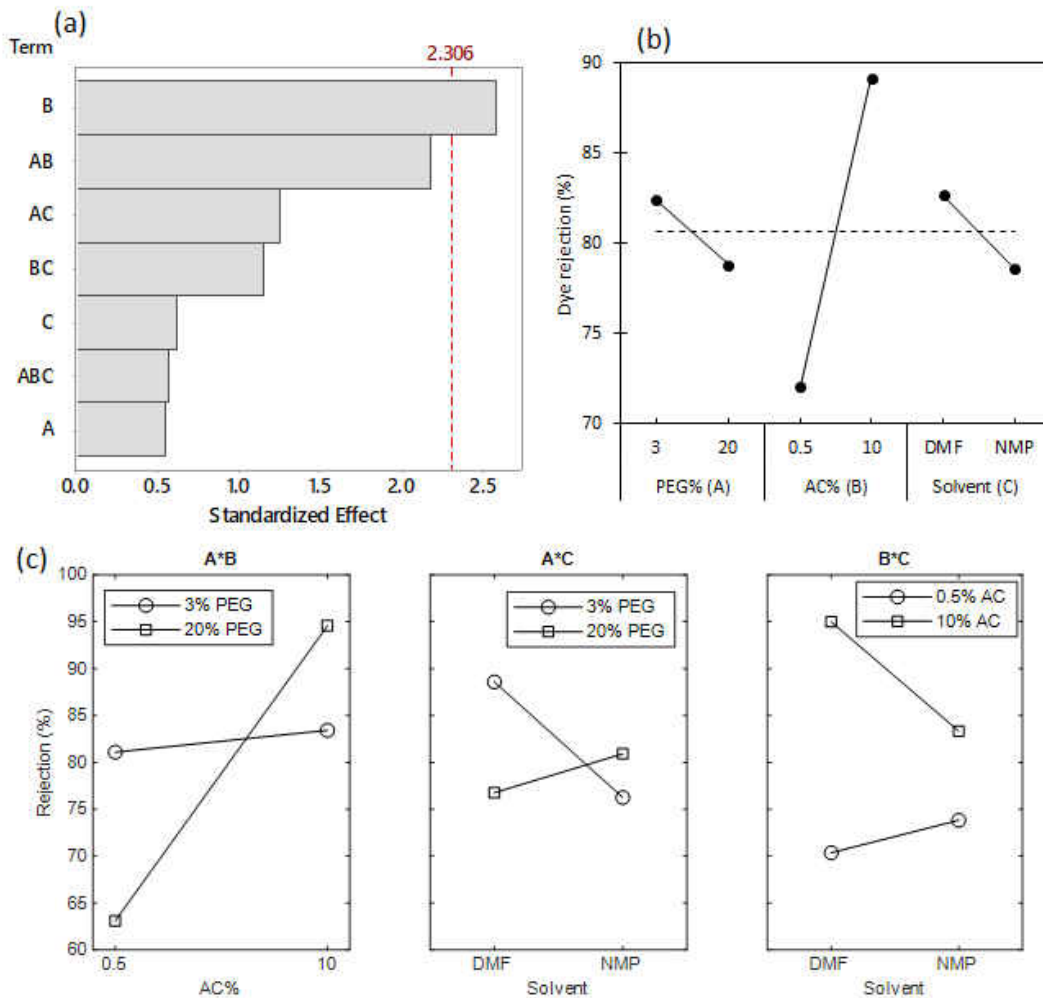
Figure 31: (a) Pareto diagram, (b) main effects, and (c) interaction effects on dye rejection performed at 95% confidence.

3.5. Response Optimality

The response optimizer in Minitab was used to determine the optimal conditions in terms of maximum flux, maximum rejection, and minimum agglomeration frequency and maximum contact angle. Maximizing flux and rejection are logical parameters. Minimum agglomeration

107

frequency resembles fewer defects. Maximum contact angle represents lower fouling potential. The data was shown to be optimal using 20% PEG, 5.2% AC, and DMF as the solvent. The intermediate results are shown in table 12.

Table 12: Response optimization data using equal weights for each factor while maximizing dye rejection, maximizing flux, and minimizing agglomeration frequency.

Response	Outcome	Desirability	Optimal Predicted Value	Composite Desirability
Dye rejection	Maximize	0.61640	76.55	
Flux	Maximize	0.54607	66.06	0.6398
Agglomeration frequency	Minimize	0.61968	655	
Contact Angle	Maximize	0.80321	75.7	

Although the optimal results were found, it is likely a range of results is sufficient for some applications. To study this, overlaid contour plots were made holding the solvent constant (Figure 32). Dye rejection was taken as the more important response, so the range was assigned to be greater than 80%. Flux was more variable, but was chosen to be greater than 20 LMH. The plots indicate that when DMF is used as the solvent, moderate amounts of AC and a wide range of PEG concentrations achieve the defined bounds. If NMP is used as the solvent, a much narrower range of both AC and PEG are required.
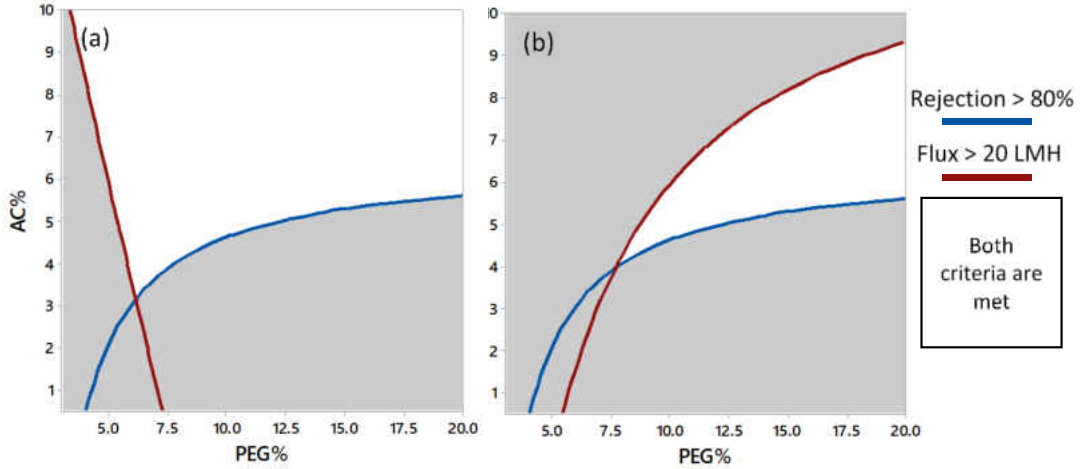
Figure 32: Overlaid contour plots showing the range of rejection greater than 80% and flux greater than 20 LMH holding the solvent constant with (a) DMF and (b) NMP

3.6. Adsorption Kinetics

To better understand the role of adsorption on dye rejection, kinetic isotherms were constructed and fitted to three common models:

Pseudo 1st order

$$\log(q_e - q_t) = \log(q_e) - \left(\frac{k_1}{2.303}\right)t \tag{3}$$

Pseudo 2st order

$$\frac{t}{q_t} = \left(\frac{1}{k_2 q_e^2}\right) + \left(\frac{1}{q_e}\right)t \tag{4}$$

Intra-particle diffusion

$$q_t = k_{id}t^{\frac{1}{2}} + C_{st} \tag{5}$$

In these models, q_e and q_t and the equilibrium and time dependent dye adsorption per mass of AC, k and C_{st} are the respective constants, and t is the contact time. Isotherms were taken at a dye concentration of 0.1 g/L and a pH of 6. Comparing the correlation coefficient of each linearized model listed in table 13 demonstrates the pseudo second order model most

accurately depicts the data. The model is graphed in figure 33 against the experimental data. This is indicative of chemisorption of dye by the AC.

Table 13: Kinetic isotherm parameters

Model	R^2	q_e (mg/g)	k	C_{st}
Pseudo 1st order	0.9279	132	0.382	-
Pseudo 2nd order	0.9976	238	0.0042	-
Intra-particle diffusion	0.711	-	38.81	76.81
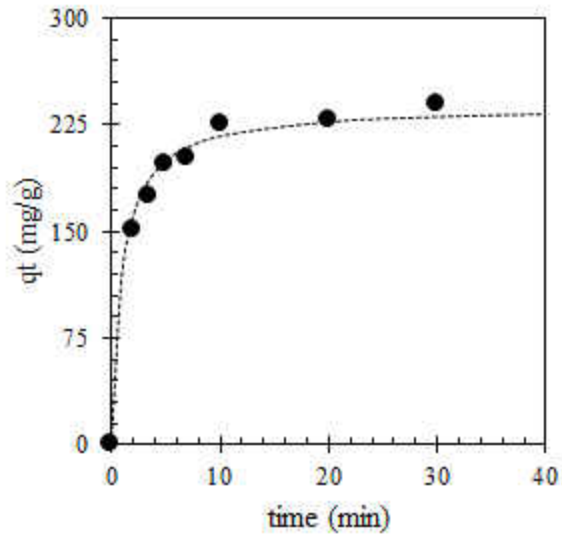
Figure 33: Adsorption kinetic results fitted to a pseudo second order kinetic isotherm.

The transient adsorption capacity reveals that AC regeneration would be required after about 30 minutes of filtration. The short residence time within the membrane, and hence the short contact time between AC and dye as well as the trends mentioned previously, indicate adsorption could not have been the only mechanism responsible for rejection. A combination of size exclusion and adsorption was responsible.

4. Conclusion

A replicated 2^3 full factorial design was used to screen the response of PEG concentration, AC concentration, and two solvents (DMF and NMP) on water contact angle, agglomeration frequency, flux and aniline blue rejection by an AC-PSF MMM. Solvent, PEG%/Solvent interactions, and a three-way interaction was shown to have a significant effect on water contact angle. Agglomeration frequency was strongly influenced by AC% and PEG%. Increased AC% resulted in higher agglomeration frequency, and increasing amounts of PEG% effectively reduced the agglomeration frequency. Weak two-way interaction between PEG%/AC% and AC%/Solvent also had a significant effect on agglomeration frequency. Flux was influenced by PEG% as a result of surface pore formation. Dye rejection was influenced by AC% as a result of increased adsorption capacity. Optimal values and operating ranges were also presented within the range of factor levels chosen. Kinetic adsorption isotherms were fitted to models which indicated chemisorption of aniline blue by the AC.

CHAPTER V: CHEMICALLY ACTIVATED BIO DERIVED CARBON/POLYSULFONE MIXED MATRIX GAS SEPARATION MEMBRANES

Abstract

In this paper, we present activated carbon (AC) mixed matrix membranes with a polysulfone matrix for separation of binary N_2/CH_4, $CO_2/CH4$, and CO_2/N_2. The influence of chemical activating agent on AC surface functional groups was exploited to study how functional groups influence AC-MMM performance. Bio-based AC was used for its diverse composition of functional groups and these functional groups are influenced by chemical activation. It was observed that hydroxide groups on the AC resulted in the best performance due to strong compatibility with AC. Although slightly polar, ether groups on AC did not improve compatibility. As a result, sodium hydroxide and zinc chloride activating agents seem to result in strong AC-PSF compatibility.

1. Introduction

Mixed matrix membranes (MMMs) are a promising class of membrane to surpass the permeability/selectivity limitations of polymeric membranes. By introducing a particle phase into a polymer matrix, multiple mechanistic pathways are formed, and can be exploited for specific separation applications [1]. Specifically, gas diffusion through the pores of the filler tends to enhance its permeability. One of the most important aspects of MMM development is choice of polymer/filler combination. Their individual properties and their compatibility dictate the extent of performance. Poor compatibility will result in interfacial defects in the

vicinity of the filler particles, and will inevitably lead to unselective membranes [2]. This has been the ultimate challenge of MMM development, and thus much research has focused on methods to prevent or correct the poor compatibility. For example, particle size is highly influential. However, depending on the type of filler, either smaller or larger particles tend to produce fewer defects and perform better. Lainez et at. found that 150nm ZIF-8 particles performed better than 50 nm particles for H_2/CO_2 separation [3]. Contrarily, Ghalei et al. found that 20-30nm MOF particles tended to disperse better in the matrix preventing interfacial defects and performed better than 100-200nm particles [4]. Due to these discrepancies, it appears there are complex interacting effects between particle size, surface area, and particle functional groups on defect formation that is not well understood.

Other strategies to improve interaction is by priming particles with a polymer, effectively creating a three phase region consisting of the matrix/primer/filler [5]. This can increase the compatibility by lowering the surface tension between particle and matrix, reducing defects upon membrane formation. Thermal annealing above the matrix glass transition temperature has also shown to increase filler/matrix compatibility by relaxing the matrix chains, initiating intimate contact between polymer and filler [5-7]. Considering the formation of MMMs is highly dependent on the thermodynamics of the casting solution, some works have discovered this equilibrium can also influence defect formation and performance. For example, other than the choice of filler and matrix, the solvent, and nonsolvent for wet phase inversion membranes, also plays an important role in compatibility [8,9]. The solvent can potentially degrade the filler if not chosen properly [9], but more importantly, equilibrium conditions during formation can create local areas of concentrated solvent, nonsolvent, and polymer, preventing compatibility [8].

Furthermore, function-led design has been recognized as the most influential aspect of influencing matrix/filler compatibility [10-12]. Introducing fillers to matrices with compatible functional groups increases the likelihood of strong interactions forming between them. This reduces the presence of interfacial defects. Depending on the type of filler, functionalization can be achieved by various methods. In engineered particles, using precursors that have the desired functional groups is an effective method. Various functional groups can also be attached chemically by grafting or physically through strong intermolecular bonds. One popular species used for grafting is silane. Various forms of silane are available with different functionality [11,13]. An example of physical grafting was shown by Saranya et al. in which particles were functionalized onto alginate aggregates [14]. Similarly, the polymer phase of the MMM can be functionalized with various functional groups to achieve compatibility [15].

Although not used as frequently as more advanced fillers such as MOFs and zeolites, AC has had minor success in separating gases and has given some insight into the field [17-20]. Notable progress with AC-MMMs is improved permeability with maintained selectivity and rigidification of polymers by incorporating AC. None however, have investigated how the AC functional groups can be manipulated to achieve better performance. Some methods work well for some fillers and matrix combinations. In this work we utilized activated carbon (AC) derived from sunflower hulls as the filler in a polysulfone (PSF) matrix. AC is a versatile material which is porous, has high surface area, and most importantly, is full of functional groups that can be influenced by various means. Producing AC from biomass is one of the methods to achieve desired functional groups due to the complex structure of lignin, cellulose, and hemicellulose [16]. One process to convert biomass into AC is through pyrolysis of the biomass into biochar, then chemical activation in an inert atmosphere at elevated temperatures.

Depending on the activating agent, temperature, residence time, heating rate, and precursor biomass, various functional groups remain post processing. It is our hypothesis that this "functionalization" can be exploited to produce AC-MMMs for gas separation of CO_2, N_2, and CH_4 gas pairs. Both the inherent properties of the AC, and the compatibility of AC with PSF are suspected to be contributing factors. Three activating agents were chosen based on their oxidizing features: NaOH, H_2O_2, and $ZnCl_2$.

2. Materials and Methods

2.1. Materials

Raw sunflower hulls were supplied by CHS Grandin, Grandin, North Dakota and were used as the AC precursor. Sodium hydroxide (NaOH) 50 wt.%, hydrogen peroxide (H_2O_2) 30 wt.%, and zinc chloride ($ZnCl_2$) were purchased from sigma Aldrich and were used for chemical activation. Hydrochloric acid used for AC rinsing and purifying purchased from Fisher Scientific. N,N-Dimethylformamide (DMF 99.8%) and polysulfone (PSF 35,000 Da) used for membrane fabrication were purchased from Sigma Aldrich. Argon, nitrogen, carbon dioxide, and methane were purchased from Praxair in analytical grades.

2.2. AC Production and Characterization

About 50g of sunflower hulls were loaded into a one-liter Thermolyne 21100 fixed bed tube furnace reactor with temperature and heating rate control. Pyrolysis was achieved by purging the reactor with argon for about five minutes, then heating from room temperature to 500°C at a rate of 15°C/min under continuous argon flow. The reactor was held at 500°C for 20 minutes, then allowed to cool slowly back to room temperature. Volatiles, bio oils, and tars were continuously discharged into a water bath. Biochar was collected from the reactor.

The biochar was washed thoroughly with distilled water until a clear filtrate was seen. Then, it was washed with 5 wt.% hydrochloric acid, at a ratio of 5mL to 5g char, to remove trace salts and residual bio-oils. It was then ground with a mortar and pestle and sieved with a #270 sieve tray for less than 55μm particle size. Varying amounts of activating agent (NaOH, H_2O_2, or $ZnCl_2$) were then impregnated into ground biochar, by mixing then evaporating excess water. In the case of H_2O_2 activating agent, evaporation was not carried out due to its low boiling point. The impregnated biochar was loaded into the tube furnace and heated again at a rate of 15°C/min to a final temperature of 700°C under argon flow, held for 20 minutes at 700°C, then allowed to slowly cool to room temperature.

The AC was recovered and rinsed with 5 wt.% hydrochloric acid to remove residual activating agent, then with water to remove residual acid. The AC was either ground or micronized in a micronizing mill, and the size distribution and pores were investigated using scanning electron microscopy. The surface area was determined by means of iodine number which was evaluated according to ASTM standard D4607 [21]. AC functional groups were investigated with a Thermo Nicolet FTIR with a ZnSe crystal in attenuated total reflectance mode.

2.3. MMM Formation, Characterization, and Gas Permeance

Appropriate amounts of AC were initially dissolved in DMF and mixed vigorously for at least 24 hours to allow for degassing. PSF was added in three parts over 48 hours to the AC/DMF solution to prime the AC, and eventually create a 20 wt.% PSF in solvent with between 0.25% and 2% AC relative to PSF. Once all polymer was added, the solution was mixed with a magnetic stirrer at 60 rpm for at least 24 hours. Before casting, the solutions were removed from the stirrer and allowed to sit for several hours to remove bubbles that formed from stirring.

A 50 micron casting blade measuring 3 inches wide was used to cast the solution on a Duran®

glass plate. About 10 cm of membrane was cast manually at a comfortable rate of about 5

cm/sec. The membranes were then precipitated by wet phase inversion in distilled water to

form asymmetric MMMs. To investigate the influence of thermal annealing on gas separation

performance, MMMs were then heated at a rate of 5°C/min to 200°C for two hours, then

allowed to slowly cool to room temperature.

Membranes were inspected visually with light microscopy for interfacial defects, and

migration of AC to the dense skin by qualitatively viewing the top and bottom surfaces. SEM

was used to view the MMM cross section and to check for particle ruptures through the surface.

The permeance of pure CO_2, N_2, and CH_4 through the MMMs were investigated using the

constant pressure variable volume method. The MMMs were supported with a porous steel

mesh. The pressure was monitored with a pressure gauge and the flow rate of each gas was

measured with a soap bubble flow meter. The same membrane was used for each gas in the

order of N_2, CH_4, then CO_2, to limit the effects of potential plasticization due to CO_2. Several

data points were taken to ensure steady state.

3. Results and Discussion

3.1. AC Production and Characterization

In order to produce AC with desirable properties, biochar was impregnated with three different

activating agents and activated at various temperatures. NaOH was used as a model agent to

determine the best temperature to perform the activation. As shown in Figure 34, the activating

agent, impregnating ratio, and temperature all influenced the AC surface area as measured by

iodine number. While the biochar properties would likely also influence these results, the

parameters used to create biochar was held constant according to our previous work. A control was used to rule out temperature effects without any activating agent. It is apparent that without any activating agent, the AC iodine number was very similar to biochar, with a slight increase as temperature increased as expected. When NaOH was used, the iodine number followed a parabolic trend, which is commonly encountered. It peaked near 700°C, so this was the temperature used for the remaining AC. What is also apparent is an increase in iodine number when higher concentrations of activating agent were used.
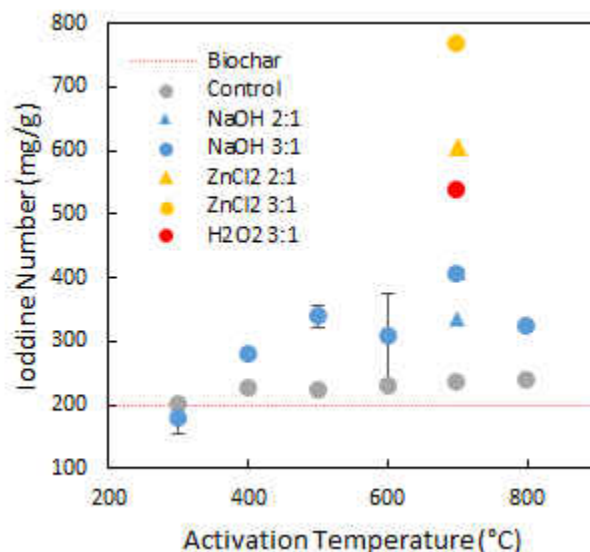
Figure 34: Iodine number for chemically activated biochars

The surface functional groups were also influenced by the activating agent. This is depicted by the FTIR spectra in Figure 35. Each AC shows aromatic functional groups at wavenumbers less than 1000 cm^{-1}. Other similarities between the three includes a C=C peak around 2300 cm^{-1}, carbonyl C=O at about 1650 cm^{-1}, and alkane and alkene CH stretching peaks between 1200 and 1400. Important differences are the OH stretch in AC-NaOH at 3500 cm^{-1}, and ether C-O-C stretch at 1120 and 1250 cm^{-1} in AC-H$_2$O$_2$. From this analysis is it apparent that the potential for strong intermolecular bonds between AC and PSF will likely be

greatest in AC-NaOH due to hydrogen bonding from the OH functional groups, then AC-H_2O_2 from the ether linkages. AC-$ZnCl_2$ appeared to have fewest oxide groups and is expected to form weaker intermolecular bonds with PSF. It is worth noting that the highly aromatic nature of AC will result in pi stacking between the rings in the AC and PSF, contributing to intermolecular bonding [22].
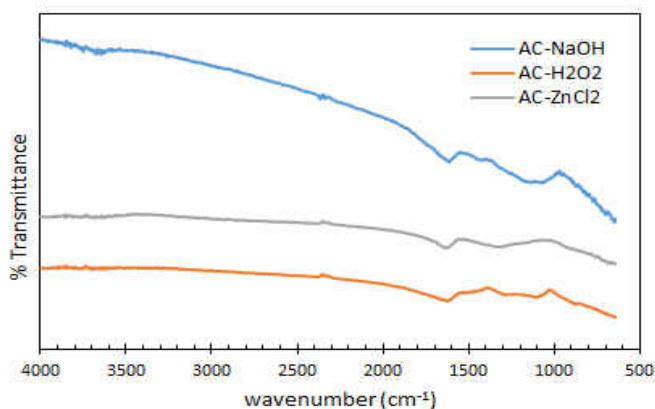
Figure 35: FTIR spectra of each AC listed by activating agent.

From the SEM images in Figure 36a, a variety of pores are apparent in the powered AC. The pore size is on the order of 1μm. Because pore diffusion in MMMs through the AC is expected to occur, 1μm pores are not ideal because it would result in unselective flow through them. The pore size of micronized AC seen in Figure 36b is apparent, but is much smaller than 1μm. This yields the possibility of selective flow through the pores of the AC.
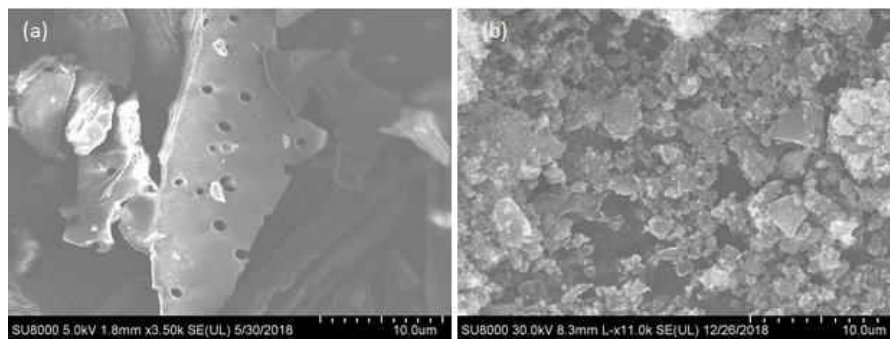
Figure 36: SEM images of (a) powdered and (b) micronized AC

To investigate the influence of functional groups on AC-MMMs while reducing the effect of surface area, AC with similar iodine numbers were chosen for MMMs listed in Table 14. To understand the influence of large pore size AC, one powdered AC was also used. While particle size may have an impact, it is expected the difference in pore size will be the dominant factor. The particle size distribution of each AC is shown in Figure 37.
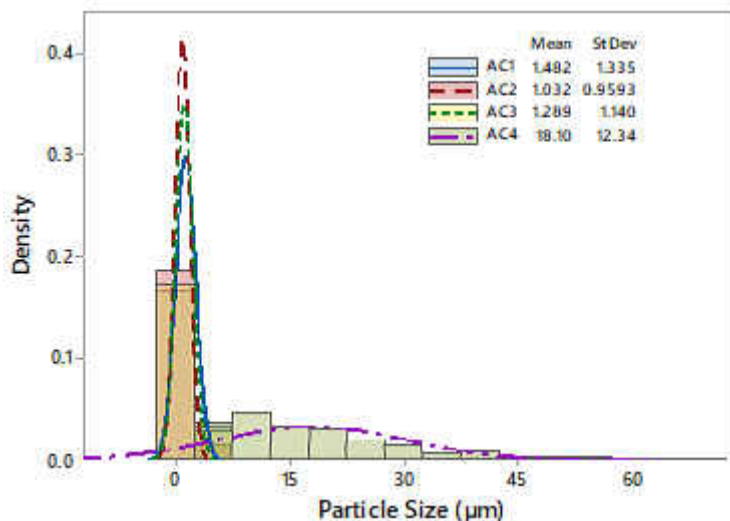
Figure 37: Particle size distribution for AC1-AC4 used for MMM fabrication.

Table 14: AC used for MMM fabrication.

AC	Activating Agent	Impregnation Ratio (Agent:Biochar)	Iodine Number (mg/g)	Average Diameter (µm)
AC1	NaOH	3:1	405.0	1.482
AC2	H_2O_2	3:1	536.2	1.032
AC3	$ZnCl_2$	2:1	605.5	1.289
AC4	NaOH	3:1	405.0	18.10

3.2. MMM Characterization and Performance

MMMs were made with each AC and thermally annealed. MMMs made with AC4 were not annealed due to poor performance. From optical micrographs in Figure 38a, it was apparent that there was some void space surrounding AC2, but not AC1, AC3, or AC4, forming a sieve

in a cage morphology. This was an interesting result because AC2 showed signs of ether groups and was expected to possess higher potential for intermolecular bonding that AC3. This could be a result of ether aromatics which could potentially weaken pi stacking, causing weaker interactions compared to AC3, which did not show signs of polar groups. Another possibility is the ether groups were sterically hindered in the AC structure, limiting its interaction with PSF.

SEM images revealed an asymmetric cross section in all AC-MMMs. A representative example is shown in Figure 38b. The selective layer was especially thin compared to those reported in pristine PSF membranes [23]. It is expected thermally annealed MMMs had a denser cross sectional based on the color change from white in the asymmetric to clear. It should be noted that AC tended to reside in the top layer rather than remained dispersed upon wet phase inversion. This is significant because for AC to influence permeability in asymmetric membranes, the dense layer must be penetrated slightly. It appears this was the case based on the top of the MMMs being darker in color than the bottom, which has also been reported previously [24].
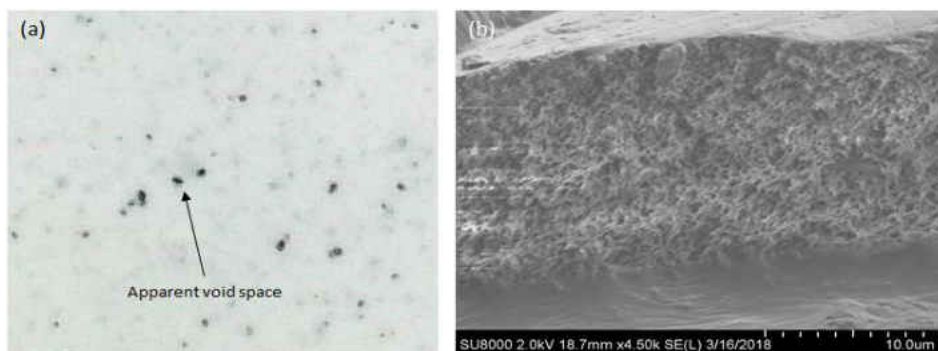
Figure 38: (a) Optical micrograph showing a shiny area surround AC2-MMM and (b) SEM image showing a representative cross section of all AC-MMMs.

Each membrane was subject tested for N_2, CH_4, and CO_2 permeance. The permeance was calculated according to equation 1 [25],

$$P = \frac{22{,}414 \ p_1}{A \ (p_2 - p_1) \ RT} \frac{dV}{dt} \tag{1}$$

where p is pressure, A is membrane area, R is the gas constant, T is temperature, and dV/dt is the volumetric flow rate and is in units of $cm^3(STP)/(cm^2scmHg)$. The permeance in units of GPU is equivalent to 1×10^{-6} $cm^3(STP)/(cm^2scmHg)$ and is used instead of permeability (barrer) because of the difficulty and inaccuracy in measuring the active layer of the AC-MMMs.

The permeation results are depicted in Figure 39. Generally, there was an increase in gas permeance with AC loading, as expected. It was also apparent that the permeance was lower in annealed membranes compared to non-annealed MMMs. This is likely due to an increase in active layer thickness with the thermal annealing causing more resistance to flow. AC1-MMMs seemed to perform best. Interesting, AC2-MMMs did not perform well, showing extremely high permeance in the Knudsen flow regime. This is most likely due to the poor interfacial interactions which caused void space surrounding the AC particles and allowed for unselective diffusion. Another interesting point is in AC3 annealed MMMs, there was an initial decrease in CO_2 permeance compared to pristine PSF. This could be a result of pore blockage by PSF as a result of the thermal annealing. Another possibility is adsorption was a competing mechanism where the rate of adsorption was faster than diffusion for low AC loadings. However, this is slightly less likely because that trend was not seen in the un annealed MMMs. AC4-MMMs (not shown) showed Knudsen flow for the entire span of AC loading. This was expected due to the large pore sizes in AC4.
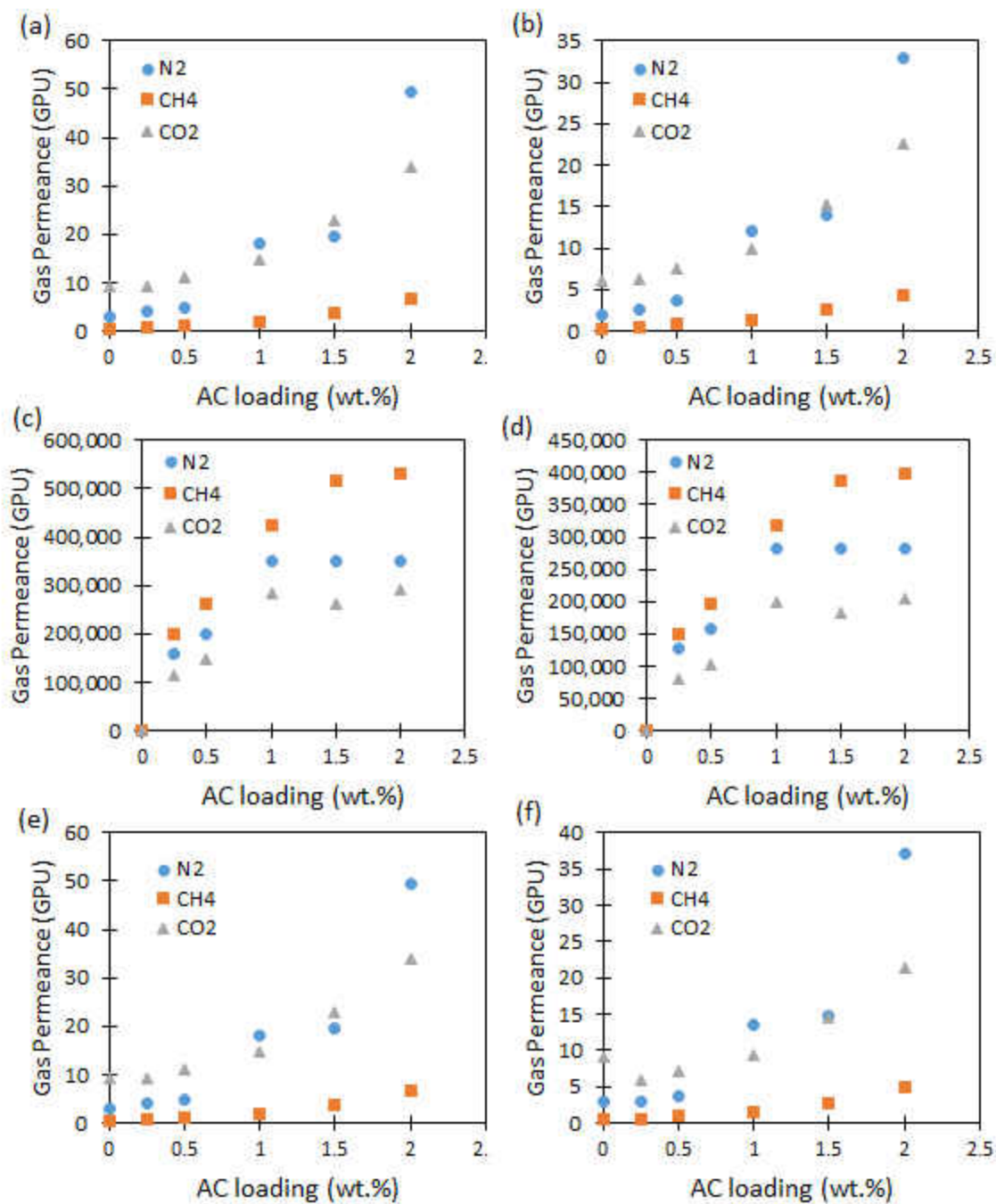
Figure 39: Gas permeation through (a) AC1-MMM, (b) AC1-annealed MMM, (c) AC2-MMM, (d) AC2 annealed MMM, (e) AC3-MMM, and (f) AC3 annealed MMM.

The permselectivity of each AC-MMM was calculated according to equation 2:

$$\alpha_{AB} = \frac{P_A}{P_B} \tag{2}$$

Although there was a significant increase in permeance with AC loading in all cases, the permselectivity tended to decrease until Knudsen selectivity was achieved. In the case of AC4, Knudsen selectivity was achieved immediately with dilute AC loading. These results are summarized shown in Figure 7.
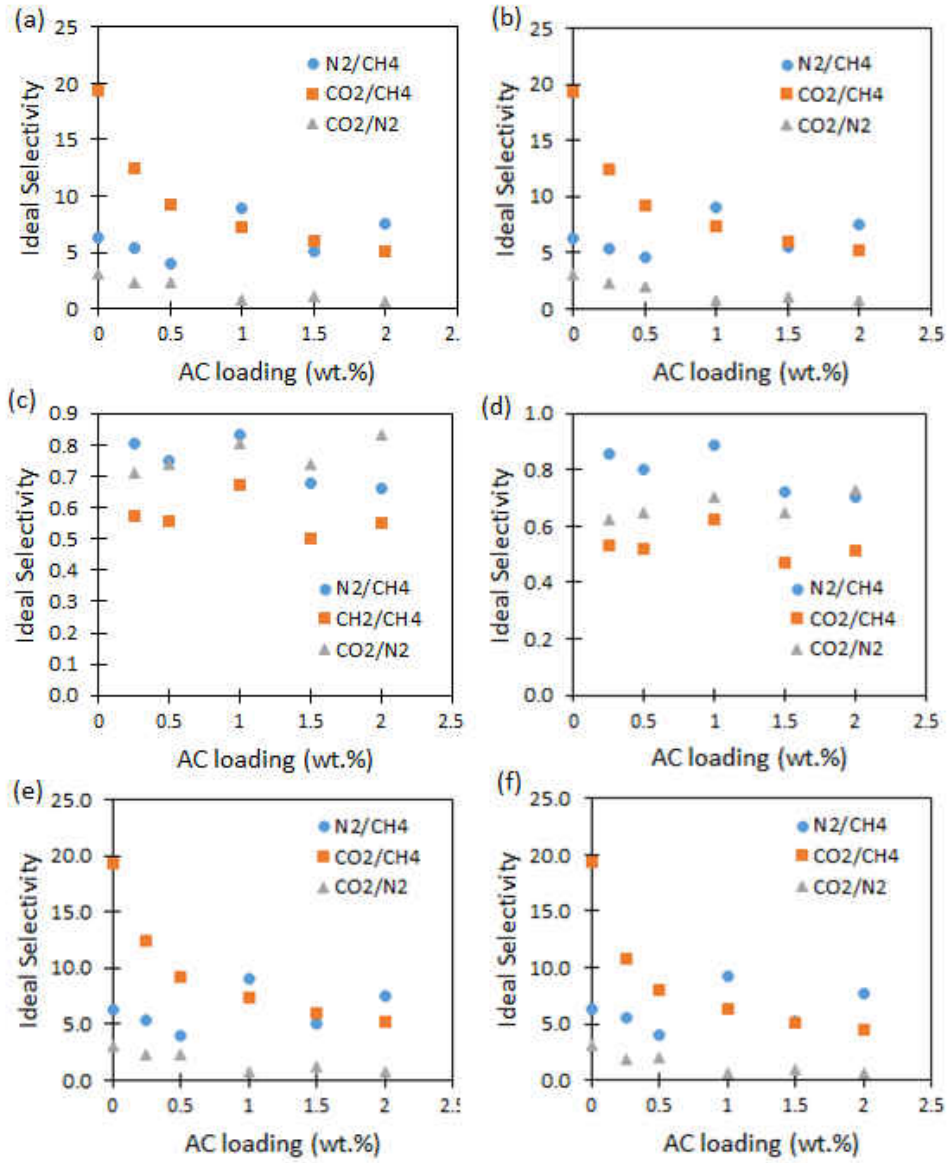
Figure 40: Ideal selectivities of each gas par for (a) AC1-MMMs, (b) AC1 annealed MMMs, (c) AC2-MMMs, (d) AC2 annealed MMMs, (e) AC3-MMMs, and (d) AC3 annealed MMMs.

4. Conclusion

In this we demonstrated the importance of functional groups on AC-MMMs. The presence of hydroxyl groups resulted in membranes with superior performance due to hydrogen bonding between AC and PSF. Interestingly, ether groups on the AC resulted in poor compatibility and sieve in a cage morphology. AC made with $ZnCl_2$ as the activating agent resulted in fewest oxide groups. This was expected to result in poorest performance, but performed quite well, meaning there was likely some competing interactions. We also showed that larger pores in the AC resulted in unselective MMMs. This was a result of micron sized pores which allowed for unselective gas diffusion. Further experimentation is needed to confirm the permeability and selectivity trends shown here, but it is quite evident that AC-PSF MMMs are highly influenced by the type of AC used.

APPENDIX A: PARTICLE SOLUBILITY STUDIES

The solubility of biochar was considered in solvent selection. As shown in the table, 2 mL of several solvents were placed in contact with 20 mg of biochar and mixed. The samples were either mixed and allowed to sit for 24 hours, or mixed and sonicated, then allowed to sit.

Table 15: Solubility of biochar in various solvents, without sonication.
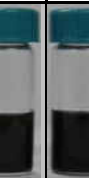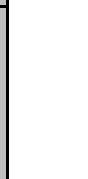
	Acetone	DCM	DEG	DMF	DMSO	EtOH	MeOH	NMP	THF	Tol.
Initial										
Char after 24 hrs										

Table 16: Solubility of biochar in various solvents after mixing and sonication.

	Acetone	DCM	DEG	DMF	DMSO	EtOH	MeOH	NMP	THF	Tol.
Initial										
Char after 24 hrs										

It is apparent there is some settling after time goes by with or without sonication. The brown shades above the sediment biochar are indicative of smaller particles remaining in solution. It is clear that DMF, DMSO, and NMP are the best candidate solvents. Sonication did improve the solubility for other solvents, but equally improved the three mentioned. Considering cost, DMF was chosen as the solvent for this study.

This study also allowed for a prediction of leaching behavior during the wet phase inversion process. The biochar is not highly soluble in ethanol, thus, leaching from the membrane into the ethanol nonsolvent is not likely to occur.

It is worth noting that acetone and toluene almost completely evaporated upon sonication. This is the reason those images are not present in the table

APPENDIX B: THERMOGRAVIMETRIC METHODS FOR CHARACTERIZING ACTIVATED CARBON

Abstract

The production, characterization, and application of activated carbon is of great interest in research and industrially. In this short review, we present thermogravimetric methods that have proven useful in studying activated carbon. Thermogravimetry is shown to be a tool in: predicting optimal charring and activating conditions, characterizing proximate analysis, thermal stability, surface area, pore volume, and gas sorption behavior. Comparisons to traditional methods and the advantages and limitations of the presented thermogravimetric methods are discussed where appropriate.

1. Introduction

Activated carbon (AC) is a porous, adsorptive material, that is made from carbonaceous precursors, and is used in applications such as water purification [1], catalysis [2, 3], and gas adsorption [4]. The general procedure to produce AC is as follows: thermal degradation of a precursor to produce a char then physical or chemical activation of the char at elevated temperatures. There are many important variables to this process. The precursor material is one of the most critical. In the early 1900s, popular precursors were wood dust. Later, coal and biomass feedstock such as coconut husks became industrially popular. Most recently, there has been research interest in using other biomass feedstock, mainly for economic advantages.

Another important factor is the charring conditions. Pyrolysis and gasification are the key processes that are utilized for char formation, and their influential factors include heating rate, residence time, and atmospheric conditions [5]. During the activation step, there are also a number of factors including activating agent used for chemical activation, impregnating ratio of activating agent to char, heating rate, residence time, and gas flow rate for physical activation.

Once produced, some characteristic properties are needed to compare ACs. Some of the main characteristics are surface area, pore volume, pore density, functionality, composition, thermal stability, adsorption characteristics, and morphology. The number of variables that can influence AC formation and properties, and the number of important properties, can make research and development of AC time consuming, expensive, and complicated by the required number of different instruments. However, one such technique that is underutilized in AC production is thermogravimetric analysis (TGA). While it is well understood that some properties, such as proximate analysis and thermal stability of AC can be investigated with TGA, various methods have been developed over time to cover much broader aspects of AC research and development, which are infrequently utilized. This review aims to describe how TGA can be utilized as a relatively fast and inexpensive method to investigate AC production conditions, select properties, and gas adsorption characteristics with minimal amounts of raw material requirements. The advantages and disadvantages of using TGA versus traditional techniques are also discussed.

2. Reaction Conditions

During AC formation, two key reaction processes are utilized. The pyrolysis of a precursor and the activation of the resulting char. In the case of pyrolysis, reactions taking place are due

to bond cleavage. During activation, activating agents can act as a catalyst to further promote bond cleavage of various functional groups, or react with the surface. There are two key reaction conditions that can be investigated using TGA: 1) conditions that pyrolysis or gasification occur in the charring stage, and 2) the activating temperature of the char into AC. Both conditions are represented well by TGA, but are most frequently studied on bench scale reactors, which use more material, and are more expensive to conduct.

2.1. Charring Conditions

The charring stage of AC production is the first step that can easily be studied using TGA. Pyrolysis is the thermal degradation in the absence of oxygen, and gasification is thermal degradation with controlled amounts of oxygen. Both processes are easily mimicked using either inert gases (i.e. N_2 and Ar) in the case of pyrolysis, or a combination of inert gases and oxygen in the case of gasification. Key variables that can be studied are heating rate and residence time, as both are well controlled with TGA instruments. Yield is one response variable that can be measured. Yield is an important factor that can dictate whether or not a particular feedstock is commercially viable. TGA records weight as a function of temperature and time, thus yield can be recognized quite readily.

Some key advantages of measuring yield in this fashion are, small sample sizes. Depending on the reactor type, the difference between large samples and small sample sizes can skew yield results due to uncharred material. Small sample sizes also prevent heat transfer limitations that are typically present in larger reactors [6]. Also, when using bench scale or large reactors, physically removing the char can cause error as well. Some charred material

will be unaccounted for due to being left in the reactor, or being lost in transition from reactor to measuring device.

There is one disadvantage of using TGA to study yield. That is, pyrolysis and gasification often produce tars as a by-product. In standard reactors, this tar can either be continuously removed, or separated after reactions are complete. In TGA, tars are unable to escape sample crucibles, and thus, the char yield in TGA may include yield of tar as well. However, considering tar remains in the crucible, it also may thermally degrade, or even evaporate, soon after it is produced, minimizing its influence on char yield.

2.2. Activation Temperature

The chemical activation of char can also be studied to find the optimal activation temperature and heating rate. In the case of chemical activation, after char is impregnated with desired amounts of an activating agent, it is subjected to high temperatures in an inert atmosphere. Two or three characteristic degradation steps are likely to occur depending on the activating agent, one at a significantly lower temperature than the other two. The low temperature degradation is likely moisture loses from residue water from impregnation. The other degradations can be from evaporation of activating agent, or from reactions between activating agent and char (activation). If activating agents are carefully chosen, the evaporation curve may not be present. This leave only mass change due to chemical activation. The temperature at which the TGA curve levels indicates complete activation. Tsai et al. have shown that this temperature is the optimal activation temperature [7], yielding optimal properties. This is shown in figure 41. Thus, this experiment can, at the least, greatly narrow the number of activating temperatures investigated, as most researchers choose to investigate several temperatures, seemingly without evidence of a particular range. Similar analysis can be

conducted for the case of physical activation. In this case, reactive gases such as water vapor or carbon dioxide are fed into TGA rather than inert gases.
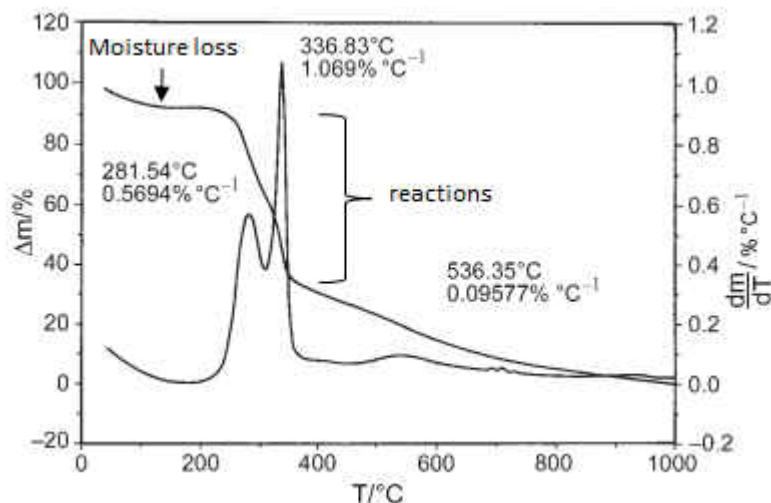
Figure 41: TGA and DTG curves depicting the chemical activation of corn cob impregnated with ZnCl2. The optimal activating temperature was concluded to be 400°C, the point where the major mass loss concluded. Adopted from [7] and reprinted with permission from Springer.

While this analysis can narrow the temperature range chosen to study, it will likely not give the exact optimal activating temperature in real systems. In real reactors, heat and mass transfer become limiting conditions, as reactions between activating agent and char can vary down the length or radius of a reactor.

3. Characterization

Once AC is made, it is commonly characterized by various methods. There are five characteristics described here in which TGA would be most suitable to use; namely, proximate analysis, thermal stability, surface area, pore volume, and gas adsorption/desorption. Some of these characteristics are common in research and are frequently utilized, while others are not.

3.1. Proximate Analysis

Proximate analysis is the determination of moisture, volatiles, ash, and fixed carbon of a sample. This method is frequently, nearly exclusively, studied using TGA [8, 9]. First, a sample

132

is heated at a predetermined rate in an inert atmosphere, from room temperature to high temperatures (typically 900-1100°C). Two properties are determined from this curve. The weight loss between room temperature and 105°C is commonly attributed to moisture, and thus is the moisture content of the AC. The weight loss between 105°C and the temperature in which the TGA curve levels (or usually the final weight), is the volatile content of the AC. Next, a reactive gas is used to measure the ash content. A sample is either immediately exposed to oxygen after 900°C, or a new sample is subject to heat from room temperature to high temperatures in the presence of oxygen. The remaining weight after the TGA curve levels in this case, is known as the ash content, which consists incombustible compounds like metals. The fixed carbon content is taken as the difference between the moisture, volatile, and ash content from unity and is highly stable, aromatic networks. This process is represented schematically in figure 42.
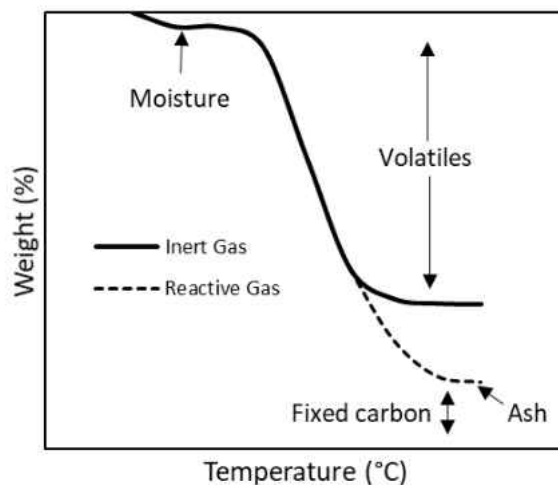
Figure 42: Proximate analysis schematic showing the region on the TGA curve in which each component is taken.

3.2. Thermal Stability

The other property almost exclusively studied by TGA is the thermal stability of the AC [10-12]. The thermal stability is defined as the temperature at which major degradation occurs. It

133

is often taken as the inflection point on the TGA curve, or the peak of the differential curve (DTG). It is sometimes appropriate to report the initial and final temperature where major degradation occurs. Similar to pyrolysis, most of this degradation is caused by cleavage of loosely bonded oxygenated functional groups and single bonded carbon chains. The higher temperatures provide more energy to break double and triple bonded functional groups, leaving behind highly stable aromatics.

In the case of AC, depending on the intended application, a number of gaseous environments can be chosen. In most instances, the AC is subject to inert atmospheres at a predetermined heating rate. The thermal stability in reactive conditions can be investigated by using a reactive gas such as air, or even harsher gases like hydrogen sulfide [13], sulfur dioxide, and nitrous oxides [14]. The thermal degradation property is depicted in figure 43. In the case of reporting the inflection point as the degradation temperature, the DTG curve is often useful, as its peak is at the inflection point of the TGA curve.
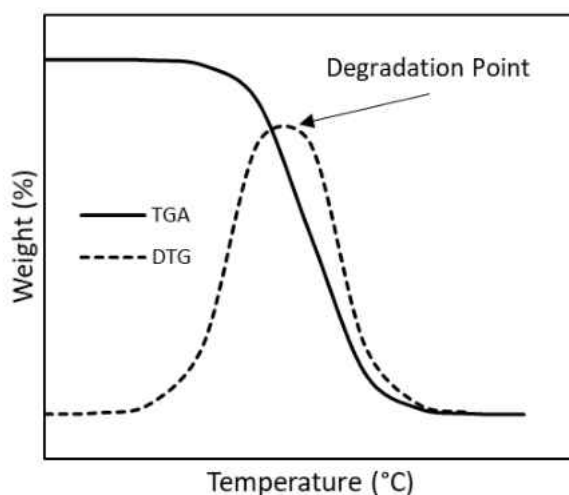
Figure 43: TGA/DTG curves depicting the thermal degradation point.

3.3. Surface Area

Specific surface area of AC is one of the most important characteristics reported. Some methods to determine surface area include BET analysis. In this case, Argon or N_2 adsorption isotherms are taken at 77 K then analyzed according to BET theory, to determine the so called BET surface area. In this case, degassing occurs for 24 hours. While this is the most widely used and accepted method, it is time consuming and the analysis is non-trivial. Another fairly common and accepted method to measure surface area is through the so called Iodine number [15]. In this case, an iodine solution of known concentration is allowed contact time with a predetermined amount of AC. The residual is then filtered and the concentration of the filtrate is determined by an end point titration with sodium thiosulfate. The iodine number is defined as the amount of iodine adsorbed per gram of AC when the residual concentration is 0.02N. Commercially, this is a common identifier of AC. In research, attempts have been made to correlate the iodine number to BET surface area [16, 17]. Although an acceptable method to report surface area, the iodine number test involves a minimum of three titrations per sample and several chemical solutions, making it a very consuming test in terms of supplies and time.

A TGA method was developed by Pan et al in 1996 [18]. Both BET surface area and pore volume were determined by this method. To perform this test, about 20mg of AC is heated by TGA to 200°C under N_2 to degas. Once cooled to room temperature and allowed to equilibrate, either butanol or heptane is added to completely wet the AC. Butanol is chosen for polar (hydrophilic) AC, and heptane is chosen for nonpolar (hydrophobic) AC. The AC immersed in solution is then heated to 300°C at a rate of 5°C/min. Un-adsorbed butanol/heptane quickly evaporate, resulting in a steep weight loss curve with respect to time. It was hypothesized that the remaining liquid remains trapped within the pores of the AC, thus

as temperature is increased, the butanol/heptane more slowly evaporate from the pores until the TGA curve levels off. The amount of solution that escaped from the pores is visually clear from DTG curves of the first and second derivative, as was later suggested by Mercuri et al [19]. The values from these points shown in figure 44 are used to calculate the surface area based on empirical correlations using butanol or heptane:

Butanol: $$S_A = 2.64 * 10^5 * a_{sa} + 77.6 \qquad (1)$$

Heptane: $$S_A = 3.85 * 10^5 * a_{sa} + 57.7 \qquad (2)$$

$$a_{sa} = \frac{M - R}{R * M_w} \qquad (3)$$
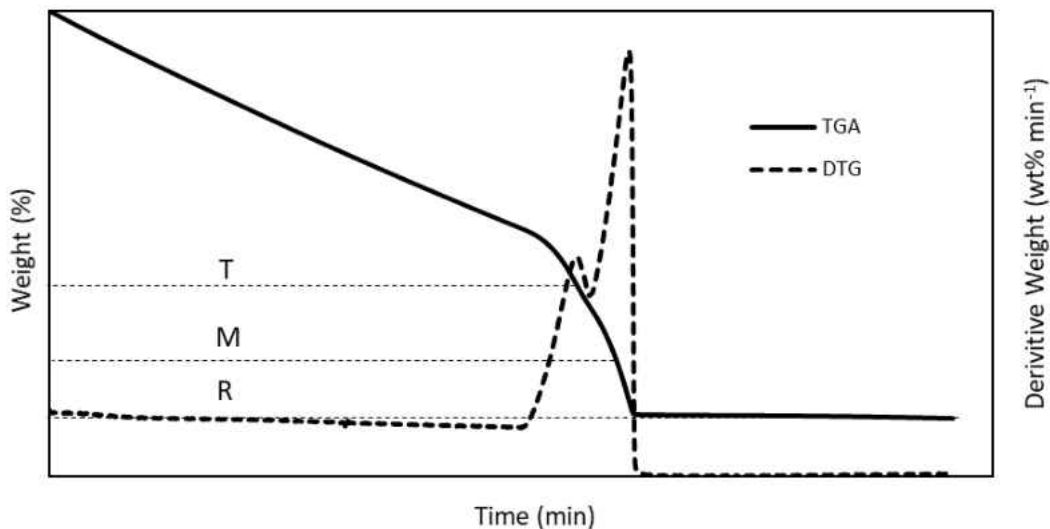
Figure 44: TGA/DTG curves representing liquid adsorption/desorption and key points in calculating specific surface area or pore volume.

This method has shown to yield surface area results exceptionally similar to AC containing mostly mesopores [20-22]. However, this method may find limitation to micro porous AC as neither butanol nor heptane can penetrate those pores completely. It is also limiting to AC with significant pore volume. In the case of low pore volume, the peak of the

136

1st and second derivative become indistinguishable due to the amount of desorbed solution being very small.

3.4. Pore Volume

The average pore volume is another AC characteristic that provides meaningful information. As described earlier, BET analysis can also be used to determine pore volume. Another method used to measure pore volume is porometry, which is performed with a porometer. While a number of types of porometry exist [23], they all essentially follow the same principle that an amount of desorbed gas or liquid from the pores of the AC can be used to determine pore size, then converted to a volume.

The TGA method described earlier for surface area [18] can also be used to estimate pore volume. In this case, the same procedure is applied. However, a different correlation was made to correspond with pore volume obtained from BET analysis. Thus, a different empirical equation is applied to the same data to obtain the pore volume with this method. The empirical correlations were determined to be:

Butanol: $$V_p = 102.8 * a_{vp} + 0.0826 \tag{4}$$

Heptane: $$V_p = 154 * a_{vp} + 0.0557 \tag{5}$$

$$a_{vp} = \frac{T - R}{R * M_w} \tag{6}$$

3.5. Surface Functionality

While heptane and butanol desorption have been correlated to surface area and pore volume, the desorption isotherms of other compounds can give insight into the surface functionality.

137

This is a result of intermolecular bonding between the surface functional groups on the AC and the adsorbate. Polar bonds in AC will bond strongly with polar adsorbates and highly non polar functional groups will bond strongly to nonpolar adsorbates. This was clearly demonstrated by Pan and Jaroniec [24], where surface modified AC showed unique desorption isotherms for various adsorbates. Liquids adsorbents of various polarity such as butanol, water, and other hydrocarbons are adequate for this analysis because they can completely wet the AC and differences in desorption will be apparent. However, some studies have gained insight into surface functionality by investigating the desorption of particulates such as mercury [25] and ammonium nitrate prills [26].

3.6. Gas Adsorption/Desorption

One major application of AC is adsorption of gases. In most cases, the equilibrium amount adsorbed is of interest and reported as an isotherm. The kinetics of adsorption are also sometimes sought, making transient analysis necessary.

Gas adsorption can be studied using bench scale packed columns. In this method, measurements of flow rates of gas into the column, pressure drop, and flow rates exiting the column are required for meaningful data. The more common method is with lab scale gas sorption analyzers. Essentially, a gas is put in contact with AC and weighed to find the amount adsorbed. This technique is beneficial because it can easily measure equilibrium adsorption at varying pressures, thus obtaining an isotherm. While the complete isotherm cannot be obtained using TGA due to invariable pressure restrictions, the adsorption kinetics can be investigated. Through a process called isothermal-thermal analysis, the amount of gas adsorbed versus time at specified temperatures is easily measured. With isothermal-thermal analysis by TGA, it is

important the sample be initially heated under N_2 to remove moisture and other physically adsorbed species. Once cooled or taken to the desired temperature, the gas of interested is introduced at a predetermined flow rate and is adsorbed onto the AC, and mass recorded versus time. The general procedure is represented in Figure 45. This method has proved to be beneficial in studying the adsorption kinetic parameters of CO_2 on resin based [27] and agro based [28-30] AC.
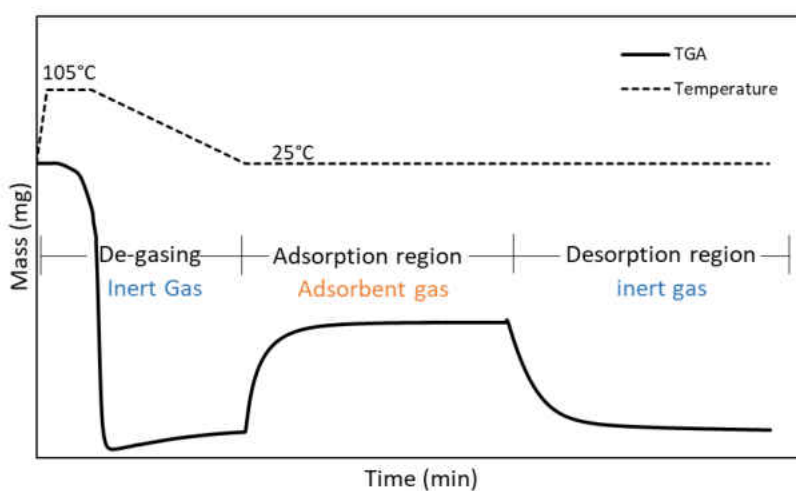
Figure 45: Schematic procedure for measuring gas adsorption by TGA. Rate of adsorption can be investigated in the adsorption and desorption regions. The temperature influence can also be investigated by setting any temperature in that region.

4. Conclusions

The thermogravimetric methods used to study AC are presented. The methods offer cost and time effective alternatives to traditional methods. We have shown that TGA can effectively be used to study the entire process of AC production from charring conditions to activating temperature. Methods to quantify several AC characteristics are presented and include proximate analysis, thermal stability, specific surface area, and pore volume. A method for the application of AC for gas sorption was also presented and can be useful in studying sorption kinetics. The methods shown are compared to traditional methods where appropriate, in which the advantages and limitations of each were discussed. The use of TGA can be an effective tool in AC research and development.

APPENDIX C: TOP VIEW SESSILE DROP METHOD FOR MEASURING CONTACT ANGLES

Abstract

The water contact angle on a materials surface is an important characteristic giving insight into that materials wettability. Methods to perform this measurement are often difficult or involve expensive equipment. In this paper we present and validate a top view imaging method using a cell phone camera.

1. Introduction

Contact angle measurements are widely used, across multiple disciplines, as a quantitative measure of a material's surface wettability. This is an important characteristic for understanding wetting phenomena in applications including membrane separation[1], coatings [2], printing [3], and adhesives [4] to name a few. Due to the widespread interest in measuring the contact angle, many methods have been developed to do so. Of the most popular are sessile drop goniometry, captive bubble, tilting plate, Wilhelmy balance, and capillary rise methods [5]. Various more advanced techniques have also been developed for specific applications. For example, Forward et al. developed an optical microscopy method to measure the contact angle on microparticles [6]. Nuriel et al. developed an imaging technique to measure the contact angle of carbon nanofibers [7]. Other novel methods utilized classic imaging techniques but focused on the surrounding conditions [8].

While precise and accurate, each of these methods possess some negative features. Most notably, imaging methods require costly imaging devices, such as optical or scanning electron microscopes. Non imaging methods, such as the capillary rise method, require knowledge of the liquid-gas surface tension, which is not always easy to gather.

Despite this, sessile drop goniometry is the most widely used method, owning to its accuracy, simplicity, and the abundance of software available for drop analysis. To make this method more cost effective, Costa et al. recently presented a method in which the angle was calculated based on a spherical cap geometry [9]. Rather than processing a goniometric side view image, the image of the drop was taken from the top view. The drop diameter was the measured variable, and the contact angle was calculated based on this diameter. This method was shown to reasonably measure water contact angles on calcite crystals.

In this work, we expand further on this method and introduce a simple smartphone camera rather than an optical microscope, for imaging. We utilized a statistical experimental design to screen three important variables for their potential impact on measurements. Importantly we compared contact angle results from this method to the traditional goniometric method, for a variety of materials, in order to present confidence in the method.

2. Experimental Section

2.1. Materials

To assess the top view-spherical cap method for a variety of material types, several materials were tested. These consisted of various polymers, metals, ceramics, and glasses. It is important to note, that highly rough and porous materials were intentionally not utilized due to the impracticality of the sessile drop method on these surfaces [10,11]. All surfaces were cleaned

with either acetone or water, and allowed to dry before testing. A Samsung Galaxy S9 smartphone was used for imaging the surface. Methyl blue was purchased from Sigma Aldrich and was dissolved with distilled water for a 1 wt.% dye solution.

2.2. Goniometric measurements

Side view measurements were taken for comparison purposes using an in-house built goniometer. The set up consisted of a syringe, level stage, a light, and a microscope camera. Images were analyzed using ImageJ editing software [12]. The angles reported are the average of the angle observed from both edges of at least two drops.

2.3. Top view imaging set-up

The phone camera was mounted to a ring stand and held perpendicular to the surface of the material being tested. This is shown schematically in Figure 46a. The zoom was set to 8x and was held constant throughout. A measured volume of either distilled water or 5 wt.% dye was pipetted onto the surface where a bead formed. Both the drop and a reference scale bar were imaged. The diameter of the drop was measured using ImageJ. Considering the geometry of the drop is the most important parameter, drops with irregular shapes (non-spherical), were preliminarily discarded. The average diameter was taken from two axes and was used for calculations. The contact angles reported are the average from at least three measurements. An example of an irregular and regular shaped drop is depicted in Figure 46b and 1c.
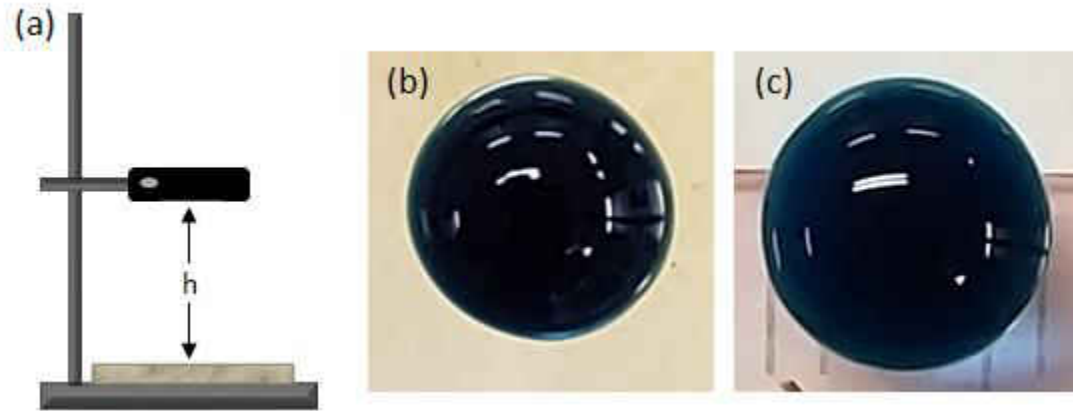
Figure 46: (a) experimental set-up and an example of (b) an irregular shaped drop and (c) a regular shaped drop.

A replicated 2^3 full factorial statistical design was used to screen and quantify the effects of three factors in this set up: the distance between the surface and camera, drop volume, and presence of methyl blue dye. This analysis was performed using Minitab 18 according to established statistical methods [13].

2.4. Contact angle calculations

The water drop was estimated as a spherical cap shown in Figure 47 [14]. A series of calculations were performed to calculate the contact angle.
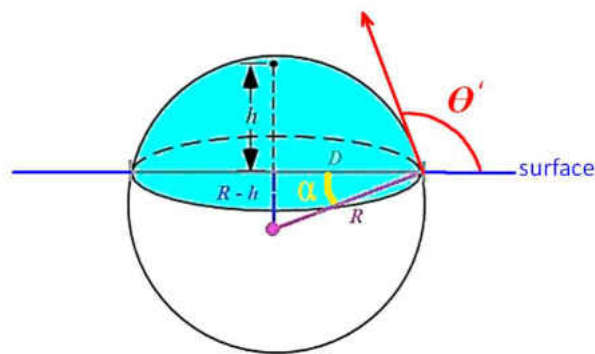
Figure 47: Spherical cap geometry

The diameter, D, of the drop is readily measured when imaged from the top view. The radius and known volume are then used to calculate the cap height according to equation 1.

$$\pi h^3 + 3\pi r^2 h - 6V = 0 \tag{1}$$

In this case, care must be taken to ensure unit consistency. All lengths (r and h) are in units of μm and the volume in terms of $μm^3$. The calculation of h can be performed using any numerical technique. Then the radius of curvature, R, is calculated with equation 2.

$$R = \frac{r^2 + h^2}{2h} \tag{2}$$

The angle between the center of the projected sphere and the bottom of the cap, α, is then calculated according to equation 3. The outer contact angle θ', and the inner contact angle traditionally reported, θ, are easily calculated with equations 4 and 5. All angles are calculated in units of radians.

$$\alpha = \sin^{-1}\left[\frac{R - h}{R}\right] \tag{3}$$

$$\theta' = \alpha + \frac{\pi}{2} \tag{4}$$

$$\theta = \pi - \theta' \tag{5}$$

3. Results and Discussion

3.1. 2^3 full factorial design on method parameters

Like any other imaging technique, picture resolution is one of the most important aspects. surface being tested is also an important factor. For this reason, we chose the distance between camera and surface as an important variable related to image resolution. This relationship is depicted in Figure 48, where the further the camera is from the surface, the lower the image resolution.
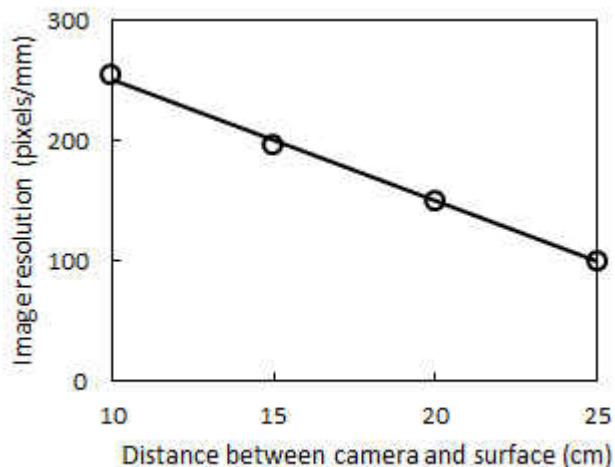
Figure 48: Image resolution as a function of distance between the camera and surface.

To better visualize the edges of sessile drops, we investigated using a 5 wt.% methyl blue dye and compared it to using distilled water. Drop size is another factor that greatly contributes to accuracy. Larger drops cover a greater surface area, and can become more unstable as a result of this. Smaller drops on the other can be too sensitive to defects in the material. For this reason, two drop sizes were investigated, 20 µL and 80µL. For simplicity, all experiments in the factorial design were performed on acrylic glass due to its smooth surface and homogeneity. The randomized factorial design and raw data are shown in table 17.

A 95% confidence level was used for calculation. The coded factors are shown as dye/no dye (A), height (B), and drop size (C). The results in Figure 49 indicate that the three variables studied do not have significant effects on the contact angle measurement. This is concluded by the standard effects well below the 95% confidence level. The interaction plots in figure 4(d) reveal no significant interactions. However, it is worth noting that the interaction effects between dye*height, and height*drop size were substantially greater than dye*drop size. This indicates the loss in resolution and difficulty in differentiating the drop edges are the main contributors to error in measurements. This analysis also yields the approximate deviation

in the measurements. The averages between replicates are all between about 65° and 70°, so it is concluded the error of measurement is about ±2.5°. This is based on inaccuracies solely from setting up the apparatus and dispensing the drop, not from difficulties in sample preparation. It is important to note that the contact angle calculated here is reasonably the same as that reported elsewhere [15]. This result allows for choosing any of the factor levels studied for further investigation. For convenience and ease in analyzing the drops, we chose to use water with dye, at a height of 10 cm above the sample, and a 20 µL drop size.

Table 17: Randomized two level factorial design with three factors and two replicates at each corner point.

Standard Order	Run Order	Factors			Response
		dye	height (cm)	drop size (µL)	contact angle (°)
13	1	No dye	10	80	70.80
16	2	dye	20	80	67.78
10	3	dye	10	20	69.67
9	4	No dye	10	20	69.67
12	5	dye	20	20	66.77
2	6	dye	10	20	64.59
3	7	No dye	20	20	66.21
5	8	No dye	10	80	68.70
11	9	No dye	20	20	78.34
1	10	No dye	10	20	75.26
15	11	No dye	20	80	71.90
6	12	dye	10	80	65.34
4	13	dye	20	20	71.04
7	14	No dye	20	80	67.80
14	15	dye	10	80	61.02
8	16	dye	20	80	67.21
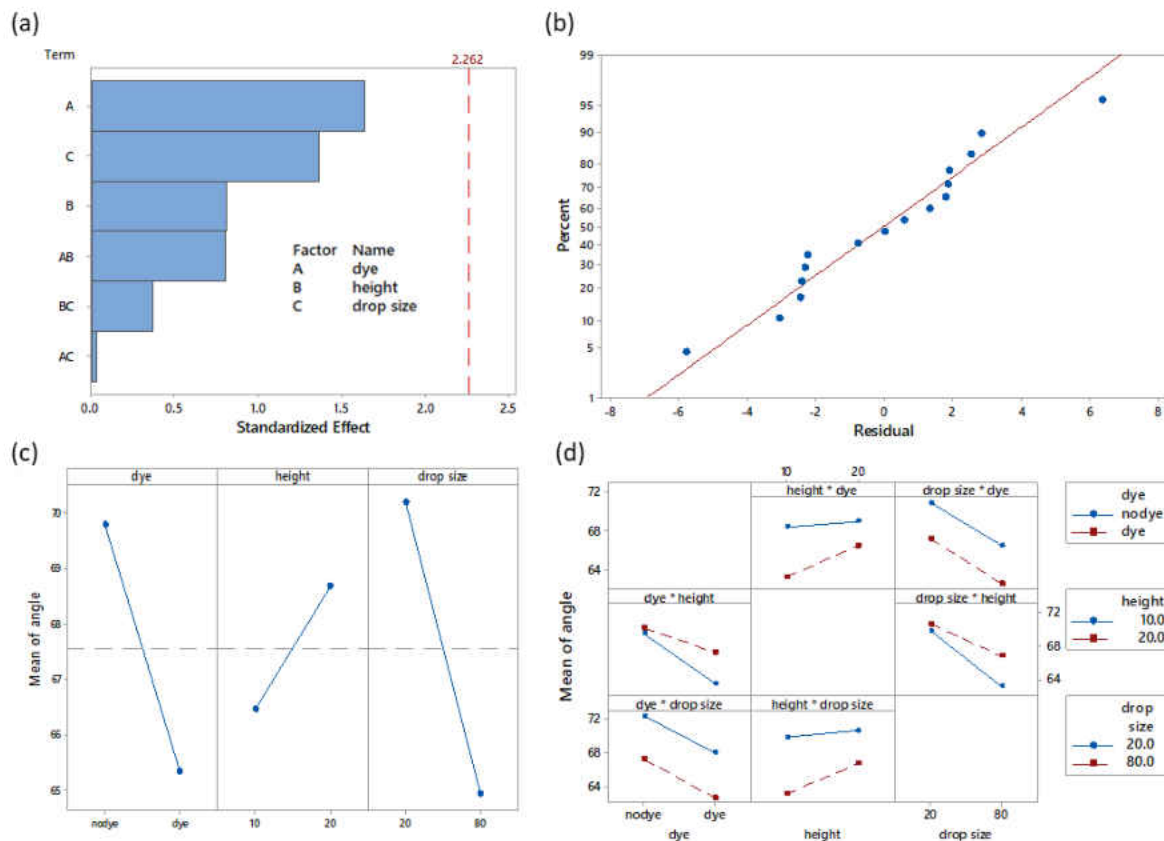
Figure 49: (a) Pareto diagram showing the standardized main effects and two level interaction effects. (b) Normal plot of the data showing normality. (c) main effect and (d) interaction plots.

3.2. Side view/top view comparison

A variety of seventeen materials were investigated. The contact angles measured by the top view and side view methods are shown in Table 18. It is difficult to compare the contact angle measurements from this work to other studies because sample preparation can greatly influence the measurements. None the less, a range of values are reported here based on those found in the literature. From this table, it is apparent the contact angles measured in this study correlate reasonably well with those found in the literature. The one exception is in the Parafilm® sample, where the difference between this study and literature is at least 10°. This is likely because the sample used in this study was commercially available Parafilm®. Since the contact

angle of this particular material is not readily available in the literature, another paraffin based material was used for comparison. The chemical makeup of each is likely different.

Table 18: Contact angles measured for each material by the top view and side view compared to literature values.

Material	Contact Angle (°)			Ref
	Top view	Side View	Literature	
Aluminum	87.43	79.61	75	[16]
Duran® Glass Plate	24.25	35.46	-	-
Millipore parchmentized paper	82.73	100.65	-	-
Ceramic tile	43.76	44.77	35-45	[17]
Graphene-oxide membrane	50.94	53.15	45-60	[18]
Holey graphene-oxide membrane	47.40	49.53		
Parafilm®	94.46	92.40	108-114	[19]
Isopore™ membrane filter	59.03	59.91	49.9	[20]
Clear polystyrene	80.14	82.60	80-86	[21]
Opaque polystyrene	79.10	71.35	83	[22]
Pyrex	71.44	80.76	40-80	[23]
Silicon	104.05	104.02	90-120	[24]
Stainless steel	71.34	71.29	70-75	[25]
Teflon	98.34	98.82	90-110	[23]
Polyvinyl chloride	64.01	53.09	60-87	[26,27]
Acrylic glass	67.13	65.17	63-80	[15]
Polysulfone	70.15	68.43	72-90	[28]

Most notable is the comparison between the top view and side view measurements. This is shown graphically in figure 50. The reference line y=x represents the same angle calculated from each method. Thus, points close to the reference line indicate compatibility between the top view and side view. Based on a correlation coefficient of 0.887 compared to

the reference line, the top view method matches reasonably well with the traditional side view method for the materials tested.

It is worth noting that, it was anticipated contact angles greater than 90° would not be distinguishable from those close to 90°. This was expected because the projected area of a sessile drop would mask the spherical cap diameter. However, four samples had contact angles between 90° and 105°. These were also reasonably measured with the top view method, indicating the shadowing effect of the projected area was not a major hindrance. However, it is still expected that highly hydrophobic materials still cannot be measured by top view images.

It is apparent that the error encountered within samples had a more significant effect on measurements than errors in setting up the apparatus. Only the error associated with the top view is shown, however the error associated with side view measurements were typically ±5° within a particular sample. The error within samples is fairly common in imaging methods, which is mainly attributed to inhomogeneity in the surface caused by surface defects, rough patches, scratches, and particulate contamination. None the less, the error within samples was typically less than ±8° except in slightly rough samples where inhomogeneity is suspect.
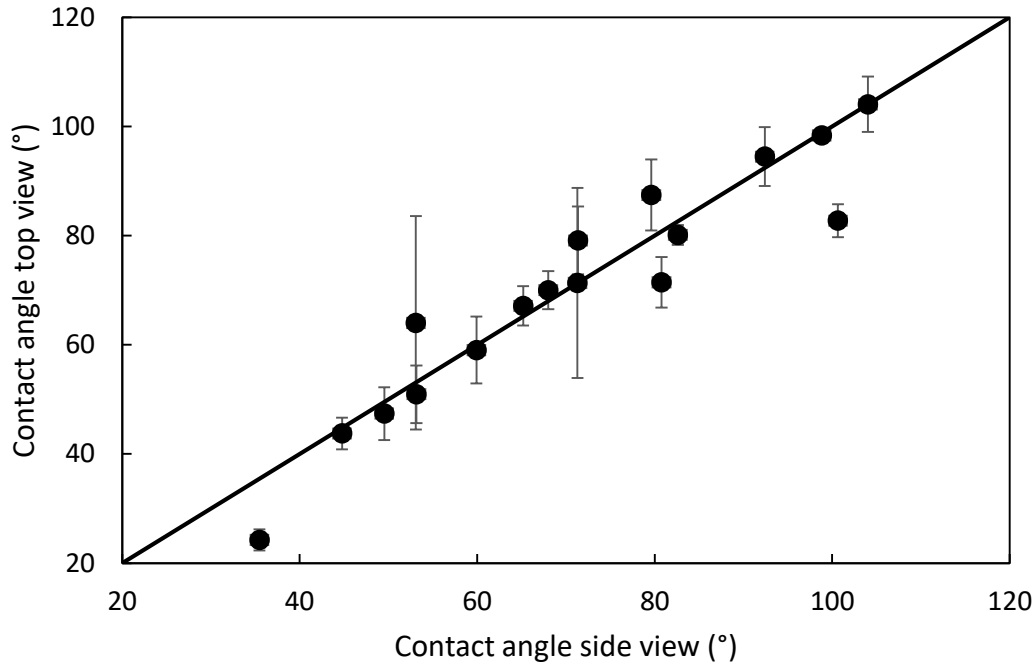
Figure 50: Comparison between the top view and side view methods with the y=x reference line representing an exact match between the two methods. R2 values is 0.887.

4. Conclusions

In this paper we validate a simple top view goniometric method for measuring the water contact angle of various materials. A phone camera was used to image water drops, and the contact angle was calculated based on a spherical cap geometry. The appropriate experimental set up was chosen based on a 2^3 factorial design investigating three factors: dye/no dye in water used to make drops, height between the camera and stage, and drop size. Contact angles using the top view method were reasonably similar to those of traditional side view methods. Thus, the top view method using a simple phone camera is an acceptable method for measuring water contact angles.

REFERENCES
CHAPTER I

1. Lewis, J., Al-sayaghi, M., Buelke, C., Alshami, A. (2019) Activated carbon in mixed-matrix membranes. *Separation and Purification Reviews*. doi: 10.1080/15422119.2019.1609986

CHAPTER II

1. Paul, D. R. and Kemp,D. R. (1973) The Difussion Time Lag in Polymer Membranes Containing Adsorptive Fillers. *J. Polym. Sci. Polym. Symp.,* 41:79-93.

2. Drioli, E. and Giorno, L. (2016) *Encyclopedia of Membranes.* Springer: Verlag Berlin Heidelberg.

3. Baghbanzadeh, M., Rana, D., Lan, C.Q., and Matsuura, T. (2016) Effects of Inorganic Nano-Additives on Properties and Performance of Polymeric Membranes in Water Treatment. *Sep. Purif. Rev.,* 45: 141-167. doi:10.1080/15422119.2015.1068806

4. Villalobos-Rodríguez, R., Montero-Cabrera, M.E., Esparza-Ponce, H.E., Herrera-Peraza, E.F., and Ballinas-Casarrubias, M.L. (2012) Uranium Removal from Water using Cellulose Triacetate Membranes Added with Activated Carbon. *Appl. Radiat. Isot.,* 70: 872-881. doi:10.1016/j.apradiso.2012.01.017

5. Nejad, M.N., Asghari, M., and Afsari, M. (2016) Investigation of Carbon Nanotubes in Mixed Matrix Membranes for Gas Separation: A Review. *ChemBioEng Rev.,* 3: 276-298. doi:10.1002/cben.201600012

6. Dechnik, J., Sumby, C.J., and Janiak, C. (2017) Enhancing Mixed-Matrix Membrane Performance with Metal–Organic Framework Additives. *Cryst. Growth Des.,* 17: 4467-4488. doi:10.1021/acs.cgd.7b00595

7. Vu, D.Q., Koros, W.J. and Miller, S.J. (2003) Mixed Matrix Membranes using Carbon Molecular Sieves: I. Preparation and Experimental Results. *J. Membr. Sci.,* 211: 311-334. doi:10.1016/S0376-7388(02)00429-5

8. Vu, D.Q., Koros, W.J. and Miller, S.J. (2003) Mixed Matrix Membranes using Carbon Molecular Sieves: II. Modeling Permeation Behavior. *J. Membr. Sci.,* 211: 335-348. doi:10.1016/S0376-7388(02)00425-8

9. Muntha, S.T., Kausar, A., and Siddiq, M. (2016) A Review on Zeolite-Reinforced Polymeric Membranes: Salient Features and Applications. *Polym. Plast. Technol. Eng.,* 55: 1971-1987. doi:10.1080/03602559.2016.1185631

10. Weigelt, F., Georgopanos, P., Shishatskiy, S., Filiz, V., Brinkmann, T., and Abetz, V. (2018) Development and Characterization of Defect-Free Matrimid Mixed-Matrix Membranes Containing Activated Carbon Particles for Gas Separation. *Polymers,* 10:1-21. doi:10.3390/polym10010051

11. Tessema, T.D.M., Venna, S.R., Dahe, G., Hopkinson, D.P., El-Kaderi, H.M., and Sekizkardes, A.K. (2018) Incorporation of Benzimidazole Linked Polymers into Matrimid to Yield Mixed Matrix Membranes with Enhanced CO 2 /N 2 Selectivity. *J. Membr. Sci.,* 554: 90-96. doi:10.1016/j.memsci.2018.02.054

12. Rezaee, R., Nasseri, S., Mahvi, A.H., Nabizadeh, R., Mousavi, S.A., Rashidi, A., Jafari, A., and Nazmara, S. (2015) Fabrication and Characterization of a Polysulfone-Graphene Oxide Nanocomposite Membrane for Arsenate Rejection from Water. *J. Environ. Health Sci. Eng.,* 13:61. doi:10.1186/s40201-015-0217-813. Mukherjee, R., and De, S. (2016) Novel Carbon-Nanoparticle Polysulfone Hollow Fiber Mixed Matrix Ultrafiltration Membrane: Adsorptive Removal of Benzene, Phenol and Toluene from Aqueous Solution. *Sep. Purif. Technol.,* 157: 229-240. doi:10.1016/j.seppur.2015.11.015

14. Anadão, P., Sato, L.F., Wiebeck, H., and Valenzuela-Díaz, F.R. (2010) Polysulfone Activated Carbon Composite Membranes. *Mater. Sci. Forum,* 660-661: 1081-1086. doi:10.4028/www.scientific.net/MSF.660-661.1081

15. Anson, M., Marchese, J., Garis, E., Ochoa, N., and Pagliero, C. (2004) ABS Copolymer-Activated Carbon Mixed Matrix Membranes for CO2/CH4 Separation. *J. Membr. Sci.,* 243: 19-28. doi:10.1016/j.memsci.2004.05.008

16. Fu, X., Maruyama, T., Sotani, T., and Matsuyama, H. (2008) Effect of Surface Morphology on Membrane Fouling by Humic Acid with the use of Cellulose Acetate Butyrate Hollow Fiber Membranes. *J. Membr. Sci.,* 320: 483-491. doi:10.1016/j.memsci.2008.04.027

17. Aroon, M. A., Ismail, A.F., Matsuura, T. and Montazer-Rahmati, M.M. (2010) Performance Studies of Mixed Matrix Membranes for Gas Separation: A Review. *Sep. Purif. Technol.,* 75: 229-242. doi:10.1016/j.seppur.2010.08.023

18. Goh, P.S., Ismail, A.F., Sanip, S.M., Ng, B.C., and Aziz, M. (2011) Recent Advances of Inorganic Fillers in Mixed Matrix Membrane for Gas Separation. *Sep.Purif. Technol.,* 81: 243-264. doi:10.1016/j.seppur.2011.07.042

19. Chung, T., Jiang, L.Y., Li, Y., and Kulprathipanja, S. (2007) Mixed Matrix Membranes (MMMs) Comprising Organic Polymers with Dispersed Inorganic Fillers for Gas Separation. *Prog. Polym. Sci.,* 32: 483-507. doi:10.1016/j.progpolymsci.2007.01.008

20. Rezakazemi, M., Amooghin, A.E., Montazer-Rahmati, M.M., Ismail, A.F., and Matsuura, T. (2014) State-of-the-Art Membrane Based CO.Sub.2 Separation using Mixed Matrix Membranes : An Overview on Current Status and Future Directions. *Prog. Polym. Sci.,* 39: 817. doi:10.1016/j.progpolymsci.2014.01.003

21. Vinoba, M., Bhagiyalakshmi,M., Alqaheem,Y., Alomair,A. A., Pérez,A. and Rana,M. S. (2017) Recent Progress of Fillers in Mixed Matrix Membranes for CO2 Separation: A Review. *Sep. Purif. Technol.,* 188: 431-450. doi:10.1016/j.seppur.2017.07.051

22. Goh. P.S., Ng B.C., Lau, W.J. and Ismail, A.F. (2014) Inorganic Nanomaterials in Polymeric Ultrafiltration Membranes for Water Treatment. *Sep. Purif. Rev.,* 44: 216-249. doi:10.1080/15422119.2014.926274

23. Qadir D., Mukhtar, H., and Keong L.K. (2016) Mixed Matrix Membranes for Water Purification Applications. *Sep. Purif. Rev.,* 46: 62-80. doi:10.1080/15422119.2016.1196460

24. Bastani, D., Esmaeili, N., and Asadollahi, M. (2013) Polymeric Mixed Matrix Membranes Containing Zeolites as a Filler for Gas Separation Applications: A Review. *J. Ind. Eng. Chem.,* 19: 375-393. doi:10.1016/j.jiec.2012.09.019

25. Lakhotia, S. R., Mukhopadhyay, M., and Kumari, P. (2017) Surface-Modified Nanocomposite Membranes. *Sep. Purif. Rev.,* 47: 288-305. doi:10.1080/15422119.2017.1386681

26. Liu, M., Gurr, P.A., Fu, Q., Webley, P.A., and Qiao, G.G. (2018) Two-Dimensional Nanosheet-Based Gas Separation Membranes. *J. Mater. Chem. A,* 6: 23169-23196. doi:10.1039/c8ta09070j

27. Cheng, Y., Ying, Y., Japip, S., Jiang, S., Chung, T., Zhang, S., and Zhao, D. (2018) Advanced Porous Materials in Mixed Matrix Membranes. *Adv. Mater.,* 30: 1802401. doi:10.1002/adma.201802401

28. Ismail, A. F., Khulbe, K.C., and Matsuura, T. (2015) *Gas Separation Membranes.* Springer International Publishing: Cham.

29. Al-Sayaghi, M., Lewis, J., Buelke, C., and Alshami, A.S. (2018) Physicochemical and Thermal Effects of Pendant Groups, Spatial Linkages and Bridging Groups on the Formation and Processing of Polyimides. *Int. J. Polym. Anal. Charact.,* 23: 566-576. doi:10.1080/1023666X.2018.1505221

30. Mallade, R., and Menendez, M. (2008) *Inorganic Membranes.* Elsevier Science: San Diego, CA, USA.

31. Hinds, B. J., Chopra, N., Rantell, T., Andrews, R., Gavalas, V., and Bachas, L.G. (2004) Aligned Multiwalled Carbon Nanotube Membranes. *Science,* 303: 62-65. doi:10.1126/science.1092048

32. Buelke, C., Alshami, A., Casler, J., Lewis, J., Al-Sayaghi, M., and Hickner, M.A. (2018) Graphene Oxide Membranes for Enhancing Water Purification in Terrestrial and Space-Born Applications: State of the Art. *Desalination,* doi:10.1016/j.desal.2018.09.008

33. Marino, T., Russo, F., Rezzouk, L., Bouzid, A., and Figoli, A. (2017) PES-Kaolin Mixed Matrix Membranes for Arsenic Removal from Water. *Membranes,* 7: 57. doi:10.3390/membranes7040057

34. Penkova, A.V., Dmitrenko, M.E., Savon, N.A., Missyul, A.B., Mazur, A.S., Kuzminova, A.I., Zolotarev, A.A., Mikhailovskii, V., Lahderanta, E., Markelov, D.A., Semenov, K.N., and Ermakov, S.S. (2018) Novel Mixed-Matrix Membranes Based on Polyvinyl Alcohol Modified by Carboxyfullerene for Pervaporation Dehydration. *Sep. Purif. Technol.,* 204: 1-12. doi:10.1016/j.seppur.2018.04.052

35. Ishaq, S., Tamime, R., Bilad, M.R., and Khan, A.L. (2019) Mixed Matrix Membranes Comprising of Polysulfone and Microporous Bio-MOF-1: Preparation and Gas Separation Properties. *Sep. Purif. Technol.,* 210: 442-451. doi:10.1016/j.seppur.2018.08.031

36. Anisuzzaman, S.M., Joseph, C.G., Taufiq-Yap, Y.H., Krishnaiah, D., and Tay, V.V. (2015) Modification of Commercial Activated Carbon for the Removal of 2,4-Dichlorophenol from Simulated Wastewater. *JKSUS.,* 27: 318-330. doi:10.1016/j.jksus.2015.01.002

37. Ahmad, M., Rajapaksha, A.U., Lim, J.E., Zhang, M., Bolan, N., Mohan, D., Vithanage, M., Lee, S.S., and Ok, Y.S. (2014) Biochar as a Sorbent for Contaminant Management in Soil and Water: A Review. *Chemosphere,* 99: 19-33. doi:10.1016/j.chemosphere.2013.10.071

38. Sharma, A., Pareek, V., and Zhang, D. (2015) Biomass pyrolysis—A Review of Modelling, Process Parameters and Catalytic Studies. *Renew. Sust. Energ. Rev.,* 50: 1081-1096. doi:10.1016/j.rser.2015.04.193

39. Efika, C.E., Onwudili, J.A., and Williams, P.T. (2018) Influence of Heating Rates on the Products of High-Temperature Pyrolysis of Waste Wood Pellets and Biomass Model Compounds. *Waste Manage.,* 76: 497-506. doi:10.1016/j.wasman.2018.03.021

40. Guedes, R.E., Luna, A.S., and Torres, A.R. (2018) Operating Parameters for Bio-Oil Production in Biomass Pyrolysis: A Review. *J. Anal. Appl. Pyrolysis,* 129: 134-149. doi:10.1016/j.jaap.2017.11.019

41. Mohan, D., Pittman, C.U., and Steele, P.H. (2006) Pyrolysis of Wood/Biomass for Bio-Oil: A Critical Review. *Energy Fuels,* 20: 848-889. doi:10.1021/ef0502397

42. Han, J., and Kim, H. (2008) The Reduction and Control Technology of Tar during Biomass Gasification/Pyrolysis: An Overview. *Renew. Sust. Energ. Rev.,* 12: 397-416. doi:10.1016/j.rser.2006.07.015

43. Kandel, K., Koc-Karabocek, R., Xu, T., Wang, F.C.Y., and Ferrughelli, D.T. (2018) Upgrading Hydrocarbon Pyrolysis Tar. US20180057759A1

44. Tesser, A., Alemaryeen, A., Lewis, J., Alshami, A., Haghshenas, M., Noghanian, S. PLA-biotar composite substrate for an RF antenna. *In preparation for Sci. Rep.*

45. Xu, T., Lou, L., Luo, L., Cao, R., Duan, D., and Chen, Y. (2012) Effect of Bamboo Biochar on Pentachlorophenol Leachability and Bioavailability in Agricultural Soil. *Sci. Total Environ.,* 414: 727-731. doi:10.1016/j.scitotenv.2011.11.005

46. Ahmad, M., Lee, S.S., Dou, X., Mohan, D., Sung, J., Yang, J.E., and Ok, Y.S. (2012) Effects of Pyrolysis Temperature on Soybean Stover- and Peanut Shell-Derived Biochar Properties and TCE Adsorption in Water. *Bioresour. Technol.,* 118: 536-544. doi:10.1016/j.biortech.2012.05.042

47. Ahmad, M., Lee, S., Lee, S.S., Rajapaksha, A.U., Vithanage, M., Zhang, M., Cho, J.S., and Ok, Y.S. (2013) Trichloroethylene Adsorption by Pine Needle Biochars Produced at various Pyrolysis Temperatures. *Bioresour. Technol.,* 143: 615-622. doi:10.1016/j.biortech.2013.06.033

48. Weber, K., and Quicker, P. (2018) Properties of Biochar. *Fuel,* 217: 240-261. doi:10.1016/j.fuel.2017.12.054

49. Liu, W.J., Jiang, H., and Yu, H.Q. (2015) Development of Biochar-Based Functional Materials: Toward a Sustainable Platform Carbon Material. *Chem. Rev.,* 115 :12251-12285. doi:10.1021/acs.chemrev.5b00195

50. Idrees, M., Batool, S., Kalsoom, T., Kalsoom, A., Yasmeen, S., Raina, S., Zhuang, Q., and Kong, J. (2018) Animal Manure-Derived Biochars Produced Via Fast Pyrolysis for the Removal of Divalent Copper from Aqueous Media. *J. Environ. Manage.,* 213: 109-118. doi:10.1016/j.jenvman.2018.02.003

51. Abdelhafez, A.A., and Li, J. (2016) Removal of Pb(II) from Aqueous Solution by using Biochars Derived from Sugar Cane Bagasse and Orange Peel. *J. Taiwan Inst. Chem. Eng.,* 61: 367-375. doi:10.1016/j.jtice.2016.01.005

52. Saleh, M.E., El-Refaey, A.A., and Mahmoud, A.H. (2016) Effectiveness of Sunflower Seed Husk Biochar for Removing Copper Ions from Wastewater: A Comparative Study. *Soil Water Res.,* 11: 53-63. doi:10.17221/274/2014-SWR

53. Usman, A.R.A., Abduljabbar, A., Vithanage, M., Ok, Y.S., Ahmad, M., Ahmad, M., Elfaki, J., Abdulazeem, S.S., and Al-Wabel, M.I. (2015) Biochar Production from Date Palm Waste: Charring Temperature Induced Changes in Composition and Surface Chemistry. *J. Anal. Appl. Pyrolysis,* 115: 392-400. doi:10.1016/j.jaap.2015.08.016

54. Zielinska, A., and Oleszczuk, P. (2015) Evaluation of Sewage Sludge and Slow Pyrolyzed Sewage Sludge-Derivedbiochar for Adsorption of Phenanthrene and Pyrene. *Bioresour. Technol.,* 192: 618-626. doi:10.1016/j.biortech.2015.06.032

55. Xu, X., Cao, X., and Zhao, L. (2013) Comparison of Rice Husk- and Dairy Manure-Derived Biocharsfor Simultaneously Removing Heavy Metals from Aqueous Solutions: Role of Mineral Components in Biochars. *Chemosphere,* 92: 955-961. doi:10.1016/j.chemosphere.2013.03.009

56. Shen, Y., Wang, S., Tzou, Y., Yan, Y., and Kuan, W. (2012) Removal of Hexavalent Cr by Coconut Coir and Derived Chars – the Effect of Surface Functionality. *Bioresour. Technol.,* 104: 165-172. doi:10.1016/j.biortech.2011.10.096

57. Wang. B., Lehmann, J., Hanley, K., Hestrin, R., and Enders, A. (2015) Adsorption and Desorption of Ammonium by Maple Wood Biocharas a Function of Oxidation and pH. *Chemosphere,* 138: 120-126. doi:10.1016/j.chemosphere.2015.05.062

58. Sun, L., Chen, D., Wan, S., and Yu, Z. (2015) Performance, Kinetics, and Equilibrium of Methylene Blue Adsorption on Biochar Derived from Eucalyptus Saw Dust Modified with Citric, Tartaric, and Acetic Acids. *Bioresour. Technol.,* 198: 300-308. doi:10.1016/j.biortech.2015.09.026

59. Meng, J., Tao, M., Wang, L., Liu, X., and Xu, J. (2018) Changes in Heavy Metal Bioavailability and Speciation from a Pb-Zn Mining Soil Amended with Biochars from Co-Pyrolysis of Rice Straw and Swine Manure. *Sci. Total Environ.,* 633: 300-307. doi:10.1016/j.scitotenv.2018.03.199

60. Luo, M., Lin, H., Li, B., Dong, Y., He, Y., and Wang, L. (2018) A Novel Modification of Lignin on Corncob-Based Biochar to Enhance Removal of Cadmium from Water. *Bioresour. Technol.,* 259: 312-318. doi:10.1016/j.biortech.2018.03.075

61. Yang, X., Kwon, E.E., Dou, X., Zhang, M., Kim, K., Tsang, D.C.W., and Ok, Y.S. (2018) Fabrication of Spherical Biochar by a Two-Step Thermal Process from Waste Potato Peel. *Sci. Total Environ.,* 626: 478-485. doi:10.1016/j.scitotenv.2018.01.052

62. Elleuch, A., Boussetta, A., Yu, J., Halouani, K., and Li, Y. (2013) Experimental Investigation of Direct Carbon Fuel Cell Fueled by Almond Shell Biochar: Part I. Physico-Chemical Characterization of the Biochar Fuel and Cell Performance Examination. *Int. J. Hydrogen Energy,* 38: 16590-16604. doi:10.1016/j.ijhydene.2013.08.090

63. Zhang, T., Walawender, W. P., Fan, L. T., Fan, M., Daugaard, D., and Brown, R.C. (2004) Preparation of Activated Carbon from Forest and Agricultural Residues through CO2 Activation. *Chem. Eng. J.,* 105: 53-59. doi:10.1016/j.cej.2004.06.011

64. Shim, T., Yoo, J., Ryu, C., Park, Y., and Jung, J. (2015) Effect of Steam Activation of Biochar Produced from a Giant Miscanthus on Copper Sorption and Toxicity. *Bioresour. Technol.,* 197: 85-90. doi:10.1016/j.biortech.2015.08.055

65. Xiao, F., Bedane, A.H., Zhao, J.X., Mann, M.D., and Pignatello, J.J. (2018) Thermal Air Oxidation Changes Surface and Adsorptive Properties of Black Carbon (Char/Biochar). *Sci. Total Environ.,* 618: 276-283. doi:10.1016/j.scitotenv.2017.11.008

66. Ioannidou, O., and Zabaniotou, A. (2007) Agricultural Residues as Precursors for Activated Carbon production-A Review. *Renew. Sust. Energ Rev.,* 11: 1966-2005. doi:10.1016/j.rser.2006.03.013

67. Dehkhoda, A.M., Gyenge, E., and Ellis, N. (2016) A Novel Method to Tailor the Porous Structure of KOH-Activated Biochar and its Application in Capacitive Deionization and Energy Storage. *Biomass Bioenergy,* 87: 107-121. doi:10.1016/j.biombioe.2016.02.023

68. Islam, M.A., Tan, I.A.W., Benhouria, A., Asif, M., and Hameed, B.H. (2015) Mesoporous and Adsorptive Properties of Palm Date Seed Activated Carbon Prepared Via Sequential Hydrothermal Carbonization and Sodium Hydroxide Activation. *Chem.l Eng. J.,* 270: 187-195. doi:10.1016/j.cej.2015.01.058

69. Aljeboree, A.M., Alshirifi, A.N. and Alkaim, A.F. (2017) Kinetics and Equilibrium Study for the Adsorption of Textile Dyes on Coconut Shell Activated Carbon. *Arab. J. Chem.,* 10: S3393. doi:10.1016/j.arabjc.2014.01.020

70. Demiral, H., and Gungor, C. (2016) Adsorption of Copper(II) from Aqueous Solutions on Activated Carbon Prepared from Grape Bagasse. *J. Clean. Prod.,* 124: 103-113. doi:10.1016/j.jclepro.2016.02.084

71. Ozdemir, I., Şahin, M., Orhan, R., and Erdem, M. (2014) Preparation and Characterization of Activated Carbon from Grape Stalk by Zinc Chloride Activation. *Fuel Process. Technol.,* 125: 200-206. doi:10.1016/j.fuproc.2014.04.002

72. Muniandy, L., Adam, F., Mohamed, A.R., and Ng, E. (2014) The Synthesis and Characterization of High Purity Mixed Microporous/Mesoporous Activated Carbon from Rice Husk using Chemical Activation with NaOH and KOH. *Microporous Mesoporous Mater.,* 197: 316-323. doi:10.1016/j.micromeso.2014.06.020

73. Liou, T.H. (2010) Development of Mesoporous Structure and High Adsorption Capacity of Biomass-Based Activated Carbon by Phosphoric Acid and Zinc Chloride Activation. *Chem. Eng. J.,* 158: 129-142. doi:10.1016/j.cej.2009.12.016

74. Nayak, A., Bhushan, B., Gupta, V., and Sharma, P. (2017) Chemically Activated Carbon from Lignocellulosic Wastes for Heavy Metal Wastewater Remediation: Effect of Activation Conditions. *J. Colloid Interface Sci.,* 493: 228-240. doi:10.1016/j.jcis.2017.01.031

75. Yorgun, S., and Yıldız, D. (2015) Preparation and Characterization of Activated Carbons from Paulownia Wood by Chemical Activation with H3PO4. *J. Taiwan Inst. Chem. Eng.,* 53: 122-131. doi:10.1016/j.jtice.2015.02.032

76. Iriarte-Velasco, U., Sierra, I., Cepeda, E.A., Bravo, R., and Ayastuy, J.L. (2015) Methylene Blue Adsorption by Chemicallyactivated Waste Pork Bones. *Color. Technol.,* 131: 322-332. doi:10.1111/cote.12160

77. Kiyono, M., Williams, P.J., and Koros, W.J. (2010) Effect of Pyrolysis Atmosphere on Separation Performance of Carbon Molecular Sieve Membranes. *J. Membr. Sci.,* 359: 2-10. doi:10.1016/j.memsci.2009.10.019

78. Hassan, M., Abou-Zeid, R., Hassan, E., Berglund, L., Aitomäki, Y., and Oksman, K. (2017) Membranes Based on Cellulose Nanofibers and Activated Carbon for Removal of Escherichia Coli Bacteria from Water. *Polymers,* 9: 335. doi:10.3390/polym9080335

79. Mushardt, H., Müller, M., Shishatskiy, S., Wind, J., and Brinkmann, T. (2016) Detailed Investigation of Separation Performance of a MMM for Removal of Higher Hydrocarbons Under Varying Operating Conditions. *Membranes,* 6:16. doi:10.3390/membranes6010016

80. Tanco, M.A.L., and Tanaka, D.A.P. (2016) Recent Advances on Carbon Molecular Sieve Membranes (CMSMs) and Reactors. *Processes,* 4: 29. doi:10.3390/pr4030029

81. Nasir, R., Mukhtar, H., Man, Z., Dutta, B.K., Shaharun, M.S., and Abu Bakar, M.Z. (2015) Mixed Matrix Membrane Performance Enhancement using Alkanolamine Solution. *J. Membr. Sci.,* 483: 84-93. doi:10.1016/j.memsci.2015.02.041

82. Dong, G., Li, H., and Chen, V. (2013) Challenges and Opportunities for Mixed-Matrix Membranes for Gas Separation. *J. Mater. Chem. A,* 1: 4610. doi:10.1039/c3ta00927k

83. Jia, M., Pleinemann, K., and Behling, R. (1992) Preparation and Characterization of Thin-Film zeolite–PDMS Composite Membranes. *J. Membr. Sci.,* 73: 119-128. doi:10.1016/0376-7388(92)80122-Z

84. Torras, C., Ferrando, F., Paltakari, J., and Garcia-Valls, R. (2006) Performance, Morphology and Tensile Characterization of Activated Carbon Composite Membranes for the Synthesis of Enzyme Membrane Reactors. *J. Membr. Sci.,* 282: 149-161. doi:10.1016/j.memsci.2006.05.018

85. Galizia, M., Chi, W.S., Smith, Z.P., Merkel, T.C., Baker, R.W., and Freeman, B.D. (2017) 50th Anniversary Perspective: Polymers and Mixed Matrix Membranes for Gas and Vapor Separation: A Review and Prospective Opportunities. *Macromolecules,* 50: 7809-7843. doi:10.1021/acs.macromol.7b01718

86. Nasir, R., Mukhtar, H., Man, Z. and Mohshim, D.F. (2013) Material Advancements in Fabrication of Mixed-Matrix Membranes. *Chem. Eng. Technol.,* 36: 717-727. doi:10.1002/ceat.201200734

87. Michele, L.D., Zaccone, A., and Eiser, E. (2012) Analytical Theory of Polymer-Network-Mediated Interaction between Colloidal Particles. *Proc. Natl. Acad. Sci. USA.* 109: 10187-10192. doi:10.1073/pnas.1202171109

88. Bar-Chaput, S. and Carrot, C. (2006) Interactions of Active Carbon with Low- and High-molecular Weight Polyethylene Glycol and Polyethylene Oxide. *J. Appl. Polym. Sci.,* 100: 3490-3497. doi:10.1002/app.22149

89. Mushardt, H., Kramer, V., Hülagü, D., Brinkmann, T., and Kraume, M. (2014) Development of Solubility Selective Mixed Matrix Membranes for Gas Separation. *Chem. Ing. Tech.,* 86: 83-91. doi:10.1002/cite.201300074

90. García, M.G., Marchese, J., and Ochoa, N.A. (2010) Effect of the Particle Size and Particle Agglomeration on Composite Membrane Performance. *J. Appl. Polym. Sci.,* 118: 2417-2424. doi:10.1002/app.32274

91. Mukherjee, R., and De, S. (2016) Preparation, Characterization and Application of Powdered Activated Carbon-cellulose Acetate Phthalate Mixed Matrix Membrane for Treatment of Steel Plant Effluent. *Polym. Adv. Technol.,* 27: 444-459. doi:10.1002/pat.3690

92. Kusworo, T.D., Ismail, A.F., Mustafa, A., and Budiyono. (2010) Application of Activated Carbon Mixed Matrix Membrane for Oxygen Purification. *Int. J. Sci. Eng.,* 1: 21-24.

93. Kumar, S.K., Li, C., Schadler, L.S., Bansal, A., Cho, K., Yang, H., and Benicewicz, B.C. (2005) Quantitative Equivalence between Polymer Nanocomposites and Thin Polymer Films. *Nat. Mat.,* 4: 693-698. doi:10.1038/nmat1447

94. Lin, R., Villacorta Hernandez, B., Ge, L., and Zhu, Z. (2018) Metal Organic Framework Based Mixed Matrix Membranes: An Overview on Filler/Polymer Interfaces. *J. Mater. Chem. A,* 6: 293-312. doi:10.1039/c7ta07294e

95. Lan, Y., and Wang, W. (2017) Application of Tree Biochar in PDMS Pervaporation Membranes. *Adv. Polym. Technol.,* doi:10.1002/adv.21856

96. Mohshim, D.F., Mukhtar, H., and Man, Z. (2014) The Effect of Incorporating Ionic Liquid into Polyethersulfone-SAPO34 Based Mixed Matrix Membrane on CO2 Gas Separation Performance. *Sep. Purif. Technol.,* 135: 252-258. doi:10.1016/j.seppur.2014.08.019

97. Mohshim, D.F., Mukhtar, H.B., Man, Z., and Nasir, R. (2013) Latest Development on Membrane Fabrication for Natural Gas Purification: A Review. *J. Eng.,* 2013: 1-7. doi:10.1155/2013/101746

98. Ebadi Amooghin, A., Mashhadikhan, S., Sanaeepur, H., Moghadassi, A., Matsuura, T., and Ramakrishna, S. (2019) Substantial Breakthroughs on Function-Led Design of Advanced Materials used in Mixed Matrix Membranes (MMMs): A New Horizon for Efficient CO2 Separation. *Prog. Mater. Sci.,* 102: 222-295. doi:10.1016/j.pmatsci.2018.11.002

99. Saranya, R., Kumar, M., Tamilarasan, R., Ismail, A.F., and Arthanareeswaran, G. (2016) Functionalised Activated Carbon Modified Polyphenylsulfone Composite Membranes for Adsorption Enhanced Phenol Filtration. *J. Chem. Technol. Biotechnol.,* 91: 748-761. doi:10.1002/jctb.4641

100. Spahis, N., Dellali, M., and Mahmoudi, H. (2012) Synthesis and Characterization of Polymeric/Activated Carbon Membranes. *Procedia Eng.,* 33: 47-51. doi:10.1016/j.proeng.2012.01.1175

101. Ballinas-Casarrubias, L., Terrazas-Bandala, L.P., Ibarra-Gomez, R., Mendoza-Duarte, M.E., Manjarrez-Nevarez, L., and Gonzalez-Sanchez, G. (2006) Structural and Performance Variation of Activated Carbon-Polymer films. *Polym. Adv. Technol.,* 17: 991-999. doi:10.1002/pat.842

102. Garcia, M., Marchese, J., and Ochoa, N. (2012) High Activated Carbon Loading Mixed Matrix Membranes for Gas Separations. *J Mater Sci,* 47: 3064-3075. doi:10.1007/s10853-011-6138-8

103. Shen, G., Zhao, J., Guan, K., Shen, J., and Jin, W. (2017) Highly Efficient Recovery of Propane by Mixed-matrix Membrane Via Embedding Functionalized Graphene Oxide Nanosheets into Polydimethylsiloxane. *AIChE J.,* 63: 3501-3510. doi:10.1002/aic.15720

104. Li, Q., Cheng, L., Shen, J., Shi, J., Chen, G., Zhao, J., Duan, J., Liu, G., and Jin, W. (2017) Improved Ethanol Recovery through Mixed-Matrix Membrane with Hydrophobic MAF-6 as Filler. *Sep.Purif. Technol.,* 178: 105-112. doi:10.1016/j.seppur.2017.01.024

105. Bakeri, G., Ismail, A.F., Shariaty-Niassar, M., and Matsuura, T. (2010) Effect of Polymer Concentration on the Structure and Performance of Polyetherimide Hollow Fiber Membranes. *J. Membr. Sci.,* 363: 103-111. doi:10.1016/j.memsci.2010.07.018

106. Ariono, D., Aryanti, P.T.P., Subagjo, S., and Wenten, I.G. (2017) The Effect of Polymer Concentration on Flux Stability of Polysulfone Membrane. *AIP Conf. Proc.,* 1788: 030048. doi:10.1063/1.4968301

107. Adewole, J.K., Ahmad, A.L., Ismail, S., Leo, C.P., and Sultan, A.S. (2015) Comparative Studies on the Effects of Casting Solvent on Physico-Chemical and Gas Transport Properties of Dense Polysulfone Membrane used for CO2/CH4separation. *J. Appl. Polym. Sci.,* 132: 42205. doi:10.1002/app.42205

108. Guillen, G.R., Pan, Y., Li, M., and Hoek, E.M.V. (2011) Preparation and Characterization of Membranes Formed by Nonsolvent Induced Phase Separation: A Review. *Ind. Eng. Chem. Res.,* 50: 3798-3817. doi:10.1021/ie101928r

109. Azimi, H., Tezel, F.H., and Thibault, J. (2017) Effect of Embedded Activated Carbon Nanoparticles on the Performance of Polydimethylsiloxane (PDMS) Membrane for Pervaporation Separation of Butanol. *J. Chem. Technol. Biotechnol.,* 92: 2901-2911. doi:10.1002/jctb.5306

110. Wan, C.F., Yang, T., Lipscomb, G.G., Stookey, D.J., and Chung, T. (2017) Design and Fabrication of Hollow Fiber Membrane Modules. *J. Membr. Sci.,* 538: 96-107. doi:10.1016/j.memsci.2017.05.047

111. Tijink, M.S.L., Wester, M., Sun, J., Saris, A., Bolhuis-Versteeg, L.A.M., Saiful, S., Joles, J.A., Borneman, Z., Wessling, M., and Stamatialis, D.F. (2012) A Novel Approach for Blood Purification: Mixed-Matrix Membranes Combining Diffusion and Adsorption in One Step. *Acta Biomater.,* 8: 2279-2287. doi:10.1016/j.actbio.2012.03.008

112. Tijink, M.S.L., Wester, M., Glorieux, G., Gerritsen, K.G.F., Sun, J., Swart, P.C., Borneman, Z., Wessling, M., Vanholder, R., Joles, J.A., and Stamatialis, D. (2013) Mixed Matrix Hollow Fiber Membranes for Removal of Protein-Bound Toxins from Human Plasma. *Biomaterials,* 34: 7819-7828. doi:10.1016/j.biomaterials.2013.07.008

113. Feng, C.Y., Khulbe, K.C., Matsuura, T., and Ismail, A.F. (2013) Recent Progresses in Polymeric Hollow Fiber Membrane Preparation, Characterization and Applications. *Sep. Purif. Technol.,* 111: 43-71. doi:10.1016/j.seppur.2013.03.017

114. Ren, J., Zhou, J., and Deng, M. (2010) Morphology Transition of Asymmetric Polyetherimide Flat Sheet Membranes with Different Thickness by Wet Phase-Inversion Process. *Sep.Purif. Technol.,* 74: 119-129. doi:10.1016/j.seppur.2010.05.014

115. Buonomenna, M.G., Figoli, A., Jansen, J.C., and Drioli, E. (2004) Preparation of Asymmetric PEEKWC Flat Membranes with Different Microstructures by Wet Phase Inversion. *J. Appl. Polym. Sci.,* 92: 576-591. doi:10.1002/app.20042

116. Sadrzadeh, M., and Bhattacharjee, S. (2013) Rational Design of Phase Inversion Membranes by Tailoring Thermodynamics and Kinetics of Casting Solution using Polymer Additives. *J. Membr. Sci.,* 441: 31-44. doi:10.1016/j.memsci.2013.04.009

117. Garcia-Ivars, J., Iborra-Clar, M., Alcaina-Miranda, M., and Van der Bruggen, B. (2015) Comparison between Hydrophilic and Hydrophobic Metal Nanoparticles on the Phase Separation Phenomena during Formation of Asymmetric Polyethersulphone Membranes. *J. Membr. Sci.,* 493: 709-722. doi:10.1016/j.memsci.2015.07.009

118. Mazinani, S., Darvishmanesh, S., Ehsanzadeh, A. and Van der Bruggen, B. (2017) Phase Separation Analysis of Extem/Solvent/Non-Solvent Systems and Relation with Membrane Morphology. *J. Membr. Sci.,* 526: 301-314. doi:10.1016/j.memsci.2016.12.031

119. Dahe, G.J., Singh, R.P., Dudeck, K.W., Yang, D., Berchtold, K.A. (2019) Influence of non-solvent chemistry on polybenzimidazole hollow fiber membrane preparation. *J. Membr. Sci.,* 577: 91-103. doi:10.1016/j.memsci.2019.02.001

120. Hwang L.L., Chen, J.C., and Wey, M.Y. (2013) The Properties and Filtration Efficiency of Activated Carbon Polymer Composite Membranes for the Removal of Humic Acid. *Desalination,* 313: 166-175. doi:10.1016/j.desal.2012.12.019

121. Aghili, F., Ghoreyshi, A.A., Rahimpour, A., and Rahimnejad, M. (2017) Coating of Mixed-Matrix Membranes with Powdered Activated Carbon for Fouling Control and Treatment of Dairy Effluent. *Process Saf. Environ. Prot.,* 107: 528-539. doi:10.1016/j.psep.2017.03.013

122. He, J., Song, Y., and Chen, J.P. (2017) Development of a Novel Biochar/PSF Mixed Matrix Membrane and Study of Key Parameters in Treatment of Copper and Lead Contaminated Water. *Chemosphere,* 186: 1033-1045. doi:10.1016/j.chemosphere.2017.07.028

123. Hosseini, S.M., Amini, S.H., Khodabakhshi, A.R., Bagheripour, E., and Van der Bruggen, B. (2018) Activated Carbon Nanoparticles Entrapped Mixed Matrix Polyethersulfone Based Nanofiltration Membrane for Sulfate and Copper Removal from Water. *J. Taiwan Inst. Chem. Eng.,* 82: 169-178. doi:10.1016/j.jtice.2017.11.017

124. Marchese, J., Anson, M., Ochoa, N.A., Prádanos, P., Palacio, L., and Hernandez, A. (2006) Morphology and Structure of ABS Membranes Filled with Two Different Activated Carbons. *Chem. Eng. Sci.,* 61: 5448-5454. doi:10.1016/j.ces.2006.04.013

125. Soroko, I., Makowski, M., Spill, F., and Livingston, A. (2011) The Effect of Membrane Formation Parameters on Performance of Polyimide Membranes for Organic Solvent Nanofiltration (OSN). Part B: Analysis of Evaporation Step and the Role of a Co-Solvent. *J. Membr. Sci.,* 381: 163-171. doi:10.1016/j.memsci.2011.07.028

126. Gorgojo, P., Karan, S., Wong, H.C., Jimenez-Solomon, M.F., Cabral, J.T., and Livingston, A.G. (2014) Membranes: Ultrathin Polymer Films with Intrinsic Microporosity: Anomalous Solvent Permeation and High Flux Membranes. *Adv. Funct. Mater.,* 24: 4728. doi:10.1002/adfm.201470198

127. Woock, T.W. (2016) Effect of Bridging Group of Dianhydride Precursor on Resulting Thermally Rearranged Polybenzoxazole for Removal of Nitrogen from Natural Gas. *ProQuest Dissertations Publishing*.

128. Farahani, M.H.D.A., Hua, D., and Chung, T.S. (2018) Cross-Linked Mixed Matrix Membranes (MMMs) Consisting of Amine-Functionalized Multi-Walled Carbon Nanotubes and P84 Polyimide For organic Solvent Nano Filtration (OSN) with Enhanced Flux. *J. Membr. Sci.,* 548: 319-331. doi:10.1016/j.memsci.2017.11.037

129. Tashvigh, A.A., Luo, L., Chung, T.S., Weber, M., and Maletzko, C. (2018) A Novel Ionically Cross-Linked Sulfonated Polyphenylsulfone (sPPSU) Membrane for Organic Solvent Nanofiltration (OSN). *J. Membrane Sci.,* 545: 221-228. doi:10.1016/j.memsci.2017.09.076

130. Pinnau, I. and Koros, W.J. (1991) Structures and Gas Separation Properties of Asymmetric Polysulfone Membranes made by Dry, Wet, and Dry/Wet Phase Inversion. *J. Appl. Polym. Sci.,* 43: 1491-1502. doi:10.1002/app.1991.070430811

131. Snoeyink, V.L., and Weber, W.J. (1967) The Surface Chemistry of Active Carbon; a Discussion of Structure and Surface Functional Groups. *Environ. Sci. Technol.,* 1: 228-234. doi:10.1021/es60003a003

132. Ganesh, B.M., Isloor, A.M., and Ismail, A.F. (2013) Enhanced Hydrophilicity and Salt Rejection Study of Graphene Oxide-Polysulfone Mixed Matrix Membrane. *Desalination,* 313: 199-207. doi://doi.org/10.1016/j.desal.2012.11.037

133. Rahimpour, A., Madaeni, S.S., Jahanshahi, M., Mansourpanah, Y., and Mortazavian, N. (2009) Development of High Performance Nano-Porous Polyethersulfone Ultrafiltration Membranes with Hydrophilic Surface and Superior Antifouling Properties. *Appl. Surf. Sci.,* 255: 9166-9173. doi:10.1016/j.apsusc.2009.06.123

134. Rahimpour, A., Madaeni, S.S., and Mansourpanah, Y. (2007) The Effect of Anionic, Non-Ionic and Cationic Surfactants on Morphology and Performance of Polyethersulfone Ultrafiltration Membranes for Milk Concentration. *J. Membr. Sci.,* 296: 110-121. doi:10.1016/j.memsci.2007.03.029

135. Mohamad Said, K.A., George, G.G., Mohamed Alipah, N.A., Ismail, N.Z., Jamain, R.L., Mili, N., Salleh, S.F., Mohamed Amin, M.A., Muslimen, R., Yakub, I., and Mohamed Sutan, N. (2017) Effect of Activated

Carbon in Polysufone-Polyethyleneimine-Silver Composite Membrane Towards Adsorption of Chromium (Cr), Lead (Pb), Silver (Ag) and Cadmium (Cd) in Synthetic Wastewater. *J. Mater. Environ. Sci.,* 8: 3740-3746.

136. Hofman, M., and Pietrzak, R. (2013) Copper Ions Removal from Liquid Phase by Polyethersulfone (PES) Membranes Functionalized by Introduction of Carbonaceous Materials. *Chem. Eng. J.,* 215-216: 216-221. doi:10.1016/j.cej.2012.10.079

137. Belgacem, A., Rebiai, R., Hadoun, H., Khemaissia, S., and Belmedani, M. (2014) The Removal of Uranium (VI) from Aqueous Solutions onto Activated Carbon Developed from Grinded used Tire. *Environ. Sci. Pollut. Res.,* 21: 684-694. doi:10.1007/s11356-013-1940-2

138. Villalobos-Rodríguez, R., Ruíz Cuilty, K., Montero-Cabrera, M.E., Esparza-Ponce, H.E., Nevarez-Moorillon, G.V., Fierro, V., Celzard, A., and Ballinas-Casarrubias, M.L. (2015) Iron Influence on Uranium Removal from Water using Cellulose Acetate Membranes Doped with Activated Carbon. *Desal. Water Treat.,* 56: 3476-3485. doi:10.1080/19443994.2014.980333

139. Sridhar, S., Smitha, B., Suryamurali, R., and Aminabhavi, T.M. (2008) Synthesis, Characterization and Gas Permeability of an Activated Carbon-Loaded PEBAX 2533 Membrane. *Des. Monomers Polym.,* 11: 17-27. doi:10.1163/156855508X292392

140. Nasir, R., Mukhtar, H., Man ,Z., Shaharun, M.S., and Abu Bakar, M.Z. (2015) Effect of Fixed Carbon Molecular Sieve (CMS) Loading and various Di-Ethanolamine (DEA) Concentrations on the Performance of a Mixed Matrix Membrane for CO2/CH4 Separation. *RSC Adv.,* 5: 6814-6822. doi:10.1039/c5ra09015f

141. Guo, B., Tay, S.W., Liu, Z., and Hong, L. (2012) Assimilation of Highly Porous Sulfonated Carbon Nanospheres into Nafion® Matrix as Proton and Water Reservoirs. *Int. J. Hydrogen Energy,* 37: 14482-14491. doi:10.1016/j.ijhydene.2012.07.112

142. Tsai, L., Chien, H., Wang, C., Lai, C., Lin, J., Zhu, C., and Chang, F. (2013) Poly(Ethylene Glycol) Modified Activated Carbon for High Performance Proton Exchange Membrane Fuel Cells. *Int. J. Hydrogen Energy,* 38: 11331-11339. doi:10.1016/j.ijhydene.2013.06.054

143. Chien, H., Tsai, L., Lai, C., Lin, J., Zhu, C., and Chang, F. (2013) Characteristics of High-Water-Uptake Activated Carbon/Nafion Hybrid Membranes for Proton Exchange Membrane Fuel Cells. *J. Power Sources,* 226: 87-93. doi:10.1016/j.jpowsour.2012.10.017

144. Chai, Z., Wang, C., Zhang, H., Doherty, C.M., Ladewig, B.P., Hill, A.J., and Wang, H. (2010) Nafion-Carbon Nanocomposite Membranes Prepared using Hydrothermal Carbonization for Proton-Exchange-Membrane Fuel Cells. *Adv. Funct. Mater.,* 20: 4394-4399. doi:10.1002/adfm.201001412

145. Bhalara, P.D., Punetha, D., and Balasubramanian, K. (2014) A Review of Potential Remediation Techniques for Uranium(VI) Ion Retrieval from Contaminated Aqueous Environment. *J. Environ. Chem. Eng.,* 2: 1621-1634. doi:10.1016/j.jece.2014.06.007

146. Pal, P. and Kumar, R. (2014) Treatment of Coke Wastewater: A Critical Review for Developing Sustainable Management Strategies. *Sep. Purif. Rev.,* 43: 89-123. doi:10.1080/15422119.2012.717161

147. Sani, N., Lau, W. and Ismail, A. (2015) Morphologies and Separation Characteristics of Polyphenylsulfone-Based Solvent Resistant Nanofiltration Membranes: Effect of Polymer Concentration in Casting Solution and Membrane Pretreatment Condition. *Korean J. Chem. Eng.,* 32: 743-752. doi:10.1007/s11814-014-0281-2

148. Yam-Cervantes, M.A., Santiago-García, J.L., Loria-Bastarrachea, M.I., Duarte-Aranda, S., Alberto Ruiz-Trevino, F., and Aguilar-Vega, M. (2017) Sulfonated Polyphenylsulfone Asymmetric Membranes: Effect of Coagulation Bath (Acetic acid-NaHCO3/Isopropanol) on Morphology and Antifouling Properties. *J. Appl. Polym. Sci.,* 134: 44502. doi:10.1002/app.44502

149. Yuan, W., and Zydney, A.L. (2000) Humic Acid Fouling during Ultrafiltration. *Environ. Sci. Technol.,* 34: 5043-5050. doi:10.1021/es0012366

150. Guo, W., Ngo, H., and Li, J. (2012) A Mini-Review on Membrane Fouling. *Bioresour. Technol.,* 122: 27-34. doi:10.1016/j.biortech.2012.04.089

151. Roy, A. and De, S. (2017) State-of-the-Art Materials and Spinning Technology for Hemodialyzer Membranes. *Sep. Purif. Rev.,* 46: 216-240. doi:10.1080/15422119.2016.1256323

152. Vinh-Thang, H., and Kaliaguine, S. (2013) Predictive Models for Mixed-Matrix Membrane Performance: A Review. *Chem. Rev.,* 113: 4980-5028. doi:10.1021/cr3003888

153. Robeson, L.M. (2008) The Upper Bound Revisited. *J. Membr. Sci.,* 320: 390-400. doi:10.1016/j.memsci.2008.04.030

154. Chuah, C.Y., Goh, K., Yang, Y., Gong, H., Li, W., Karahan, H.E., Guiver, M.D., Wang, R., and Bae, T.H. (2018) Harnessing Filler Materials for Enhancing Biogas Separation Membranes. *Chem. Rev.,* 118: 8655-8769. doi:10.1021/acs.chemrev.8b00091

155. Fu, X.Y., Sotani, T., and Matsuyama, H. (2008) Effect of Membrane Preparation Method on the Outer Surface Roughness of Cellulose Acetate Butyrate Hollow Fiber Membrane. *Desalination,* 233: 10-18. doi:10.1016/j.desal.2007.09.022

156. Ahmadi, M., Janakiram, S., Dai, Z., Ansaloni, L., and Deng, L. (2018) Performance of Mixed Matrix Membranes Containing Porous Two-Dimensional (2D) and Three-Dimensional (3D) Fillers for CO2 Separation: A Review. *Membranes,* 8: 50. doi:10.3390/membranes8030050

157. Scholes, C.A., Stevens, G.W., and Kentish, S.E. (2012) Membrane Gas Separation Applications in Natural Gas Processing. *Fuel,* 96: 15-28. doi:10.1016/j.fuel.2011.12.074

158. Bakangura, E., Wu, L., Ge, L., Yang, Z., and Xu, T. (2016) Mixed Matrix Proton Exchange Membranes for Fuel Cells: State of the Art and Perspectives. *Prog. Polym. Sci.,* 57: 103-152. doi:10.1016/j.progpolymsci.2015.11.004

159. Ahmed, M.J.K., Ahmaruzzaman, M. (2016) A Review on Potential Usage of Industrial Waste Materials for Binding Heavy Metal Ions from Aqueous Solutions. *J. Water Process Eng.,* 10: 39-47. doi:10.1016/j.jwpe.2016.01.014

160. Tan, X., Liu, S., Liu, Y., Gu, Y., Zeng, G., and Hu, X. (2017) Biochar as Potential Sustainable Precursors for Activated Carbon Production: Multiple Applications in Environmental Protection and energy Storage. *Bioresour. Technol.,* 227: 359-372. doi:10.1016/j.biortech.2016.12.083

161. Gonzo, E.E., Parentis, M.L., and Gottifredi, J.C. (2006) Estimating Models for Predicting Effective Permeability of Mixed Matrix Membranes. *J. Membr. Sci.,* 277: 46-54. doi:10.1016/j.memsci.2005.10.007

162. Ji, W., Sikdar, S.K., and Hwang, S. (1995) Sorption, Diffusion and Permeation of 1,1,1-Trichloroethane through Adsorbent-Filled Polymeric Membranes. *J. Membr. Sci.,* 103: 243-255. doi:10.1016/0376-7388(95)00007-Y

163. Jusoh, N., Yeong, Y.F., Chew, T.L., Lau, K.K., and Shariff, A.M. (2016) Current Development and Challenges of Mixed Matrix Membranes for CO2/CH4 Separation. *Sep. Purif. Rev.,* 45: 321-344. doi:10.1080/15422119.2016.1146149

164. Brettmann, B.K., Tsang, S., Forward, K.M., Rutledge, G.C., Myerson, A.S., and Trout, B.L. (2012) Free Surface Electrospinning of Fibers Containing Microparticles. *Langmuir,* 28: 9714-9721. doi:10.1021/la301422x

CHAPTER III

1. P.S. Goh; A.F. Ismail; S.M. Sanip; B.C. Ng; M. Aziz. Separation and Purification Technology 2011, 81, 243.

2. Dechnik, J.; Sumby, C. J.; Janiak, C. Crystal Growth & Design 2017, 17, 4467.

3. Bastani, D.; Esmaeili, N.; Asadollahi, M. Journal of Industrial and Engineering Chemistry 2013, 19, 375.

4. Hu, K.; Kulkarni, D. D.; Choi, I.; Tsukruk, V. V. Progress in Polymer Science 2014, 39, 1934.

5. Rodríguez-González, J.; Rubio-González, C.; Jiménez-Mora, M.; Ramos-Galicia, L.; Velasco-Santos, C. Appl Compos Mater 2018, 25, 1115.

6. Kamel, N. A.; Abd El-Messieh, S. L.; Saleh, N. M. Materials science & engineering. C, Materials for biological applications 2017, 72, 543.

7. Etienne, S.; Becker, C.; Ruch, D.; Germain, A.; Calberg, C. J Therm Anal Calorim 2010, 100, 667.

8. Chen, D.; Chen, S.; Yi, R.; Xu, T.; Gordin, M. L.; Wang, D. Solid State Ionics 2014, 254, 65.

9. El Miri, N.; Abdelouahdi, K.; Zahouily, M.; Fihri, A.; Barakat, A.; Solhy, A.; El Achaby, M. Journal of Applied Polymer Science 2015, 132.

10. Anson, M.; Marchese, J.; Garis, E.; Ochoa, N.; Pagliero, C. Journal of Membrane Science 2004, 243, 19.

11. Marchese, J.; Anson, M.; Ochoa, N. A.; Prádanos, P.; Palacio, L.; Hernández, A. Chemical Engineering Science 2006, 61, 5448.

12. Kotal, M.; Bhowmick, A. K. Progress in Polymer Science 2015, 51, 127.

13. Tijink, M. S. L.; Wester, M.; Sun, J.; Saris, A.; Bolhuis-Versteeg, L. A. M.; Saiful, S.; Joles, J. A.; Borneman, Z.; Wessling, M.; Stamatialis, D. F. Acta Biomaterialia 2012, 8, 2279.

14. Yan, B.; Wang, Y.; Wu, X. Advanced Composite Materials 2018, 27, 387.

15. Hu, J.; Jia, X.; Li, C.; Ma, Z.; Zhang, G.; Sheng, W.; Zhang, X.; Wei, Z. J Mater Sci 2014, 49, 2943.

16. Hoang Vinh-Thang; Serge Kaliaguine. Chemical Reviews 2013, 113, 4980.

17. Rong, M. Z.; Zhang, M. Q.; Ruan, W. H. Materials Science and Technology 2006, 22, 787.

18. Li, Z.; Chu, J.; Yang, C.; Hao, S.; Bissett, M. A.; Kinloch, I. A.; Young, R. J. Composites Science and Technology 2018, 163, 116.

19. Sorribas, S.; Gorgojo, P.; Tellez, C.; Coronas, J.; Livingston, A. G. JOURNAL OF THE AMERICAN CHEMICAL SOCIETY 2013.

20. Paul, D. R.; Robeson, L. M. Polymer 2008, 49, 3187.

21. Mousa, M.; Dong, Y. ACS Sustainable Chemistry & Engineering 2018, 6, 467.

22. Wu-Jun Liu; Hong Jiang; Han-Qing Yu. Chemical Reviews 2015, 115, 12251.

23. Mousa, M.; Dong, Y.; Davies, I. J. Advanced Composite Materials 2018, 27, 499.

24. Buelke, C.; Alshami, A.; Casler, J.; Lewis, J.; Al-Sayaghi, M.; Hickner, M. A. Desalination 2018.

25. Guillen, G. R.; Pan, Y.; Li, M.; Hoek, E. M. V. 2011.

26. Pinnau, I.; Koros, W. J. Journal of Applied Polymer Science 1991, 43, 1491.

27. Hu, P.; Yan, L.; Zhao, C.; Zhang, Y.; Niu, J. Composites Science and Technology 2018, 168, 327.

28. ASTM Standard D4607. 2015.

29. Pan, D.; Jaroniec, M.; Klinik, J. Carbon 1996, 34, 1109.

30. Mercuri, L. P.; Matos, J. R.; Li, Z.; Jaroniec, M. Journal of Colloid and Interface Science 2006, 296, 377.

31. Syed, R.; Sobh, N.; Ravaioli, U.; Popescu, G.; Mohamed, M. 2015.

32. Costa, E.; Aquilano, D. Crystals 2018, 8, 238.

33. Zisman, W. A. Advances in Chemistry 1964, 1.

34. Kabza, K. G.; Gestwicki, J. E.; McGrath, J. L. Journal of Chemical Education 2000, 77, 63.

35. Tsai, W.; Chang, C.; Lee, S.; Wang, S. Journal of Thermal Analysis and Calorimetry 2000, 63, 351.

36. Kumar, S. K.; Li, C.; Schadler, L. S.; Bansal, A.; Cho, K.; Yang, H.; Benicewicz, B. C. Nature Materials 2005, 4, 693.

37. Schadler, L. S.; Kumar, S. K.; Benicewicz, B. C.; Lewis, S. L.; Harton, S. E. MRS Bulletin 2007, 32, 335.

38. Adewole, J. K.; Ahmad, A. L.; Ismail, S.; Leo, C. P.; Sultan, A. S. Journal of Applied Polymer Science 2015, 132.

39. Koopal, L. K. Advances in Colloid and Interface Science 2012, 179-182, 29.

40. Gindl, M.; Gindl, W.; Sinn, G.; Reiterer, A.; Tschegg, S. Colloids and Surfaces A: Physicochemical and Engineering Aspects 2001, 181, 279.

41. POWAR, R. V.; GANGIL, S. INTERNATIONAL JOURNAL OF AGRICULTURAL ENGINEERING 2015, 8, 26.

42. Ahmed Al-Jumaili; Surjith Alancherry; Kateryna Bazaka; Mohan V Jacob. Materials (Basel, Switzerland) 2017, 10, 1066.

43. Husain, S.; Koros, W. J. Journal of Membrane Science 2007, 288, 195.

44. Hosseini, S. M.; Amini, S. H.; Khodabakhshi, A. R.; Bagheripour, E.; Van der Bruggen, B. Journal of the Taiwan Institute of Chemical Engineers 2018, 82, 169.

45. Abu-Bakar, A. S.; Moinuddin, K. Dec 2012.

46. Gabhi, R. S.; Kirk, D. W.; Jia, C. Q. Carbon 2017, 116, 435.

47. Zhang, L.; Li, Y.; Zhou, J. Applied Composite Materials 2018, 25, 1339.

48. Mohammad Hassan; Ragab Abou-Zeid; Enas Hassan; Linn Berglund; Yvonne Aitomäki; Kristiina Oksman. Polymers 2017, 9, 335.

49. DataPhysics Instruments.

50. Amooey, A. A.; Fazlollahnejad, M. Iranian Journal of Chemical Engineering 2014, 11, 19.

CHAPTER IV

[1] M. de França Doria, Factors influencing public perception of drinking water quality, Water Policy. 12 (2010) 1-19.

[2] R. Kant, Textile dyeing industry an environmental hazard, Natural Science. 4 (2012) 22-26.

[3] J. Wang, P. Zhang, B. Liang, Y. Liu, T. Xu, L. Wang, et al., Graphene Oxide as an Effective Barrier on a Porous Nanofibrous Membrane for Water Treatment, ACS applied materials & interfaces. 8 (2016) 6211-6218.

[4] E.I. Unuabonah, K.O. Adebowale, F.A. Dawodu, Equilibrium, kinetic and sorber design studies on the adsorption of Aniline blue dye by sodium tetraborate-modified Kaolinite clay adsorbent, Journal of Hazardous Materials. 157 (2008) 397-409.

[5] Sigma Aldrich, Methyl Blue Safety Data Sheet Version 5.4, (2016).

[6] T. Robinson, G. McMullan, R. Marchant, P. Nigam, Remediation of dyes in textile effluent: a critical review on current treatment technologies with a proposed alternative, Bioresource Technology. 77 (2001) 247-255.

[7] Y.H. Teow, A.W. Mohammad, New generation nanomaterials for water desalination: A review, Desalination. 451 (2019) 2-17.

[8] R. Mukherjee, S. De, Preparation, characterization and application of powdered activated carbon-cellulose acetate phthalate mixed matrix membrane for treatment of steel plant effluent, Polymers for Advanced Technologies. 27 (2016) 444-459.

[9] G.R. Guillen, Y. Pan, M. Li, E.M.V. Hoek, Preparation and Characterization of Membranes Formed by Nonsolvent Induced Phase Separation: A Review, (2011).

[10] G.J. Dahe, R.P. Singh, K.W. Dudeck, D. Yang, K.A. Berchtold, Influence of non-solvent chemistry on polybenzimidazole hollow fiber membrane preparation, Journal of Membrane Science. 577 (2019) 91-103.

[11] J. Garcia-Ivars, M. Iborra-Clar, M. Alcaina-Miranda, B. Van der Bruggen, Comparison between hydrophilic and hydrophobic metal nanoparticles on the phase separation phenomena during formation of asymmetric polyethersulphone membranes, Journal of Membrane Science. 493 (2015) 709-722.

[12] D. Wang, J. Lai, Recent advances in preparation and morphology control of polymeric membranes formed by nonsolvent induced phase separation, Current Opinion in Chemical Engineering. 2 (2013) 229-237.

[13] J. Dechnik, C.J. Sumby, C. Janiak, Enhancing Mixed-Matrix Membrane Performance with Metal–Organic Framework Additives, Crystal Growth & Design. 17 (2017) 4467-4488.

[14] M. Rezakazemi, A.E. Amooghin, M.M. Montazer-Rahmati, A.F. Ismail, T. Matsuura, State-of-the-art membrane based CO.sub.2 separation using mixed matrix membranes : An overview on current status and future directions, Progress in Polymer Science. 39 (2014) 817.

[15] Sedra Tul Muntha, Ayesha Kausar, Muhammad Siddiq, A review on Zeolite-Reinforced Polymeric Membranes: Salient Features and Applications, Polymer-Plastics Technology and Engineering. 55 (2016) 1971-1987.

[16] A. Ebadi Amooghin, S. Mashhadikhan, H. Sanaeepur, A. Moghadassi, T. Matsuura, S. Ramakrishna, Substantial breakthroughs on function-led design of advanced materials used in mixed matrix membranes (MMMs): A new horizon for efficient CO2 separation, Progress in Materials Science. 102 (2019) 222-295.

[17] R. Nasir, H. Mukhtar, Z. Man, D.F. Mohshim, Material Advancements in Fabrication of Mixed-Matrix Membranes, Chemical Engineering & Technology. 36 (2013) 717-727.

[18] M. Vinoba, M. Bhagiyalakshmi, Y. Alqaheem, A.A. Alomair, A. Pérez, M.S. Rana, Recent progress of fillers in mixed matrix membranes for CO 2 separation: A review, Separation and Purification Technology. 188 (2017) 431-450.

[19] Daniel Qadir, Hilmi Mukhtar, Lau Kok Keong, Mixed Matrix Membranes for Water Purification Applications, Separation and Purification Reviews. 46 (2016) 62-80.

[20] A. Pirkarami, M.E. Olya, Removal of dye from industrial wastewater with an emphasis on improving economic efficiency and degradation mechanism, Journal of Saudi Chemical Society. 21 (2017) S186.

[21] J.K. Adewole, A.L. Ahmad, S. Ismail, C.P. Leo, A.S. Sultan, Comparative studies on the effects of casting solvent on physico-chemical and gas transport properties of dense polysulfone membrane used for CO2/CH4separation, Journal of Applied Polymer Science. 132 (2015) n/a.

[22] D. Ariono, P.T.P. Aryanti, A.N. Hakim, S. Subagjo, I.G. Wenten, Determination of thermodynamic properties of polysulfone/PEG membrane solutions based on Flory-Huggins model, AIP Conference Proceedings. 1840 (2017).

[23] X. Tan, S. Liu, Y. Liu, Y. Gu, G. Zeng, X. Hu, et al., Biochar as potential sustainable precursors for activated carbon production: Multiple applications in environmental protection and energy storage, Bioresour.Technol. 227 (2017) 359-372.

[24] Wu-Jun Liu, Hong Jiang, Han-Qing Yu, Development of Biochar-Based Functional Materials: Toward a Sustainable Platform Carbon Material, Chemical Reviews. 115 (2015) 12251-12285.

[25] E. Costa, D. Aquilano, Experimental Value of the Specific Surface Energy of the Cleavage {10.4} Calcite Rhombohedron in the Presence of Its Saturated Aqueous Solution, Crystals. 8 (2018) 238.

[26] R. Syed, N. Sobh, U. Ravaioli, G. Popescu, M. Mohamed, imageJ, (2015).

[27] L.A. Soto-Salcido, G. González-Sánchez, B. Rocha-Gutierrez, R. Peralta-Perez, F.J. Zavala-Díaz, L. Ballinas-Casarrubias, Preparation, characterization and performance of acetylated cellulignin membranes obtained by green methods from biomass, Desalination. 430 (2018) 186-196.

[28] L.M. Camacho, J.A. Fox, J.O. Ajedegba, Optimization of electrodialysis metathesis (EDM) desalination using factorial design methodology, Desalination. 403 (2017) 136-143.

[29] D.C. Montgomery, Design and analysis of experiments, John Wiley & Sons, Inc, Hoboken, NJ, 2013.

[30] C. Liu, T. Xiao, L. Zhang, J. Zhang, M. Zhang, J. Yang, Effect of membrane wettability on membrane fouling and chemical durability of SPG membranes used in a microbubble-aerated biofilm reactor, Separation and Purification Technology. 127 (2014) 157-164.

[31] Li-Luen Hwang, Jyh-Cherng Chen, Ming-Yen Wey, The properties and filtration efficiency of activated carbon polymer composite membranes for the removal of humic acid, Desalination. 313 (2013) 166-175.

[32] M.G. García, J. Marchese, N.A. Ochoa, Effect of the particle size and particle agglomeration on composite membrane performance, Journal of Applied Polymer Science. (2010) n/a.

CHAPTER V

[1] Hoang Vinh-Thang, Serge Kaliaguine. Predictive Models for Mixed-Matrix Membrane Performance: A Review. Chemical Reviews, 113 (2013) 4980.

[2] R. Mahajan, W.J. Koros. Factors Controlling Successful Formation of Mixed-Matrix Gas Separation Materials. Industrial & Engineering Chemistry Research, 39 (2000) 2692.

[3] J. Sánchez-Laínez, B. Zornoza, S. Friebe, J. Caro, S. Cao, A. Sabetghadam, et al. Influence of ZIF-8 particle size in the performance of polybenzimidazole mixed matrix membranes for pre-combustion CO2 capture and its validation through interlaboratory test. Journal of Membrane Science, 515 (2016) 45.

[4] B. Ghalei, K. Sakurai, Y. Kinoshita, K. Wakimoto, A. Isfahani, Q. Song, et al. Enhanced selectivity in mixed matrix membranes for CO2 capture through efficient dispersion of amine-functionalized MOF nanoparticles. Nature Energy, 2 (2017).

[5] D.Q. Vu, W.J. Koros, and S.J. Miller. Mixed matrix membranes using carbon molecular sieves: I. Preparation and experimental results. Journal of Membrane Science, 211 (2003) 311.

[6] E.E. Oral, L. Yilmaz, and H. Kalipcilar. Effect of gas permeation temperature and annealing procedure on the performance of binary and ternary mixed matrix membranes of polyethersulfone, SAPO-34, and 2-hydroxy 5-methyl aniline. Journal of Applied Polymer Science, 131 (2014) 8498.

[7] A.F. Ismail, R.A. Rahim, and W.A.W.A. Rahman. Characterization of polyethersulfone/Matrimid® 5218 miscible blend mixed matrix membranes for O2/N2 gas separation. Separation and Purification Technology, 63 (2008) 200.

[8] S. Husain, W.J. Koros. Mixed matrix hollow fiber membranes made with modified HSSZ-13 zeolite in polyetherimide polymer matrix for gas separation. Journal of Membrane Science, 288 (2007) 195.

[9] C. Torras, F. Ferrando, J. Paltakari, and R. Garcia-Valls. Performance, morphology and tensile characterization of activated carbon composite membranes for the synthesis of enzyme membrane reactors. Journal of Membrane Science, 282 (2006) 149.

[10] Z. Li, J. Chu, C. Yang, S. Hao, M.A. Bissett, I.A. Kinloch, et al. Effect of functional groups on the agglomeration of graphene in nanocomposites. Composites Science and Technology, 163 (2018) 116.

[11] A. Ebadi Amooghin, S. Mashhadikhan, H. Sanaeepur, A. Moghadassi, T. Matsuura, and S. Ramakrishna. Substantial breakthroughs on function-led design of advanced materials used in mixed matrix membranes (MMMs): A new horizon for efficient CO2 separation. Progress in Materials Science, 102 (2019) 222.

[12] M. Ahmadi, S. Janakiram, Z. Dai, L. Ansaloni, and L. Deng. Performance of Mixed Matrix Membranes Containing Porous Two-Dimensional (2D) and Three-Dimensional (3D) Fillers for CO_2 Separation: A Review. Membranes, 8 (2018) 50.

[13] Y. Lan, W. Wang. Application of tree biochar in PDMS pervaporation membranes. Advances in Polymer Technology, (2017).

[14] R. Saranya, M. Kumar, R. Tamilarasan, A.F. Ismail, and G. Arthanareeswaran. Functionalised activated carbon modified polyphenylsulfone composite membranes for adsorption enhanced phenol filtration. Journal of Chemical Technology & Biotechnology, 91 (2016) 748.

[15] Z. Wang, D. Wang, S. Zhang, L. Hu, and J. Jin. Interfacial Design of Mixed Matrix Membranes for Improved Gas Separation Performance. Advanced Materials, 28 (2016) 3399.

[16] Xiao-fei Tan, Shao-bo Liu, Yun-guo Liu, Yan-ling Gu, Guang-ming Zeng, and Xin-jiang Hu. Biochar as potential sustainable precursors for activated carbonproduction:Multiple applications in environmental protection andenergy storage. Bioresource technology, 227 (2017) 359.

[17] M. Anson, J. Marchese, E. Garis, N. Ochoa, and C. Pagliero. ABS copolymer-activated carbon mixed matrix membranes for CO 2/CH 4 separation. Journal of Membrane Science, 243 (2004) 19.

[18] S. Sridhar, B. Smitha, R. Suryamurali, and T.M. Aminabhavi. Synthesis, Characterization and Gas Permeability of an Activated Carbon-Loaded PEBAX 2533 Membrane. Designed Monomers and Polymers, 11 (2008) 17.

[19] Fynn Weigelt, Prokopios Georgopanos, Sergey Shishatskiy, Volkan Filiz, Torsten Brinkmann, and Volker Abetz. Development and Characterization of Defect-Free Matrimid Mixed-Matrix Membranes Containing Activated Carbon Particles for Gas Separation. Polymers, 10 (2018) 1.

[20] H. Mushardt, M. Müller, S. Shishatskiy, J. Wind, and T. Brinkmann. Detailed Investigation of Separation Performance of a MMM for Removal of Higher Hydrocarbons under Varying Operating Conditions. Membranes, 6 (2016) 16.

[21] Activated carbon. Standard test method for determination of iodine number. (2015).

[22] S. Cong, H. Li, X. Shen, J. Wang, J. Zhu, J. Liu, et al. Construction of graphene oxide based mixed matrix membranes with CO_2-philic sieving gas-transport channels through strong π–π interactions. Journal of Materials Chemistry A, 6 (2018) 17854.

[23] J.K. Adewole, A.L. Ahmad, S. Ismail, C.P. Leo, and A.S. Sultan. Comparative studies on the effects of casting solvent on physico-chemical and gas transport properties of dense polysulfone membrane used for CO_2/CH_4separation. Journal of Applied Polymer Science, 132 (2015).

[24] S.M. Hosseini, S.H. Amini, A.R. Khodabakhshi, E. Bagheripour, and B. Van der Bruggen. Activated carbon nanoparticles entrapped mixed matrix polyethersulfone based nanofiltration membrane for sulfate and copper removal from water. Journal of the Taiwan Institute of Chemical Engineers, 82 (2018) 169.

[25] J.K. Adewole, A.L. Ahmad, S. Ismail, and C.P. Leo. Current challenges in membrane separation of CO_2 from natural gas: A review. International Journal of Greenhouse Gas Control, 17 (2013) 46.

APPENDIX B

1. Korotta-Gamage SM, Sathasivan A. A review: Potential and challenges of biologically activated carbon to remove natural organic matter in drinking water purification process. 2017;167:120-38; doi: 10.1016/j.chemosphere.2016.09.097.

2. Cordero-Lanzac T, Palos R, Arandes JM, Castaño P, Rodríguez-Mirasol J, Cordero T, Bilbao J. Stability of an acid activated carbon based bifunctional catalyst for the raw bio-oil hydrodeoxygenation. 2017;203:389-99; doi: 10.1016/j.apcatb.2016.10.018.

3. Zhang Y, Lei H, Yang Z, Qian K, Villota E. Renewable High-Purity Mono-Phenol Production from Catalytic Microwave-Induced Pyrolysis of Cellulose over Biomass-Derived Activated Carbon Catalyst. 2018;6:5349-57; doi: 10.1021/acssuschemeng.8b00129.

4. Sawant SY, Munusamy K, Somani RS, John M, Newalkar BL, Bajaj HC. Precursor suitability and pilot scale production of super activated carbon for greenhouse gas adsorption and fuel gas storage. 2017;315:415-25; doi: 10.1016/j.cej.2017.01.037.

5. Tan X, Liu S, Liu Y, Gu Y, Zeng G, Hu X, Wang X, Liu S, Jiang L. Biochar as potential sustainable precursors for activated carbon production: Multiple applications in environmental protection and energy storage. Bioresour Technol. 2017;227:359-72

6. Dupont C, Chen L, Cances J, Commandre J, Cuoci A, Pierucci S, Ranzi E. Biomass pyrolysis: Kinetic modelling and experimental validation under high temperature and flash heating rate conditions. 2009;85:260-7; doi: 10.1016/j.jaap.2008.11.034.

7. Tsai W, Chang C, Lee S, Wang S. Thermogravimetric Analysis of Corn Cob Impregnated With Zinc Chloride for Preparation of Activated Carbon. 2000;63:351-7; doi: 1010132207402.

8. Moralı U, Demiral H, Şensöz S. Optimization of activated carbon production from sunflower seed extracted meal: Taguchi design of experiment approach and analysis of variance. 2018;189:602-11; doi: 10.1016/j.jclepro.2018.04.084.

9. Mopoung S, Moonsri P, Palas W, Khumpai S. Characterization and Properties of Activated Carbon Prepared from Tamarind Seeds by KOH Activation for Fe(III) Adsorption from Aqueous Solution. 2015;2015:415961-9; doi: 10.1155/2015/415961.

10. Shawabkeh R, Aslam Z, Hussien I. Thermochemical treatment of fly ash for synthesis of mesoporous activated carbon. J Therm Anal Calorim. 2015;122:1191-201; doi: 10.1007/s10973-015-4964-7.

11. Bazan A, Nowicki P, Półrolniczak P, Pietrzak R. Thermal analysis of activated carbon obtained from residue after supercritical extraction of hops. J Therm Anal Calorim. 2016;125:1199-204; doi: 10.1007/s10973-016-5419-5.

12. Polovina M, Babić B, Kaluderović B, Dekanski A. Surface characterization of oxidized activated carbon cloth. 1997;35:1047-52; doi: 10.1016/S0008-6223(97)00057-2.

13. Adib F, Bagreev A, Bandosz TJ. Adsorption/Oxidation of Hydrogen Sulfide on Nitrogen-Containing Activated Carbons. 2000;16:1980-6; doi: 10.1021/la990926o.

14. Liu W, Vidic RD, Brown TD. Impact of Flue Gas Conditions on Mercury Uptake by Sulfur-Impregnated Activated Carbon. 2000;34:154-9; doi: 10.1021/es990315i.

15. Anonymous Activated carbon. Standard test method for determination of iodine number. 2015

16. Mianowski A, Owczarek M, Marecka A. Surface Area of Activated Carbon Determined by the Iodine Adsorption Number. 2007;29:839; doi: 10.1080/00908310500430901.

17. Nunes CA, Guerreiro MC. Estimation of surface area and pore volume of activated carbons by methylene blue and iodine numbers. 2011;34:472-6; doi: 10.1590/S0100-40422011000300020.

18. Pan D, Jaroniec M, Klinik J. Thermogravimetric evaluation of the specific surface area and total porosity of microporous carbons. 1996;34:1109-13; doi: //doi.org/10.1016/0008-6223(96)00063-2.

19. Mercuri LP, Matos JR, Jaroniec M. Improved thermogravimetric determination of the specific surface area for cerium-incorporated MCM-41 materials. 2002;344:190-4; doi: 10.1016/S0925-8388(02)00338-9.

20. Mercuri LP, Matos JR, Li Z, Jaroniec M. Comparative thermogravimetric and adsorption study of highly ordered mesoporous materials. 2006;296:377-80; doi: //doi.org/10.1016/j.jcis.2005.08.043.

21. You SY, Park CR, Park YH. Preparation and properties of activated carbon fabric from acrylic fabric waste. 2000;38:1453-60; doi: 10.1016/S0008-6223(99)00278-X.

22. Araujo AS, Jaroniec M. Determination of the surface area and mesopore volume for lanthanide-incorporated MCM-41 materials by using high resolution thermogravimetry. 2000;345:173-7; doi: 10.1016/S0040-6031(99)00374-3.

23. Shrestha A. Characterization of porous membranes via porometry. 2012

24. Pan D, Jaroniec M. Adsorption and Thermogravimetric Studies of Unmodified and Oxidized Active Carbons. 1996;12:3657-65; doi: 10.1021/la951549s.

25. KUANG M, YANG G, CHEN W, ZHANG Z. Study on mercury desorption from silver-loaded activated carbon fibre and activated carbon fibre. 2008;36:468-73; doi: 10.1016/S1872-5813(08)60030-4.

26. Kwok Q, Jones D. Thermodesorption studies of ammonium nitrate prills by high-resolution thermogravimetry. 2003;74:57-63; doi: 1026317517373.

27. Wei M, Yu Q, Xie H, Zuo Z, Hou L, Yang F. Kinetics studies of CO2 adsorption and desorption on waste ion-exchange resin-based activated carbon. 2017;42:27122-9; doi: 10.1016/j.ijhydene.2017.09.102.

28. Rashidi NA, Yusup S, Hameed BH. Kinetic studies on carbon dioxide capture using lignocellulosic based activated carbon. 2013;61:440-6; doi: 10.1016/j.energy.2013.08.050.

29. Shafeeyan MS, Daud, Wan Mohd Ashri Wan, Houshmand A, Arami-Niya A. Ammonia modification of activated carbon to enhance carbon dioxide adsorption: Effect of pre-oxidation. 2011;257:3936-42; doi: 10.1016/j.apsusc.2010.11.127.

30. Creamer AE, Gao B, Zhang M. Carbon dioxide capture using biochar produced from sugarcane bagasse and hickory wood. 2014;249:174-9; doi: 10.1016/j.cej.2014.03.105.

APPENDIX C

[1] C. Buelke, A. Alshami, J. Casler, J. Lewis, M. Al-Sayaghi, M.A. Hickner, Graphene oxide membranes for enhancing water purification in terrestrial and space-born applications: State of the art, Desalination. (2018).

[2] M. Su, S. Bai, Y. Luo, G. Chu, B. Sun, Y. Le, et al., Controllable wettability on stainless steel substrates with highly stable coatings, Chemical Engineering Science. (2018).

[3] B. He, S. Yang, Z. Qin, B. Wen, C. Zhang, The roles of wettability and surface tension in droplet formation during inkjet printing, Scientific reports. 7 (2017) 11841-7.

[4] J. Lee, R.S. Fearing, Wet self-cleaning of superhydrophobic microfiber adhesives formed from high density polyethylene, Langmuir : the ACS journal of surfaces and colloids. 28 (2012) 15372-15377.

[5] G. Bracco, Surface science techniques, Springer, Berlin [u.a.], 2013.

[6] K.M. Forward, A.L. Moster, D.K. Schwartz, D.J. Lacks, Contact angles of submillimeter particles: connecting wettability to nanoscale surface topography, Langmuir : the ACS journal of surfaces and colloids. 23 (2007) 5255-5258.

[7] S. Nuriel, L. Liu, A.H. Barber, H.D. Wagner, Direct measurement of multiwall nanotube surface tension, Chemical Physics Letters. 404 (2005) 263-266.

[8] Tommi Huhtamäki, Xuelin Tian, Juuso T Korhonen, Robin H A Ras, Surface-wetting characterization using contact-angle measurements, Nature Protocols. 13 (2018) 1521-1538.

[9] E. Costa, D. Aquilano, Experimental Value of the Specific Surface Energy of the Cleavage {10.4} Calcite Rhombohedron in the Presence of Its Saturated Aqueous Solution, Crystals. 8 (2018) 238.

[10] D. Cwickel, Y. Paz, A. Marmur, Contact angle measurement on rough surfaces: the missing link, Surface Innovations. 5 (2017) 190-193.

[11] H. Gu, C. Wang, S. Gong, Y. Mei, H. Li, W. Ma, Investigation on contact angle measurement methods and wettability transition of porous surfaces, Surface & Coatings Technology. 292 (2016) 72-77.

[12] R. Syed, N. Sobh, U. Ravaioli, G. Popescu, M. Mohamed, imageJ, (2015).

[13] D.C. Montgomery, Design and analysis of experiments, John Wiley & Sons, Inc, Hoboken, NJ, 2013.

[14] E.W. Weisstein, Spherical Cap, From MathWorld- A Wolfram Web Resource.

[15] K.L. Mittal, Contact Angle, Wettability and Adhesion, Chapman and Hall/CRC, Baton Rouge, 2009.

[16] Majid H. Majeed, Static Contact Angle and Large Water Droplet Thickness Measurements with the Change of Water Temperature, مجلة النهرين للعلوم الهندسية. 17 (2014) 114-128.

[17] E. Chen, M. Elias, J. Lin, N. Okun, O. Omole, M. Piccolella, et al., IMPROVING THE HYDROPHOBICITY OF KITCHENWARE THROUGH THE COVALENT BONDING OF PHOSPHONIC ACIDS, Drew University. (2012).

[18] N. Wei, C. Lv, Z. Xu, Wetting of graphene oxide: a molecular dynamics study, Langmuir : the ACS journal of surfaces and colloids. 30 (2014) 3572-3578.

[19] B.R. Ray, F.E. Bartell, Hysteresis of contact angle of water on paraffin. Effect of surface roughness and of purity of paraffin, Journal of Colloid Science. 8 (1953) 214-223.

[20] B. Tieke, F. van Ackern, L. Krasemann, A. Toutianoush, Ultrathin self-assembled polyelectrolyte multilayer membranes, Eur. Phys. J. E. 5 (2001) 29-39.

[21] Y. Li, J.Q. Pham, K.P. Johnston, P.F. Green, Contact angle of water on polystyrene thin films: effects of CO(2) environment and film thickness, Langmuir : the ACS journal of surfaces and colloids. 23 (2007) 9785.

[22] N. Spahis, M. Dellali, H. Mahmoudi, Synthesis and Characterization of Polymeric/Activated Carbon Membranes, Procedia Engineering. 33 (2012) 47-51.

[23] P.B. Kowalczuk, J. Drzymala, Some remarks on attachment of a gas bubble to another phase both immersed in water, (2016).

[24] MS Ferritto, MJ Owen, Silicone Wettability and Its Significance in Beauty Products, Polymers for Personal Care and Cosmetics, American Chemical Society, 2013, pp. 219-232.

[25] Patrícia Campos Bernardes, Nelio Jose Deandrade, Sukarno Olavo Ferreira, João Paulo Natalino Desa, Emiliane Andrade Araújo, Deyse Maria Zanom Delatorre, et al., Assessment of hydrophobicity and roughness of stainless steel adhered by an isolate of Bacillus cereus from a dairy plant, Brazilian Journal of Microbiology. 41 (2010) 984-992.

[26] S. Johnson, Presented at Aspects of Adhesion, Radcure, Middlesex, UK, Presented at Aspects of Adhesion, Radcure, Middlesex, UK. (1992).

[27] S. Wu, Calculation of interfacial tension in polymer systems, Journal of Polymer Science Part C: Polymer Symposia. 34 (1971) 19-30.

[28] E. Bormashenko, R. Pogreb, G. Whyman, Y. Bormashenko, R. Jager, T. Stein, et al., The reversible giant change in the contact angle on the polysulfone and polyethersulfone films exposed to UV irradiation, Langmuir : the ACS journal of surfaces and colloids. 24 (2008) 5977-5980.